이학 박사 학위논문

스태거드 쿼크의 카이랄성과 테이스트 대칭성

Chirality and Taste Symmetry of Staggered Quarks

2020년 8월

서울대학교 대학원

물리천문학부 물리학 전공

정환철

Abstract

This thesis investigates the general properties of the eigenvalue spectrum for improved staggered quarks and underlying chiral symmetry and SU(4) taste symmetry on it. Staggered fermion formalism is a methodology of lattice gauge theory studying quantum chromodynamics. Unfortunately, both chiral symmetry and taste symmetry are not conserved exactly for staggered quarks on the lattice. However, results of this work indicate that those symmetries are considerably preserved and retain some continuum behaviors for the improved staggered quarks such as HYP staggered quarks, Asqtad staggered quarks, and HISQ staggered quarks. Numerical simulations in this thesis are performed in quenched QCD approximation using HYP staggered quarks.

Here, a new chirality operator and a new shift operator are introduced. Unlike Golterman's irreducible representations, new definitions respect the same recursion relations as the continuum chirality operator γ_5 and related with each other by chiral Ward identity of conserved $U(1)_A$ axial symmetry of staggered fermion actions. Chirality of staggered Dirac eigenmodes is measured by this new chirality operator, by which the would-be zero modes are identified, and their correspondence with topological charge via the index theorem is discussed.

By extending this standard chirality measurement, the transition of chirality from an eigenmode to another is also studied by measuring the matrix elements of the chirality operator and the shift operator on the staggered Dirac eigenspace. This quantity is named leakage. The chiral Ward identity ensures eight leakage elements of the chirality operator and the shift operator are identical, which holds within numerical precision. Further investigation on the leakage reveals that leakages for would-be zero modes and non-zero modes exhibit opposite patterns so that one can discriminate them rigorously. Besides, the leakage pattern for non-zero modes reveals the existence of the SU(4) taste symmetry clearly, by which two barometers of the taste symmetry breaking are measured. A machine learning analysis confirms the universality of leakage patterns. As a byproduct of this research, the renormalization of chirality is also discussed.

Keywords: quantum chromodynamics, lattice gauge theory, staggered fermion, chiral symmetry, taste symmetry

Student Number: 2012-30108

Contents

List of Figures

List of Tables

Chapter 1

Introduction

It is important to understand the low-lying eigenvalue spectrum of the Dirac operator, which exhibits the topological Ward identity of the Atiyah-Singer index theorem [1], the Banks-Casher relationship [2], and the universality of the distribution of the near-zero modes for fixed topological charge sectors [3, 4]. Study on the eigenvalue spectrum of the Dirac operator is, by nature, highly non-perturbative. Hence, numerical tools available in lattice gauge theory provide a perfect playground to study on diverse properties of the Dirac eigenvalue spectrum.

In lattice QCD, there are a number of ways to implement a discrete version of the continuum Dirac operator on the lattice. Among them, in this thesis one particular class of lattice fermions that are widely used in lattice QCD community is discussed: improved stag-

gered quarks [5–7]. Here, the eigenvalue spectrum of staggered Dirac operators in quenched QCD approximation is studied in order to show that the small eigenvalues near zero modes reproduce the continuum properties very closely, which was originally noticed in Refs. [8–10]. To reach this conclusion of Refs. [8–10], they performed a number of tests including (1) the Atiya-Singer index theorem that describes the chiral Ward identity relating the zero modes to the topological charge; (2) the Banks-Casher relationship that relates the chiral condensate to the density of eigenvalues at the zero mode; (3) the universality of the small eigenvalue spectrum in the ε-regime that is predicted from the random matrix theory. In addition, in Ref. [11, 12], they used the spectral flow method of Adams [13] to identify the zero modes from the mixture with non-zero modes. The spectral flow method is robust but highly expensive in a computational sense.

Here, a new advanced chirality operator $[\gamma_5 \otimes 1]$ which respects the continuum algebra of γ_5 is introduced. It is shown that the matrix elements of this chirality operator in the basis of Dirac eigenstates are related to those of the shift operator $[1 \otimes \xi_5]$ through the Ward identity of the conserved $\mathrm{U(1)_A}$ symmetry of staggered fermions. In addition, a new concept of leakage pattern is introduced to distinguish zero modes from non-zero modes. Using the leakage pattern of the chirality and shift operators, it is possible to measure the zero modes as reliably as the spectral flow method. Hence, it would be possible

to determine the topological charge Q using the leakage pattern with much smaller computational cost than the spectral flow methods. The determination of the ratio of renormalization constants, $Z_{P\times S}/Z_{P\times P}$ using the leakage pattern is also discussed.

This thesis is heavily based on Ref. [14]. Preliminary results of this study are also available in Ref. [15–17].

Chapter 2

Staggered fermion

2.1 Lattice gauge theory [1]

In the continuum Euclidean spacetime, the Lagrangian density for quantum chromodynamics (QCD) is given by

$$\mathcal{L} = \sum_{f=1}^{N_f} \left[\bar{\psi}_f(x)(\gamma_\mu D_\mu + m_f)\psi_f(x)\right] - \frac{1}{4}F_{\mu\nu}F^{\mu\nu} \tag{2.1}$$

where $\psi_f(x)$ is the quark field of flavor f and m_f is the mass of the corresponding quark. γ_μ is Dirac spin matrix and D_μ is the covariant derivative defined as

$$D_\mu = \partial_\mu - igA_\mu(x)\,. \tag{2.2}$$

[1] Most of discussions in this section are based on Ref. [18] and [19].

Here, $A_\mu(x) = \sum_a \lambda^a A^a_\mu(x)$ is the gauge field where λ^a is the generator of the SU(3) color gauge group. $F_{\mu\nu}(x)$ is the field strength tensor given by

$$F_{\mu\nu} = \sum_a \lambda^a (\partial_\mu A^a_\nu - \partial_\nu A^a_\mu + g f_{abc} A^b_\mu A^c_\nu) \,. \tag{2.3}$$

However, QCD is amenable to perturbative approaches only at high energies since the asymptotic freedom implies a growth of the coupling constant g in the infrared. Lattice gauge theory provides a non-perturbative method to study the low energy properties of QCD [20]. QCD with the lattice gauge theory is called lattice QCD or LQCD. The lattice regularization of QCD discretizes Euclidean spacetime on a four dimensional hypercubic lattice with lattice spacing $a > 0$. Quark fields $\psi(x)$ and $\bar{\psi}(x)$ are placed on each site of the lattice, and gauge field $A_\mu(x)$ on each link between two neighbor sites.

On the lattice, the derivative of a quark field is defined as the symmetric finite difference[2]:

$$\partial_\mu \psi(x) \approx \frac{1}{2a} \left[\psi(x + a\hat{\mu}) - \psi(x - a\hat{\mu}) \right] \,, \tag{2.4}$$

which has a correction of $\mathcal{O}(a^2)$. We define a covariant derivative as

$$D_\mu \psi(x) \approx \frac{1}{2a} \left[U_\mu(x) \psi(x + a\hat{\mu}) - U^\dagger_\mu(x - a\hat{\mu}) \psi(x - a\hat{\mu}) \right] \,. \tag{2.5}$$

[2]Here, $\approx$ means that the left-hand side is the expression in the continuum QCD, and the right-hand side is the definition in the lattice QCD

Here, $U_\mu(x)$ is the gauge link given by

$$U_\mu(x) = \exp(iaA_\mu(x))\,, \tag{2.6}$$

which corresponds to Wilson line connecting x and $x+\hat{\mu}$ in the continuum QCD. For a SU(3) gauge transformation $\Omega(x)$, $U_\mu(x)$ transforms as follows:

$$U'_\mu(x) = \Omega(x)\, U_\mu(x)\, \Omega^\dagger(x + a\hat{\mu})\,. \tag{2.7}$$

Hence, we find that $\bar{\psi}(x)\, U_{\pm\mu}(x)\, \psi(x \pm a\hat{\mu})$ is gauge invariant.

Noting that the trace of a product of $U_\mu(x)$ around any closed loop is gauge invariant, the simplest possible gauge action is given by

$$S_g = \frac{6}{g^2} \sum_{x,\mu,\nu} \left[1 - \frac{1}{3} \mathrm{Re}\,\mathrm{Tr} \Big[U_\mu(x) U_\nu(x + a\hat{\mu}) U^\dagger_\mu(x + a\hat{\nu}) U^\dagger_\nu(x) \Big] \right]. \tag{2.8}$$

The gauge action S_g defined as Eq. (2.8) is called Wilson gauge action. One can show that S_g reproduces the continuum Yang-Mills action in the continuum limit $a \to 0$.

Now one can define a lattice Dirac operator from Eq. (2.5). However, a naive approach of $\gamma_\mu D_\mu$ induces 2^4 equivalent fermion doublers, which is so called the fermion doubling problem. Nielsen and Ninomiya's no-go theorem states that no lattice fermions has exact continuum-like chiral symmetry without the fermion doublers [21]. There are several popular lattice fermion methods which apply differ-

ent strategies for dealing with this doubling problem, such as Wilson fermions, staggered fermions, overlap fermions, domain-wall fermions, and their variants. Wilson fermions decouple all doublers by introducing a Wilson term, but they violate the chiral symmetry. Staggered fermions diagonalize the Dirac spin matrix, which reduces the number of doublers to 4 while preserving some chiral symmetry. Overlap fermions and domain-wall fermions are also called Ginsparg-Wilson fermions since they satisfy the Ginsparg-Wilson relation which restores an exact chiral symmetry in the continuum limit without the doublers. In theoretical sense, the Ginsparg-Wilson fermions would be preferred. However, in practice they require much greater computational cost compared with Wilson fermions and staggered fermions. Hence, one should choose a proper lattice fermions according to the physics target.

2.2 Staggered fermions [3]

Staggered fermions are one of the most popular lattice fermions. A key concept of staggered fermions is the diagonalization of Dirac spin matrix γ_μ, which allows to absorb spin degrees of freedom of quark field into one component field.

Let us assume x is a discretized lattice coordinate and the lattice spacing $a = 1$ for notational convenience. We define a local transfor-

[3] Most of discussions in this section are based on Ref. [18] and [19].

mation γ_x as

$$\gamma_x \equiv \gamma_0^{n_0}\,\gamma_1^{n_1}\,\gamma_2^{n_2}\,\gamma_3^{n_3}\,, \tag{2.9}$$

where $x = (n_0, n_1, n_2, n_3)$ with $n_\mu \in \mathbb{Z}$. It satisfies $\gamma_x^\dagger \gamma_x = 1$. Quark fields $\psi(x)$ and $\bar{\psi}(x)$ transform via γ_x as

$$\psi'(x) = \gamma_x\,\psi(x)\,, \tag{2.10}$$

$$\bar{\psi}'(x) = \bar{\psi}(x)\,\gamma_x^\dagger\,. \tag{2.11}$$

A crucial property of this transformation is that it diagonalizes the Dirac spin matrix γ_μ as follows:

$$\gamma_x^\dagger\,\gamma_\mu\,\gamma_{x\pm\hat{\mu}} = (-1)^{\sum_{\nu<\mu} n_\nu} \equiv \eta_\mu(x)\,. \tag{2.12}$$

It gives

$$\bar{\psi}'_\alpha(x)(\gamma_\mu)_{\alpha\beta}\,\psi'_\beta(x \pm \hat{\mu}) = \eta_\mu(x)\,\bar{\psi}(x)_\alpha \psi(x)_\alpha\,, \tag{2.13}$$

where α, β are spin indices. Eq. (2.13) implies that the quark action is diagonalized in spinor space. In other words, all spin components of the quark field interact independently and contribute identically to the action. It allows us to merge the four spin components of the quark field $\psi_\alpha(x)$ into one component field $\chi(x)$.

Now we write the staggered fermion action:

$$S = \frac{1}{2a}\sum_{x,\mu}\eta_\mu(x)\left[\bar{\chi}(x)U_\mu(x)\chi(x+a\hat{\mu}) - \bar{\chi}(x)U_\mu^\dagger(x-a\hat{\mu})\chi(x-a\hat{\mu})\right] + m\sum_x \bar{\chi}(x)\chi(x)\,. \tag{2.14}$$

Because of the sign alternation of $\eta_\mu(x)$ along each direction, it is natural to consider 2^4 hypercube which has two lattice points $\{0,1\}$ in each direction as the unit cell for the staggered fermion field. Thus, we parameterize x in terms of 2^4 hypercube coordinate:

$$x_A \equiv 2x + A\,, \tag{2.15}$$

where A is the hypercube coordinate with $A_\mu \in \{0,1\}$. For staggered fermions, and in this thesis, 'hypercube' simply means 2^4 hypercube.

The $16(=2^4)$ degrees of freedom that comes from the hypercube can be interpreted as four sets of four spin degrees of freedom. Remaining four degrees of freedom is called *taste*. In other words, a single staggered fermion corresponds to four tastes of continuum fermions. One can consider this extra four tastes as four flavors with a degenerated mass. To be precise, staggered fermions have a taste symmetry of $\mathrm{SU(4)_L} \otimes \mathrm{SU(4)_R} \otimes \mathrm{U(1)_V}$ in the continuum limit at $a = 0$ [22]. However, this symmetry breaks down to a subgroup of $\mathrm{U(1)_V} \otimes \mathrm{U(1)_A}$ on the lattice with $a \neq 0$ [22, 23]. In this reason, we call it as taste

instead of flavor. It is important for staggered fermions to reduce the breaking effect of the taste symmetry. In the meantime, the remaining axial symmetry of $U(1)_A$ plays an important role in protecting the quark mass from receiving an additive renormalization. Besides, it does not have any axial anomaly.

The greatest advantage of staggered fermions is on the computational speed. By virtue of making use of the one component field χ, the speed of a lattice simulation using staggered fermions is the fastest compared with those using other popular lattice fermions such as Wilson fermions, domain-wall fermions, and overlap fermions. Unlike Wilson fermions for which chiral symmetry is completely broken, staggered fermions preserve some chiral symmetry of the continuum. A real concern for staggered fermions is how to deal with the unexpected taste symmetry and its breaking effect.

There are a number of improved versions of staggered fermions such as HYP-smeared staggered fermions [5], asqtad improved staggered fermions [24], and HISQ staggered fermions [7]. All discussions in this thesis can be applied to any staggered fermion formalism regardless of its improvement details. Hence, let us consider "staggered fermions" in this thesis as all of staggered fermion formalisms collectively.

2.3 Quark bilinears

2.3.1 Staggered bilinear operator

Let us consider $\gamma_S \in \{\mathbb{1}, \gamma_\mu, \gamma_{\mu\nu}, \gamma_{\mu 5}, \gamma_5\}$ as Dirac spin matrices satisfying Clifford algebra $\{\gamma_\mu, \gamma_\nu\} = 2\delta_{\mu\nu}$ in Euclidean spacetime. Similarly, we define 4×4 taste matrices $\xi_T \in \{\mathbb{1}, \xi_\mu, \xi_{\mu\nu}, \xi_{\mu 5}, \xi_5\}$ as satisfying Clifford algebra $\{\xi_\mu, \xi_\nu\} = 2\delta_{\mu\nu}$ in Euclidean spacetime. Then staggered bilinear operators $\mathcal{O}_{S\times T}$ are defined by combinations of γ_S and ξ_T in the following way:

$$\begin{aligned}\mathcal{O}_{S\times T}(x) &\equiv \bar{\chi}(x_A)[\gamma_S \otimes \xi_T]_{AB}\chi(x_B) \\ &\equiv \bar{\chi}(x_A)\,\overline{(\gamma_S \otimes \xi_T)}_{AB}\,U(x_A, x_B)\,\chi(x_B)\,, \end{aligned} \tag{2.16}$$

where $\chi(x)$ is the staggered quark field introduced in Eq. (2.14) and the coordinate parameterization $x_A = 2x + A$ is defined in Eq. (2.15) with hypercubic vectors $A_\mu, B_\mu \in \{0, 1\}$. In the second line,

$$\overline{(\gamma_S \otimes \xi_T)}_{AB} = \frac{1}{4}\,\mathrm{Tr}\Big(\gamma_A^\dagger \gamma_S \gamma_B \gamma_T^\dagger\Big)\,, \tag{2.17}$$

and

$$U(x_A, x_B) \equiv \mathbb{P}_{\mathrm{SU}(3)}\left[\sum_{p\in\mathcal{C}} V(x_A, x_{p_1})V(x_{p_1}, x_{p_2})\cdots V(x_{p_n}, x_B)\right]. \tag{2.18}$$

Here, $\mathbb{P}_{\mathrm{SU}(3)}$ represents the SU(3) projection, and $\mathcal{C}$ represents a complete set of the shortest paths from x_A to x_B. $V(x, y)$ represents a (smeared) gauge link from x to y, which is the HYP-smeared fat link [5, 6] for HYP staggered fermions, the Fat7 fat link [6, 25–27] for asqtad or HISQ staggered fermions, and the thin gauge link for unimproved staggered fermions.

2.3.2 Golterman's irreducible representation

Golterman [28] proposed irreducible representations of quark bilinears for staggered fermions. Golterman's definition can be summarized as

$$\mathcal{O}^G_{S\times T}(x) = \sum_A \rho_{S\times T}(A)\ \bar{\chi}(x_A)\, M_{S\times T}\ \chi(x_A)\,. \tag{2.19}$$

Here, superscript G stands for Golterman. $\rho_{S\times T}(A)$ is a phase factor depending on the hypercube coordinate A. The operator $M_{S\times T}$ is given by

$$M_{S\times T}\ \chi(x_A) \equiv \prod_\mu \left[(1 - |S_\mu - T_\mu|\,) + |S_\mu - T_\mu|\,\widetilde{D}_\mu\right] \chi(x_A)\,, \tag{2.20}$$

where S_μ and T_μ are 2^4 hypercube coordinates determined by

$$\gamma_S = \gamma_0^{S_0}\gamma_1^{S_1}\gamma_2^{S_2}\gamma_3^{S_3}\,, \tag{2.21}$$

$$\gamma_T = \gamma_0^{T_0}\gamma_1^{T_1}\gamma_2^{T_2}\gamma_3^{T_3}\,. \tag{2.22}$$

Note that $S_\mu, T_\mu \in \{0, 1\}$. When $S_\mu = T_\mu$, the squared bracket in Eq. (2.20) does nothing. On the other hand, when $S_\mu \neq T_\mu$, i.e., $|S_\mu - T_\mu| = 1$, the symmetric shift operator $\widetilde{D}_\mu$ is applied to the field. $\widetilde{D}_\mu$ is defined as

$$\widetilde{D}_\mu \, \chi(x_A) \equiv \frac{1}{2} \left[V_\mu(x_A) \, \chi(x_A + \hat{\mu}) + V_\mu^\dagger(x_A - \hat{\mu}) \, \chi(x_A - \hat{\mu}) \right] , \quad (2.23)$$

where $V_\mu(x)$ is the (smeared) gauge link as in Eq. (2.18). Note that the plus sign between two terms in the bracket is the only difference from the lattice covariant derivative in Eq. (2.5).

Chapter 3

Physics of eigenvalues

3.1 Eigenvalues of Dirac operator

3.1.1 Eigenvalues of continuum Dirac operator

Let D be the continuum massless Dirac operator. D is anti-Hermitian, so its eigenvalues are purely imaginary or zero:

$$D^\dagger = -D\,, \tag{3.1}$$

$$D\,|u_\lambda\rangle = i\lambda\,|u_\lambda\rangle\ , \tag{3.2}$$

where $\lambda \in \mathbb{R}$ represents an eigenvalue $i\lambda$, and $|u_\lambda\rangle$ is the corresponding eigenvector.

Thanks to the chiral symmetry,

$$\gamma_5 D = -D\gamma_5 \tag{3.3}$$

$$\Rightarrow D\gamma_5 \left|u_\lambda\right\rangle = -i\lambda\gamma_5 \left|u_\lambda\right\rangle \ . \tag{3.4}$$

Let us define $\left|u_{-\lambda}\right\rangle \equiv \gamma_5 \left|u_\lambda\right\rangle$, and then Eq. (3.4) implies $D\left|u_{-\lambda}\right\rangle = -i\lambda\left|u_{-\lambda}\right\rangle$. In other words, if there exists $\left|u_\lambda\right\rangle$, then its parity partner eigenstate $\left|u_{-\lambda}\right\rangle$ with negative eigenvalue $-i\lambda$ must exist accordingly as a pair except for zero modes with $\lambda = 0$.

3.1.2 Eigenvalues of staggered Dirac operator

The massless Dirac operator (D_s) of staggered fermions — Remind that in this thesis staggered fermions denote all (improved) staggered fermion formalisms collectively — is anti-Hermitian: $D_s^\dagger = -D_s$. Hence, its eigenvalues are purely imaginary or zero as in the continuum:

$$D_s \left|f_\lambda^s\right\rangle = i\lambda \left|f_\lambda^s\right\rangle \ , \tag{3.5}$$

where $\lambda \in \mathbb{R}$ represents an eigenvalue $i\lambda$, and $\left|f_\lambda^s\right\rangle$ is the corresponding eigenvector. Here, the superscript s represents staggered quarks.

In the meantime, the generator of $\mathrm{U(1)_A}$ axial symmetry conserved

for staggered fermions is given by

$$\begin{aligned}\Gamma_\epsilon(A,B,a,b) &\equiv [\gamma_5 \otimes \xi_5]_{AB;ab} \\ &= \overline{(\gamma_5 \otimes \xi_5)}_{AB} \cdot \delta_{ab} \\ &= \epsilon(A) \cdot \delta_{AB} \cdot \delta_{ab}\,, \end{aligned} \tag{3.6}$$

where A and B are hypercubic indices and a and b are color indices. The phase $\epsilon(A)$ is given by

$$\epsilon(A) \equiv (-1)^{\sum_{\mu=1}^{4} A_\mu}\,. \tag{3.7}$$

Γ_ϵ is often called "distance parity". Under this $\mathrm{U(1)_A}$ transformation, the staggered Dirac operator transforms as follows:

$$\Gamma_\epsilon D_s \Gamma_\epsilon = D_s^\dagger = -D_s\,, \tag{3.8}$$

$$\Gamma_\epsilon D_s = -D_s \Gamma_\epsilon\,. \tag{3.9}$$

Applying the latter anti-commutativity to Eq. (3.5), we find that

$$D_s \Gamma_\epsilon \left| f^s_{+\lambda} \right\rangle = -i\lambda\, \Gamma_\epsilon \left| f^s_{+\lambda} \right\rangle\,. \tag{3.10}$$

Hence, as in the continuum, $\left| f^s_{-\lambda} \right\rangle$ can be obtained from $\left| f^s_{+\lambda} \right\rangle$ through

Γ_ϵ transformation as follows:

$$\Gamma_\epsilon \left| f^s_{+\lambda} \right\rangle = e^{+i\theta} \left| f^s_{-\lambda} \right\rangle ,$$
$$\Gamma_\epsilon \left| f^s_{-\lambda} \right\rangle = e^{-i\theta} \left| f^s_{+\lambda} \right\rangle , \tag{3.11}$$

where θ is a real phase. If there exists an eigenvector of $\left| f^s_{+\lambda} \right\rangle$, there must be a corresponding parity partner of $\left| f^s_{-\lambda} \right\rangle$ due to the exact chiral symmetry Γ_ϵ. In other words, this Ward identity of Eq. (3.11) comes directly from the conserved $\mathrm{U(1)_A}$ axial symmetry.

3.2 Quark condensates

3.2.1 Quark condensate in the continuum

In the continuum, the quark condensate is given by

$$\langle \bar{\psi}\psi \rangle = \frac{1}{N_f} \sum_f \langle 0 | \bar{\psi}_f \psi_f | 0 \rangle \tag{3.12}$$
$$= -\frac{1}{V N_f} \int d^4x \, \mathrm{Tr} \left(\frac{1}{D+m} \right) , \tag{3.13}$$

where ψ_f is the quark field in the continuum with flavor f, D is the Dirac operator, m is the quark mass, x is the spacetime coordinate, V is the volume, and N_f is the number of flavors with the same mass m. The trace is a sum over spin and color.

Reminding subsection 3.1.1, by spectral decomposition [4],

$$
\begin{aligned}
S_f(x,y) &= \left\langle \psi_f(x)\bar{\psi}_f(y)\right\rangle \\
&= \sum_\lambda \frac{1}{i\lambda + m} u_\lambda(x) u_\lambda^\dagger(y)\,, \qquad (3.14)\\
\Rightarrow \left\langle \bar{\psi}\psi\right\rangle &= -\frac{1}{V}\sum_\lambda \frac{1}{i\lambda+m}\int d^4x\,\mathrm{Tr}\Big(u_\lambda(x)u_\lambda^\dagger(x)\Big) \qquad (3.15)\\
&= -\frac{1}{V}\sum_\lambda \frac{1}{i\lambda+m}\,, \qquad (3.16)
\end{aligned}
$$

where we adopt a normalization convention:

$$
\langle u_a | u_b\rangle = \int d^4x\; u_a^\dagger(x) u_b(x) = \delta_{ab}\,. \qquad (3.17)
$$

Let us separate the zero mode contribution from the spectral decomposition.

$$
\left\langle \bar{\psi}\psi\right\rangle = -\frac{1}{V}\sum_{\lambda>0}\frac{2m}{\lambda^2+m^2} - \frac{n_+ + n_-}{mV}\,. \qquad (3.18)
$$

Here, n_+ and n_- are the numbers of right-handed and left-handed zero modes per flavor, respectively, so that their sum corresponds to the number of total zero modes. Note that the zero mode contribution behaves as a simple pole in the chiral limit ($m \to 0$).

Now let us define the subtracted quark condensate $\langle\bar{\psi}\psi\rangle_{\rm sub}$:

$$\langle\bar{\psi}\psi\rangle_{\rm sub} = \langle\bar{\psi}\psi\rangle + \frac{n_+ + n_-}{mV} = -\frac{1}{V}\sum_{\lambda>0}\frac{2m}{\lambda^2+m^2} \tag{3.19}$$

$$= -\frac{1}{V}\sum_{n}\frac{2m}{\lambda_n^2+m^2} \quad \text{with} \quad \lambda_n > 0$$

$$= -\int_{-\infty}^{+\infty} d\lambda\,\frac{m}{\lambda^2+m^2}\,\rho_s(\lambda)\,, \tag{3.20}$$

where the spectral density $\rho_s(\lambda)$ is given by

$$\rho_s(\lambda) = \frac{1}{V}\sum_{n}\delta(\lambda-\lambda_n)\,, \tag{3.21}$$

which is determined on a single gauge configuration with volume V. Now let us average over a full ensemble of gauge field configurations and take the limit of infinite volume ($V\to\infty$). In that limit, the spectral density $\rho(\lambda) = \langle\rho_s(\lambda)\rangle$ has a well defined (smooth and continuous) value as $\lambda\to 0$. Then, we can define the chiral condensate as

$$\Sigma = -\langle 0|\bar{\psi}\psi|0\rangle_{\rm sub}\,(m=0)$$

$$= \lim_{m\to 0}\int_{-\infty}^{+\infty} d\lambda\,\frac{m}{\lambda^2+m^2}\,\rho(\lambda) = \pi\rho(0)\,. \tag{3.22}$$

The result is called the Banks-Casher relation [2]. Unlike the $\langle\bar{\psi}\psi\rangle$ in Eq. (3.18), the subtracted quark condensate $\langle\bar{\psi}\psi\rangle_{\rm sub}$ is expected to behave well in the chiral limit. Hence, in the numerical study on

the lattice, it is important to identify the would-be zero modes which correspond to the zero modes in the continuum limit, and remove them in the calculation of quark condensates.

3.2.2 Calculation of quark condensates on the lattice

Staggered fermions have four tastes per flavor by construction [23]. Hence, quark condensate for staggered fermions is defined as

$$\langle \bar{\chi}\chi \rangle = -\frac{1}{VN_t} \left\langle \mathrm{Tr}\, \frac{1}{D_s + m} \right\rangle_U , \tag{3.23}$$

where χ represents staggered quark fields, D_s is the staggered Dirac operator for a single valence flavor, V is the lattice volume, and N_t is the number of tastes. $\langle\ \rangle_U$ means an average over ensemble of gauge field (U) configurations.

The trace of propagator in Eq. (3.23) can be measured on the lattice by the following stochastic method.

$$(D_s + m)_{x,y}\chi(y) = \xi(x) \tag{3.24}$$

$$\Rightarrow \chi(x) = \left[\frac{1}{D_s + m}\right]_{x,y} \xi(y) \tag{3.25}$$

$$\Rightarrow\ \mathrm{Tr}\, \frac{1}{D_s + m} = \lim_{N_\xi \to \infty} \frac{1}{N_\xi} \sum_{\xi} \sum_{y} \xi^\dagger(y)\chi(y)\,, \tag{3.26}$$

where x, y are representative indices which represent the spacetime coordinate, taste, and color indices collectively. $\xi(x)$ is so called source

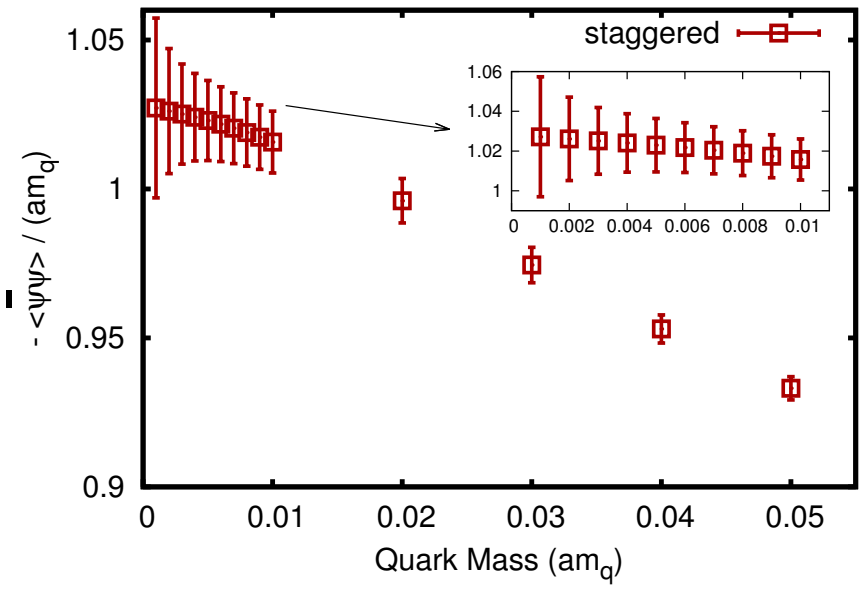

Figure 3.1: Quark condensates for staggered quarks. The Result is preliminary and unrenormalized bare. The measurement was done on a MILC asqtad lattice ensemble at $a \simeq 0.12$ fm with $m_l/m_s = 0.01/0.05$ [24]. Valence quarks are HYP-smeared staggered fermions.

vector, which represents either Gaussian random numbers or U(1) noise random numbers. The source vector must satisfy an identity:

$$\lim_{N_\xi \to \infty} \frac{1}{N_\xi} \sum_{\xi} \xi^\dagger(x)\xi(y) = \delta_{xy}\,, \tag{3.27}$$

where N_ξ is the number of the random vector samples. A preliminary measurement result of the quark condensate is presented in Fig. 3.1 [15].

As in the continuum case discussed in the previous subsection,

reminding subsection 3.1.2, the quark condensate of Eq. (3.23) can be rewritten by the spectral decomposition as follows:

$$\begin{aligned} S_{\rm stag}(x,y) &= \langle \chi(x)\bar{\chi}(y)\rangle \\ &= \sum_{\lambda} \frac{1}{i\lambda + m} f^{s}_{\lambda}(x) f^{s\dagger}_{\lambda}(y)\,, \qquad (3.28) \\ \Rightarrow \langle \bar{\chi}\chi\rangle &= -\frac{1}{VN_t}\sum_{\lambda}\frac{1}{i\lambda+m}\,\langle f^{s}_{\lambda}|f^{s}_{\lambda}\rangle \\ &= -\frac{1}{VN_t}\sum_{\lambda}\frac{1}{i\lambda+m}\,, \qquad (3.29) \end{aligned}$$

where the normalization condition $\langle f_\lambda | f_{\lambda'}\rangle = \int d^4x\; f^{s\dagger}_{\lambda}(x) f^{s}_{\lambda'}(x) = \delta_{\lambda\lambda'}$ is used. Separating out the zero mode contribution,

$$\langle \bar{\chi}\chi\rangle = -\frac{1}{VN_t}\sum_{\lambda>0}\frac{2m_v}{\lambda^2+m_v^2} - \frac{\tilde{n}_+ + \tilde{n}_-}{m_v VN_t}\,, \qquad (3.30)$$

where m_v is the valence quark mass, and $\tilde{n}_\pm$ are the numbers of zero modes with $P_\pm = \dfrac{1\pm\Gamma_\epsilon}{2}$ projection, respectively. In the second term of the right-hand side of Eq. (3.30), one can show that $\tilde{n}_+ + \tilde{n}_- = n_+ + n_-$, which means that total number of zero modes for staggered quarks is equal to that in the continuum [15]. Therefore, Eq. (3.30) can be rewritten as

$$\langle \bar{\chi}\chi\rangle = -\frac{1}{VN_t}\sum_{\lambda>0}\frac{2m_v}{\lambda^2+m_v^2} - \frac{n_+ + n_-}{m_v VN_t}\,. \qquad (3.31)$$

Now we define the subtracted quark condensate for staggered quarks:

$$\langle \bar{\chi}\chi \rangle_{\rm sub} = \langle \bar{\chi}\chi \rangle + \frac{n_+ + n_-}{m_v V N_t} \tag{3.32}$$

$$= \frac{1}{V N_t} \sum_{\lambda > 0} \frac{2m_v}{\lambda^2 + m_v^2} \,. \tag{3.33}$$

As in the continuum, the subtracted quark condensate behaves better than the original form as it approaches to the chiral limit ($m_v \to 0$). Hence, it is important to identify zero modes in the staggered fermion formulation.

3.3 Topological charge

3.3.1 Index theorem

In the continuum, the axial Ward identity is given by

$$\partial_\mu A_\mu(x) = 2mP(x) - 2N_f q(x) \,, \tag{3.34}$$

in the Euclidean spacetime [29]. Here $A_\mu \equiv \bar{\psi}\gamma_\mu\gamma_5\psi$ is the axial vector current in the flavor singlet representation, $P \equiv \bar{\psi}\gamma_5\psi$ is the corresponding pseudo-scalar operator, and $q \equiv \dfrac{1}{32\pi^2}\mathrm{Tr}\Big[F_{\mu\nu}\widetilde{F}_{\mu\nu}\Big]$ is the topological charge density (or winding number density). Now the topo-

logical charge Q can be expressed as

$$Q \equiv \int d^4x \, \langle q(x) \rangle \tag{3.35}$$

$$= -\frac{1}{2N_f} \int d^4x \, \langle \partial_\mu A_\mu(x) - 2mP(x) \rangle$$

$$= \frac{m}{N_f} \int d^4x \, \langle \bar{\psi}\gamma_5\psi \rangle \, . \tag{3.36}$$

The last equality can be rewritten by the spectral decomposition:

$$Q = -m \sum_\lambda \frac{1}{i\lambda + m} \int d^4x \, \left[u_\lambda^\dagger(x)\gamma_5 u_\lambda(x) \right] . \tag{3.37}$$

By the way, $\gamma_5 u_\lambda(x) = u_{-\lambda}(x)$, and so for $\lambda \neq 0$,

$$\int d^4x \, \left[u_\lambda^\dagger(x)\gamma_5 u_\lambda(x) \right] = \langle u_\lambda | u_{-\lambda} \rangle = 0 \, . \tag{3.38}$$

Therefore, only zero modes with $\lambda = 0$ contribute to Q. For the zero modes, it is convenient to choose the helicity eigenstates as the basis vectors so that $\langle u_0^L | \gamma_5 | u_0^L \rangle = -1$ and $\langle u_0^R | \gamma_5 | u_0^R \rangle = +1$, where the superscripts L, R represent left-handed and right-handed helicity, respectively. Then, it is straightforward to derive the index theorem [1]:

$$Q = n_- - n_+ \, , \tag{3.39}$$

where n_+ and n_- are the numbers of the right-handed and left-handed zero modes, respectively.

It is also possible to derive the index theorem from the transformation of the measure for the quark fields [29]. By a local transformation U, the quark field $\psi(x)$ transforms to $\psi'(x) = U(x)\psi(x)$ and its measure $\mathcal{D}\psi$ transforms as $\mathcal{D}\psi' = (\det \mathcal{U})^{-1}\mathcal{D}\psi$, where

$$\mathcal{U}_{xn,ym} \equiv U(x)_{nm}\delta^4(x-y)\,, \tag{3.40}$$

$$\bar{\mathcal{U}}_{xn,ym} \equiv \left[\gamma_4 U(x)^\dagger \gamma_4\right]_{nm} \delta^4(x-y)\,, \tag{3.41}$$

with indices n and m running over flavor and spin. Let us consider a local chiral transformation $U(x) = \exp[i\gamma_5\alpha(x)t]$, where t is a Hermitian matrix and $\alpha(x)$ is a real function of x. For this transformation, $\bar{\mathcal{U}} = \mathcal{U}$. When $\alpha(x) \ll 1$, we find that

$$\mathcal{D}\psi'\mathcal{D}\bar{\psi}' = (\det \mathcal{U})^{-2}\,\mathcal{D}\psi\mathcal{D}\bar{\psi} \tag{3.42}$$

$$= \exp\left[i\int d^4x\,\alpha(x)\mathcal{A}(x)\right]\,, \tag{3.43}$$

where

$$\mathcal{A}(x) \equiv -2\,\mathrm{tr}(\gamma_5 t)\delta^4(x-x)\,, \tag{3.44}$$

is the anomaly function. Here, the trace runs over flavor and spin.

Let us consider a smooth function $g(s)$ satisfying the following

properties:

$$g(0) = 1\,, \quad g(\infty) = 0\,,$$
$$sg'(s) = 0 \quad \text{at} \;\; s = 0 \;\; \text{and} \;\; s = \infty\,. \tag{3.45}$$

Using $g(s)$, $\mathcal{A}(x)$ can be rewritten as

$$\mathcal{A}(x) = -2\left[\mathrm{tr}\left(\gamma_5 t\, g\left(-\frac{D}{M^2}\right)\right)\delta^4(x-y)\right]_{y\to x}\,, \tag{3.46}$$

where M is a large mass so that Eq. (3.44) is recovered as $M \to \infty$. Making use of $\delta^4(x-y)\,\mathbb{1}_{4\times 4} = \sum_\lambda |u_\lambda(x)\rangle\,\langle u_\lambda(y)|$ for eigenvectors $u_\lambda(x)$ of D, the integral of $\mathcal{A}(x)$ gives

$$\begin{aligned}\int d^4x\,\mathcal{A}(x) &= -2\sum_\lambda t_\lambda\, g\left(\frac{\lambda^2}{M^2}\right)\langle u_\lambda(x)|\gamma_5|u_\lambda(x)\rangle \\ &\underset{m\to 0}{=} -2\sum_\lambda t_\lambda\,\langle u_\lambda(x)|\gamma_5|u_\lambda(x)\rangle\,,\end{aligned} \tag{3.47}$$

where $t\,|u_\lambda\rangle = t_\lambda\,|u_\lambda\rangle$. Here, we assume $[t, D] = 0$. Since $\langle u_\lambda(x)|\gamma_5|u_\lambda(x)\rangle = 0$ for $\lambda \neq 0$, only zero modes remains. Therefore,

$$\int d^4x\,\mathcal{A}(x) = -2\left[\sum_{\lambda=0_+} t_\lambda - \sum_{\lambda=0_-} t_\lambda\right]\,, \tag{3.48}$$

where $\lambda = 0_\pm$ represent zero modes of positive(0_+) and negative(0_-) chiralities, respectively.

In the meantime, following the steps in Ref. [29], a direct expansion of Eq. (3.46) results in

$$\mathcal{A}(x) = \frac{1}{16\pi^2} \operatorname{Tr}\left[F_{\mu\nu}\widetilde{F}_{\mu\nu}\right] \operatorname{tr}(t)\,. \tag{3.49}$$

For the special case of $t = \mathbb{1}$, combining Eqs. (3.48) and (3.49), we have the index theorem again:

$$Q = \frac{1}{32\pi^2} \int d^4x \, \operatorname{Tr}\left[F_{\mu\nu}\widetilde{F}_{\mu\nu}\right] = n_- - n_+\,. \tag{3.50}$$

3.3.2 Measurement of topological charge

On the lattice, the topological charge Q can be measured by a field-theoretic simulation directly from the definition of Eq. (3.35). A naive simplest calculation of Q is done by so called plaquette average which represents an average of closed 1×1 rectangular Wilson loops on the lattice:

$$Q = \frac{1}{32\pi^2} \sum_x \operatorname{Tr}\left[C^P_{\mu\nu}(x)\widetilde{C}^P_{\mu\nu}(x)\right]\,, \tag{3.51}$$

where the clover leaf operator $C^P_{\mu\nu}(x)$ for the 1×1 plaquette is given by

$$C^P_{\mu\nu}(x) = \frac{1}{4} \operatorname{Im}\left[\quad\right]\,. \tag{3.52}$$

Squares inside of the bracket represent 1×1 Wilson loops (plaquettes) around x, the black point at center, along with directions μ and ν. A

plaquette average in Eq. (3.51) gets an $\mathcal{O}(a^2)$ correction [30].

Based on this, improved versions of topological charge operators are discussed in Ref. [31–35]. Let us define a clover leaf operator $C^R_{\mu\nu}(x;m,n)$ for $m \times n$ (and $n \times m$) rectanglular Wilson loops:

$$C^R_{\mu\nu}(x;m,n) = \frac{1}{8}\,\mathrm{Im}\left[\right. \quad + \quad \left.\right] . \tag{3.53}$$

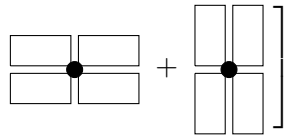

Here, the sizes of the rectangular clover leaves in the bracket are $m \times n$ (left) and $n \times m$ (right), respectively. Now we define an improved topological charge operator $Q_{\rm imp}$ [34, 35]:

$$\begin{aligned} Q_{\rm imp} &= \sum_{i=1}^{5} c_i Q_{m_i \times n_i} \,, \\ Q_{m\times n} &= \frac{1}{32\pi^2}\frac{1}{m^2 n^2}\sum_x \mathrm{Tr}\left[C^R_{\mu\nu}(x;m,n)\widetilde{C}^R_{\mu\nu}(x;m,n)\right] , \end{aligned} \tag{3.54}$$

where $(m_i, n_i) = (1,1), (2,2), (1,2), (1,3), (3,3)$ for $i = 1, \cdots, 5$ with parameters c_i's given by

$$\begin{aligned} c_1 &= \frac{19 - 55c_5}{9} , \quad c_2 = \frac{1 - 64c_5}{9} , \\ c_3 &= \frac{-64 + 640c_5}{45} , \quad c_4 = \frac{1}{5} - 2c_5 . \end{aligned} \tag{3.55}$$

$Q_{\rm imp}$ with the parameter set in Eq. (3.55) removes both $\mathcal{O}(a^2)$ and $\mathcal{O}(a^4)$ corrections. A particular choice of $c_5 = \dfrac{1}{20}$ is called 5-

loop-improved operator $Q(5\text{Li})$, which is known to behaves better compared with other choices such as $c_5 = 0$ ($Q(4\text{Li})$) and $c_5 = \frac{1}{10}$ ($Q(3\text{Li})$) [34, 35].

In practice, regardless of the improvement on the operator, a direct measurement of Q on a given gauge field configuration does not give an integer value as expected by the index theorem of Eq. (3.39). It is mainly because of ultraviolet(UV) fluctuations of the gauge field. There are several approaches of filtering out these UV fluctuations, such as cooling [34, 35], stout smearing [35], APE smearing [36, 37], HYP smearing [5], and gradient flow [38–40]. The most up-to-date status of these methods and their comparisons are given in Ref. [41]. In this thesis, APE smearing is chosen for its simplicity and efficiency.

In Figs. 3.2 and 3.3, examples of topological charge measurements are presented. Here, the evaluation of topological charge is monitored during $0 \sim 30$ iterations of APE smearing with $\alpha = 0.45$ [42]. In the plots, 'Plaquette' (red squares) represents the topological charge measured by the plaquette average as in Eq. (3.51) and '5Li' (blue circles) by the 5-loop-improved operator $Q(5\text{Li})$ defined in Eqs. (3.54) and (3.55) with $c_5 = \frac{1}{20}$. The results show that $Q(5\text{Li})$ operator converges faster and give more correct answer (integer) than the naive plaquette average method. In all cases, $Q(5\text{Li})$ requires less than 10 iterations of APE smearing to get a reasonable integer value. In this thesis, all numerical measurements of Q is obtained by $Q(5\text{Li})$ operator after

$10 \sim 30$ iterations of APE smearing with $\alpha = 0.45$.

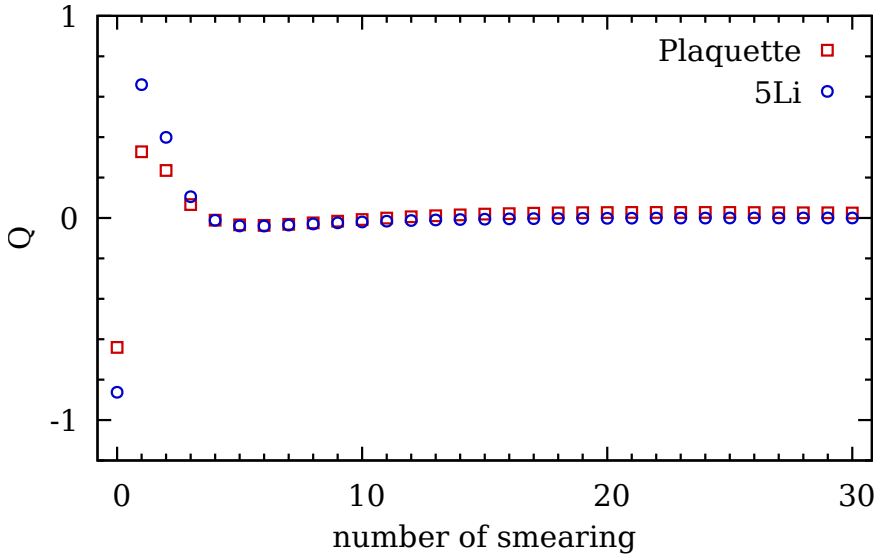

(a) $Q = 0$

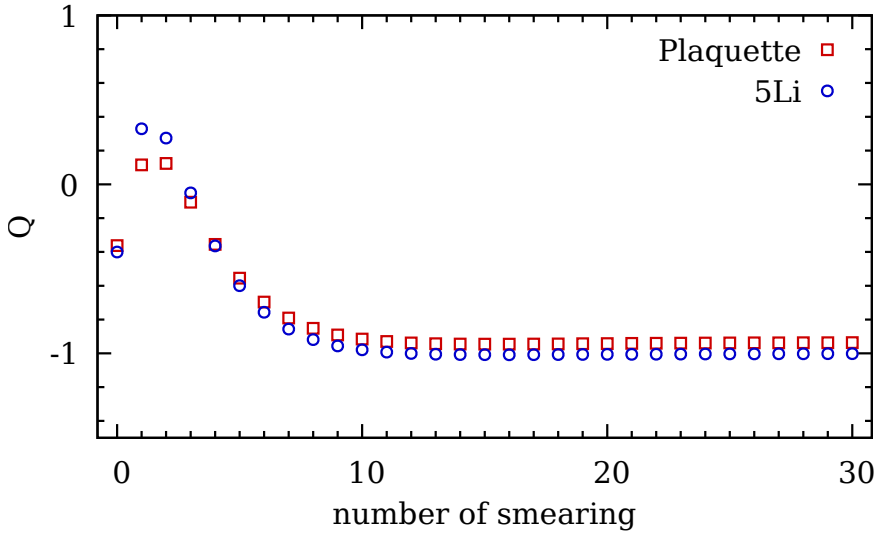

(b) $Q = -1$

Figure 3.2: Measurements of topological charge Q as increasing the number of APE smearing. Here, 'Plaquette' represents the plaquette average and '5Li' represents the 5-loop-improved operator $Q(5\mathrm{Li})$.

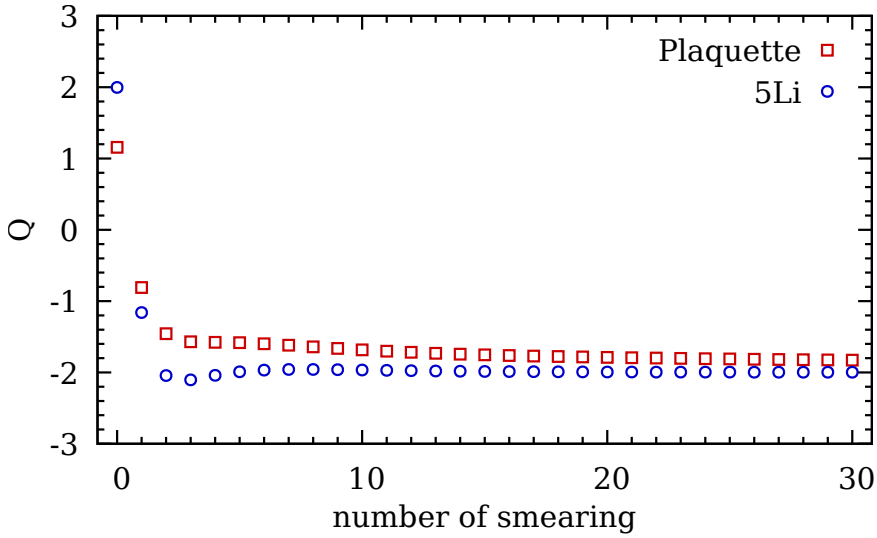

(a) $Q = -2$

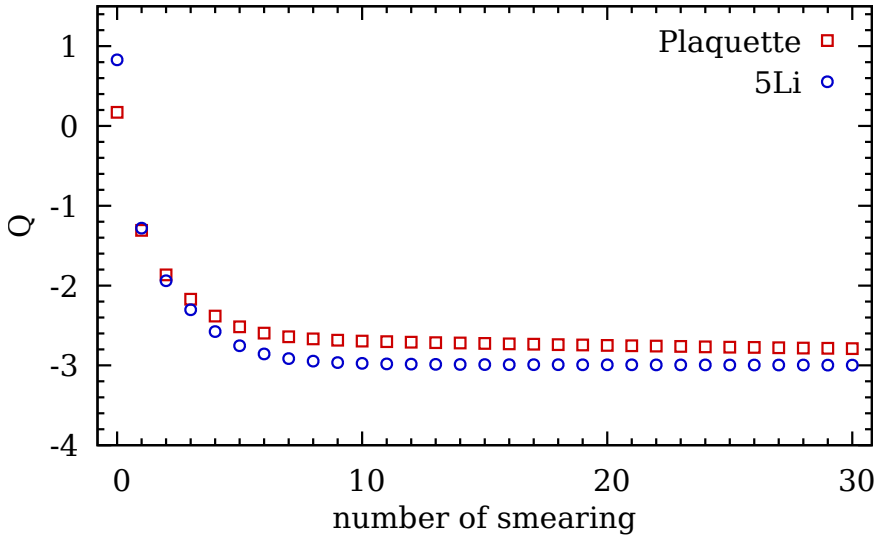

(b) $Q = -3$

Figure 3.3: Measurements of topological charge Q as increasing the number of APE smearing. The definitions of 'plaquette' and '5Li' are same with Fig. 3.2.

Chapter 4

Eigenvalue spectrum of staggered fermions

4.1 Calculation of eigenvalues and eigenvectors

4.1.1 Eigenvalues of $D_s^\dagger D_s$

Instead of calculating eigenvalues and eigenvectors of D_s directly, calculating those of $D_s^\dagger D_s$ has several advantages in practice. Reminding of discussions in Subsection 3.1.2 and the eigenvalue equation of D_s of Eq. (3.5), the eigenvalue equation of $D_s^\dagger D_s$ is given by

$$D_s^\dagger D_s \left| g_{\lambda^2}^s \right\rangle = \lambda^2 \left| g_{\lambda^2}^s \right\rangle . \tag{4.1}$$

where the $\left|g^s_{\lambda^2}\right\rangle$ state is a mixture of two eigenvectors: $\left|f^s_{+\lambda}\right\rangle$ and $\left|f^s_{-\lambda}\right\rangle$. In other words,

$$\left|g^s_{\lambda^2}\right\rangle = c_1 \left|f^s_{+\lambda}\right\rangle + c_2 \left|f^s_{-\lambda}\right\rangle \,, \tag{4.2}$$

where c_i are complex numbers and they satisfy the normalization condition:

$$|c_1|^2 + |c_2|^2 = 1 \,. \tag{4.3}$$

Since $D_s^\dagger D_s$ is Hermitian, its eigenvalues and eigenvectors can be computed by Lanczos algorithm [43]. Details on Lanczos and its improvements are discussed in Subsection 4.1.2.

Why is λ^2 preferred over $i\lambda$? The first reason is to use the even-odd preconditioning [44], which makes Lanczos run on only even or odd sites on the lattice. This leads to two benefits: one is that there is a substantial gain in the speed of the code and the other is that the code uses only half of the memory that is otherwise used. Details on the even-odd preconditioning are described in Subsection 4.1.3. The second reason is that it allows us to implement the polynomial acceleration algorithms [45] into Lanczos easier, since the eigenvalues of $D_s^\dagger D_s$ are positive definite, and have a lower bound of $\lambda^2 > 0$. Here, note that staggered fermions can have would-be zero modes whose eigenvalues are small and positive ($\lambda^2 > 0$) in rough gauge configurations. In other words, there is no exact zero modes ($\lambda = 0$) with staggered fermions on rough gauge configurations [46]. Details

on our implementation of polynomial acceleration are described in Subsection 4.1.2.

The Lanczos algorithm solves the eigenvalue equation of Eq. (4.1) and obtains the solution $\left|g^s_{\lambda^2}\right\rangle$ as well as the corresponding eigenvalue λ^2. To decompose $\left|g^s_{\lambda^2}\right\rangle$ into $\left|f^s_{+\lambda}\right\rangle$ and $\left|f^s_{-\lambda}\right\rangle$, let us define projection operators as

$$P_+ = (D_s + i\lambda)\,, \tag{4.4}$$

$$P_- = (D_s - i\lambda)\,. \tag{4.5}$$

P_+ is the projection operator to select only the $\left|f^s_{+\lambda}\right\rangle$ component and remove the $\left|f^s_{-\lambda}\right\rangle$ component, while P_- works the opposite way. Hence, applying $P_\pm$ to $\left|g^s_{\lambda^2}\right\rangle$ give us the $\left|f^s_{\pm\lambda}\right\rangle$ components of $\left|g^s_{\lambda^2}\right\rangle$:

$$\left|\tilde{f}_+\right\rangle = P_+ \left|g^s_{\lambda^2}\right\rangle\,, \tag{4.6}$$

$$\left|\tilde{f}_-\right\rangle = P_- \left|g^s_{\lambda^2}\right\rangle\,. \tag{4.7}$$

Now, the normalized eigenvectors are obtained as

$$\left|f^s_{+\lambda}\right\rangle = \frac{\left|\tilde{f}_+\right\rangle}{\sqrt{\left\langle \tilde{f}_+ \middle| \tilde{f}_+ \right\rangle}}\,, \tag{4.8}$$

$$\left|f^s_{-\lambda}\right\rangle = \frac{\left|\tilde{f}_-\right\rangle}{\sqrt{\left\langle \tilde{f}_- \middle| \tilde{f}_- \right\rangle}}\,. \tag{4.9}$$

4.1.2 Lanczos algorithm

Lanczos is a numerical algorithm to calculate eigenvalues and eigenvectors of a Hermitian matrix [43]. It transforms an $n \times n$ Hermitian matrix H into tridiagonal matrix T through a unitary transformation Q, which is represented by

$$T = Q^{\dagger} H Q \,. \tag{4.10}$$

Here, columns of Q are composed of basis vectors of n-th Krylov subspace $\mathcal{K}_n(H, b)$ generated by H and a starting vector b of our choice. Each iteration of Lanczos computes a column of Q and T in sequence. At the end, diagonalizing the tridiagonal matrix T yields eigenvalues and eigenvectors of H.

In principle, Lanczos is a direct method that takes n iterations to construct the $n \times n$ tridiagonal matrix T. However, since these columns of T are computed in order, a sequence of $m < n$ iterations also constructs an $m \times m$ tridiagonal matrix T' which is a submatrix of T. In practice, the real benefit of Lanczos is that eigenvalues of T' approximate some eigenvalues of T. As iteration continues and the size of the submatrix T' increases, eigenvalues of T' converge to eigenvalues of T. Their convergence condition is somewhat complicated. They converge to the largest, the smallest, or the most sparse eigenvalue first. The speed of convergence depends on the density of eigenvalues.

The less dense, the faster they converge.

In this thesis, two popular improvement techniques of Lanczos are implemented; (1) implicit restart [47] and (2) polynomial acceleration with Chebyshev polynomial [48]. The implicit restart method gets rid of converged eigenvalues in the middle of the Lanczos iteration. It takes effect as if we restarted the Lanczos with a shifted matrix H' given by

$$H' \equiv H - \sum_i \lambda_i \mathcal{I}, \tag{4.11}$$

where λ_i are eigenvalues we want to remove. Then H' is still Hermitian but does not have such eigenvalues λ_i. Hence, Lanczos with H' converges to remaining eigenvalues faster. Besides, the implicitly restarting procedure gives us a new submatrix, which has a reduced dimension $((m-r)\times(m-r))$ by the number of eigenvalues we have removed (r). Then we iterate Lanczos r times to refill the submatrix to restore the structure of $m \times m$ matrix. Then we repeat the implicit restart to obtain a new submatrix of $(m-r)\times(m-r)$, and so on. It allows us to control the size of submatrix, the computational cost and the memory usage while the submatrix T' contains $(m-r)$ eigenmodes more precise (much closer to the true eigenmodes of the full matrix H) for each iteration.

A polynomial operation on a matrix changes the eigenvalue spectrum accordingly while retaining the eigenvectors. Since the polyno-

mial of a Hermitian matrix is also Hermitian, Lanczos is still available to calculate its eigenvalues and eigenvectors. By choosing a proper polynomial, one can manipulate density of the eigenvalue spectrum so that the convergences to the desired eigenvalues are accelerated. Chebyshev polynomial is a popular choice for this purpose. Using the Chebyshev polynomial, one can map the first region of eigenmodes of no interest to $[-1, 1]$, and map the second region of eigenmodes of our interest to $[-\infty, -1]$. Chebyshev polynomial bounds the first region to $[-1, 1]$ where the eigenvalues are enough dense to make the Lanczos not converge. In addition, Chebyshev polynomial rapidly changes in the second region such that it makes the density of eigenmodes enough low to accelerate the convergence of Lanczos faster. To apply Chebyshev polynomial for $D_s^\dagger D_s$ whose eigenvalues are $\lambda^2 \geq 0$, one can set the lower bound of the first region to a value somewhat greater than the largest eigenvalue wanted. This strategy will not only suppress high unwanted eigenmodes but also accelerate the speed of Lanczos for the low eigenmodes of our interest.

In the meantime, numerical stability is essential for Lanczos algorithm. Each Lanczos iteration generates Lanczos vectors, which are column vectors of the unitary matrix Q in Eq. (4.10). After several iterations, however, Lanczos vectors lose their orthogonality due to gradual loss of numerical precision. This loss would induce spurious ghost eigenvalues [49]. A straightforward prescription to the prob-

lem is performing a reorthogonalization for every calculation of Lanczos vectors. There are also alternative approaches to eliminate those ghost eigenvalues without the reorthogonalization, such as Cullum-Willoughby method [50, 51]. For numerical simulations in this thesis, the full reorthogonalization is performed for each Lanczos iteration.

For a large scale simulation using Lanczos, Multi-Grid Lanczos [52] and Block Lanczos [53] are also available in the market [1]. Multi-Grid Lanczos is also based on the implicit restart and Chebyshev acceleration. Along with that, it reduces the memory requirement significantly by compressing the eigenvectors using their local coherence [54]. It constructs a spatially-blocked deflation subspace from some of the lowest eigenvectors of Dirac operator. Then the coherence of eigenvectors allows us to represent other eigenvectors on this subspace and run Lanczos with much less memory size. Meanwhile, Block Lanczos utilizes the Split Grid method [53]. This algorithm deals with multiple starting vectors for Lanczos, where the Split Grid method divides the domain of the Dirac operator application into multiple smaller domains so that each partial domain runs in parallel on a partial grid (lattice) with a lower surface to volume ratio compared to that of the full grid. Hence, one can optimize the off-node communication by adjusting the block (grid) size.

[1] These methods are not applied in this work. This paragraph is only for reference.

A more substantial description of the Lanczos iteration method is available in Appendix A.

4.1.3 Even-odd preconditioning and phase ambiguity

Even-odd preconditioning reorders a fermion field $\chi(x)$ so that even site fermion fields are obtained first, and odd site fermion fields are obtained from them:

$$\chi(x) = \begin{pmatrix} \chi_e \\ \chi_o \end{pmatrix} , \tag{4.12}$$

where χ_e (χ_o) is the fermion field collection on even (odd) sites. On this basis, the massless staggered Dirac operator D_s can be represented as a block matrix:

$$D_s = \begin{pmatrix} 0 & D_{eo} \\ D_{oe} & 0 \end{pmatrix} , \tag{4.13}$$

where D_{oe} (D_{eo}) relates even (odd) site fermion fields to odd (even) site fermion fields. Since $D_s^\dagger = -D_s$, one also find that $D_{oe}^\dagger = -D_{eo}$ and $D_{eo}^\dagger = -D_{oe}$.

On this basis, $D_s^\dagger D_s$ is expressed as

$$D_s^\dagger D_s = \begin{pmatrix} 0 & -D_{eo} \\ -D_{oe} & 0 \end{pmatrix} \begin{pmatrix} 0 & D_{eo} \\ D_{oe} & 0 \end{pmatrix} \tag{4.14}$$

$$= \begin{pmatrix} -D_{eo}D_{oe} & 0 \\ 0 & -D_{oe}D_{eo} \end{pmatrix} . \tag{4.15}$$

Hence, the eigenvalue equation of $D_s^\dagger D_s$ (Eq. (4.1)) can be divided into two eigenvalue equations as follows,

$$-D_{eo}D_{oe} \left|g_e\right\rangle = \lambda^2 \left|g_e\right\rangle , \tag{4.16}$$

$$-D_{oe}D_{eo} \left|g_o\right\rangle = \lambda^2 \left|g_o\right\rangle , \tag{4.17}$$

where $\left|g_{e(o)}\right\rangle$ is the collection of even (odd) site components of $\left|g^s_{\lambda^2}\right\rangle$. Here, the superscript s and the subscript λ^2 are omitted for notational simplicity. Now, multiplying D_{oe} from the left on both sides of Eq. (4.16) gives

$$-D_{oe}D_{eo}(D_{oe} \left|g_e\right\rangle) = \lambda^2 (D_{oe} \left|g_e\right\rangle) , \tag{4.18}$$

which is identical to Eq. (4.17). Hence, we find that $\left|g_o\right\rangle = \eta\, D_{oe} \left|g_e\right\rangle$ where $\eta = re^{i\alpha}$ is an arbitrary complex number with $r > 0$ and $0 \leq \alpha < 2\pi$. Here, r represents the scaling behavior and α represents a random phase. Since $-D_{eo}D_{oe} (= D_{oe}^\dagger D_{oe})$ is Hermitian and

positive semi-definite, one can solve Eq. (4.16) using the Lanczos algorithm introduced in Subsection 4.1.2. From the result of $|g_e\rangle$, it is straightforward to obtain the eigenvector $\left|g^s_{\lambda^2}\right\rangle$ of Eq. (4.1) as follows,

$$\left|g^s_{\lambda^2}\right\rangle = \begin{pmatrix} |g_e\rangle \\ \eta\, D_{oe}\,|g_e\rangle \end{pmatrix} . \tag{4.19}$$

where η is a random complex number in general.

Now, let us apply the projection operator P_+, defined in Eq. (4.4), to $\left|g^s_{\lambda^2}\right\rangle$. Using Eq. (4.16), we find that

$$\begin{aligned} \left|\tilde{f}_+\right\rangle = P_+\left|g^s_{\lambda^2}\right\rangle &= \begin{pmatrix} i\lambda & D_{eo} \\ D_{oe} & i\lambda \end{pmatrix} \begin{pmatrix} |g_e\rangle \\ \eta\, D_{oe}\,|g_e\rangle \end{pmatrix} \\ &= (1+i\eta\lambda) \begin{pmatrix} i\lambda\,|g_e\rangle \\ D_{oe}\,|g_e\rangle \end{pmatrix} . \end{aligned} \tag{4.20}$$

Similarly, for the projection operator P_- defined in Eq. (4.5), we find that

$$\left|\tilde{f}_-\right\rangle = P_-\left|g^s_{\lambda^2}\right\rangle = (1-i\eta\lambda) \begin{pmatrix} -i\lambda\,|g_e\rangle \\ D_{oe}\,|g_e\rangle \end{pmatrix} . \tag{4.21}$$

Since η only appears in the overall factor for both cases, it gives only the relative phase difference between the normalized eigenvectors $\left|f^s_{\pm\lambda}\right\rangle$ defined in Eqs. (4.8) and (4.9).

We can proceed further to obtain the eigenvectors $\left|f^s_{\pm\lambda}\right\rangle$. The norm of $\left|\tilde{f}_+\right\rangle$ is given by

$$\left\langle \tilde{f}_+ \middle| \tilde{f}_+ \right\rangle = [(1 - i\eta^*\lambda)(1 + i\eta\lambda)] \cdot 2\lambda^2 \langle g_e | g_e \rangle \ . \tag{4.22}$$

Hence, $\left|f^s_{+\lambda}\right\rangle$ is

$$\left|f^s_{+\lambda}\right\rangle = \frac{1}{N}\sqrt{\frac{1 + i\eta\lambda}{1 - i\eta^*\lambda}} \begin{pmatrix} i\lambda \ |g_e\rangle \\ D_{oe} \, |g_e\rangle \end{pmatrix} , \tag{4.23}$$

where

$$N \equiv \sqrt{2\lambda^2 \langle g_e | g_e \rangle} \, . \tag{4.24}$$

Similarly,

$$\left|f^s_{-\lambda}\right\rangle = \frac{1}{N}\sqrt{\frac{1 - i\eta\lambda}{1 + i\eta^*\lambda}} \begin{pmatrix} -i\lambda \ |g_e\rangle \\ D_{oe} \, |g_e\rangle \end{pmatrix} . \tag{4.25}$$

These results for $\left|f^s_{\pm\lambda}\right\rangle$ indicate that the phase difference θ for Γ_ϵ transformation defined in Eq. (3.11) depends on the value of η.

For numerical simulations in this thesis, η is set to $\eta = re^{i\alpha} = 1$: $r = 1$ and $\alpha = 0$. Hence, the relative random phase between $\left|f^s_{\pm\lambda}\right\rangle$ states is removed by hand. Therefore, the phase θ defined in Eq. (3.11) contains a bias from the choice of $\eta = 1$.

For $\eta = 1$ (our choice), $\Gamma_\epsilon \left| f^s_{+\lambda} \right\rangle$ is

$$\Gamma_\epsilon \left| f^s_{+\lambda} \right\rangle = \frac{1}{N} \sqrt{\frac{1+i\lambda}{1-i\lambda}} \begin{pmatrix} i\lambda \, |g_e\rangle \\ -D_{oe} \, |g_e\rangle \end{pmatrix} , \tag{4.26}$$

while $\left| f^s_{-\lambda} \right\rangle$ is

$$\left| f^s_{-\lambda} \right\rangle = \frac{1}{N} \sqrt{\frac{1-i\lambda}{1+i\lambda}} \begin{pmatrix} -i\lambda \, |g_e\rangle \\ D_{oe} \, |g_e\rangle \end{pmatrix} . \tag{4.27}$$

Then the following contraction gives $e^{i\theta}$ as follows,

$$\begin{aligned} \left\langle f^s_{-\lambda} \right| \Gamma_\epsilon \left| f^s_{+\lambda} \right\rangle &= \frac{1}{N^2} \sqrt{\left(\frac{1-i\lambda}{1+i\lambda} \right)^* \frac{1+i\lambda}{1-i\lambda}} \cdot (-N^2) \\ &= -\frac{1+i\lambda}{1-i\lambda} \\ &= e^{i(\pi+2\beta)} = e^{i\theta} , \end{aligned} \tag{4.28}$$

where $\beta \equiv \arctan(\lambda)$. From Eq. (3.11), we find that

$$\theta = \pi + 2\beta . \tag{4.29}$$

In Fig. 4.1, we measure the phase θ for hundreds of eigenvectors on a gauge configuration with $Q = -1$. Here, red circles represent numerical results and the blue line represents the prediction from the theory in Eq. (4.29). The results are consistent with our theoretical

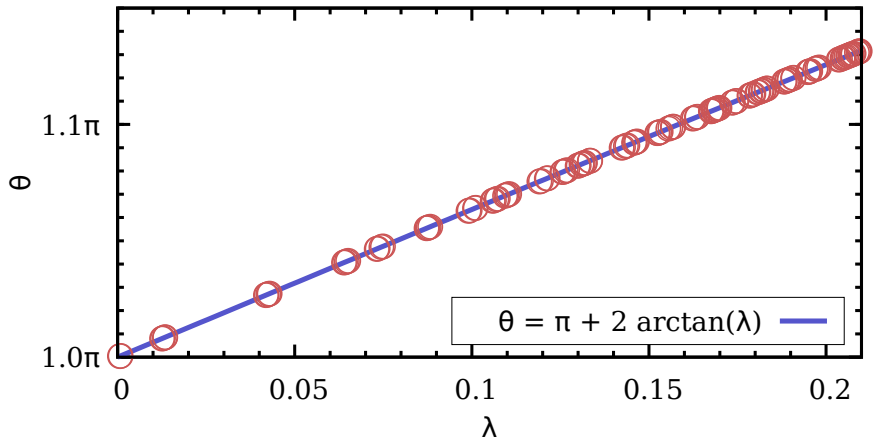

Figure 4.1: The phase θ as a function of λ. Red circle symbols represent numerical results for θ. The blue line represents the prediction from the theory. Here, we use a gauge configuration with $Q = -1$ for the measurement.

prediction within numerical precision.

4.2 Eigenvalue spectrum: numerical results

In this section, numerical results of eigenvalue spectrum of staggered Dirac operator are discussed. In Table 4.1, input parameters for this study are given. The same parameter set is applied to all numerical simulations in this thesis.

4.2.1 Eigenvalue spectrum for $Q = 0$ and $Q = -1$

An example of eigenvalue spectrum for $Q = 0$ is presented in Fig. 4.2. Since $Q = 0$, it is not expected to find any zero modes for this gauge configuration. In Fig. 4.2(a), eigenvalues of λ^2 for eigenvectors $\left|g^s_{\lambda^2}\right\rangle$

Table 4.1: Input parameters for numerical study in quenched QCD. For more details, refer to Ref. [9].

parameters	values
gluon action	tree level Symanzik [33, 55, 56]
tadpole improvement	yes
β	5.0
geometry	20^4
a	0.077(1) fm [57]
$1/a$	2.6 GeV
valence quarks	HYP staggered fermions [6, 58, 59]
N_f	$N_f = 0$ (quenched QCD)

defined in Eq. (4.1) are shown. Here, one observes eight-fold degeneracy for non-zero eigenmodes due to the conserved $\mathrm{U(1)_A}$ axial symmetry. Note that $\lambda_2 = -\lambda_1$ and, in general, $\lambda_{2n} = -\lambda_{2n-1}$ for $n > 0$ and $n \in Z$. In other words, λ_{2n} is the parity partner of λ_{2n-1}. For each λ_i, there exists four-fold degeneracy due to approximate SU(4) taste symmetry. This set of four degenerate eigenvalues is denoted quartet. For each of these four-fold degenerate eigenvalues (for example $\lambda_1, \lambda_3, \lambda_5, \lambda_7$ in Fig. 4.2(a)), there exists a parity partner eigenvalue due to the $\mathrm{U(1)_A}$ symmetry: $\lambda_2 = -\lambda_1$, $\lambda_4 = -\lambda_3$, $\lambda_6 = -\lambda_5$, and $\lambda_8 = -\lambda_7$ (refer to Fig. 4.2(b)).

Let us turn to the $Q = -1$ example. Since $Q = -1$, it is expected to observe four-fold would-be zero modes. Because the gauge configurations are rough, one can observe not exact zero modes but would-be zero modes. Fig. 4.3 demonstrates how the would-be zero modes be-

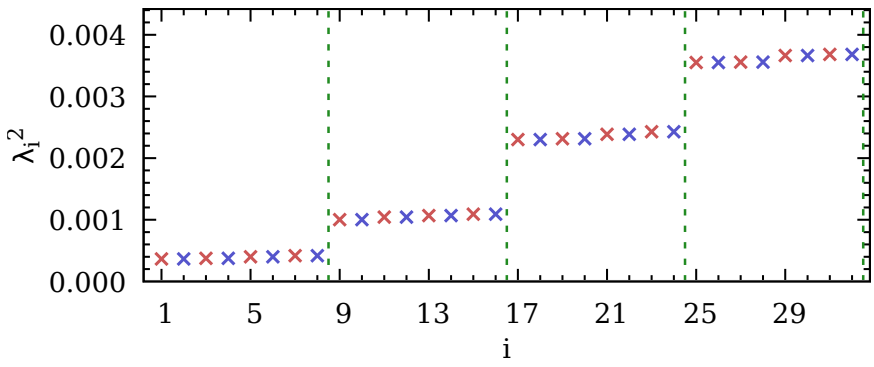

(a) λ_i^2

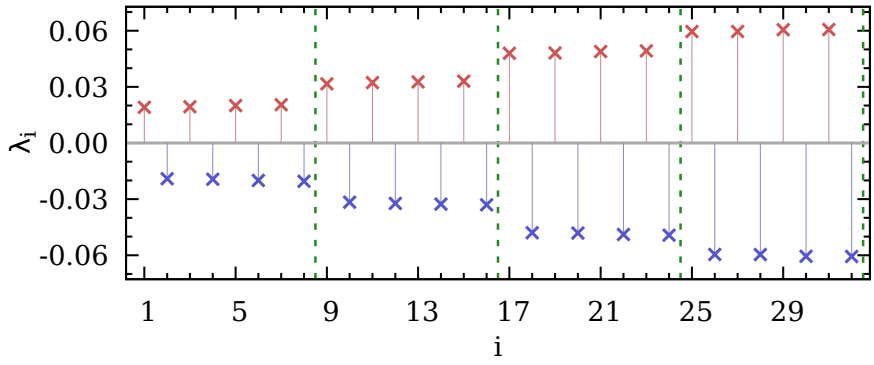

(b) λ_i

Figure 4.2: Eigenvalue spectrum of staggered Dirac operator on a $Q = 0$ gauge configuration.

have on the gauge configuration with $Q = -1$. In Fig. 4.3(a) and 4.3(b), one can easily find a quartet of four-fold degenerate would-be zero modes: $\lambda_1, \lambda_2, \lambda_3, \lambda_4$. In addition, thanks to the $\mathrm{U(1)_A}$ chiral Ward identity in Eq. (3.11), they satisfy $\lambda_2 = -\lambda_1$ and $\lambda_4 = -\lambda_3$. As in the case of $Q = 0$, non-zero eigenmodes are eight-fold degenerate. These patterns of four-fold degeneracy for would-be zero modes and

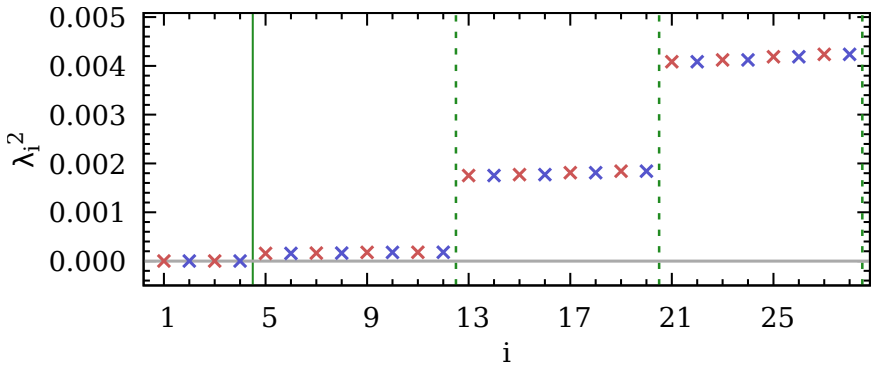

(a) λ_i^2

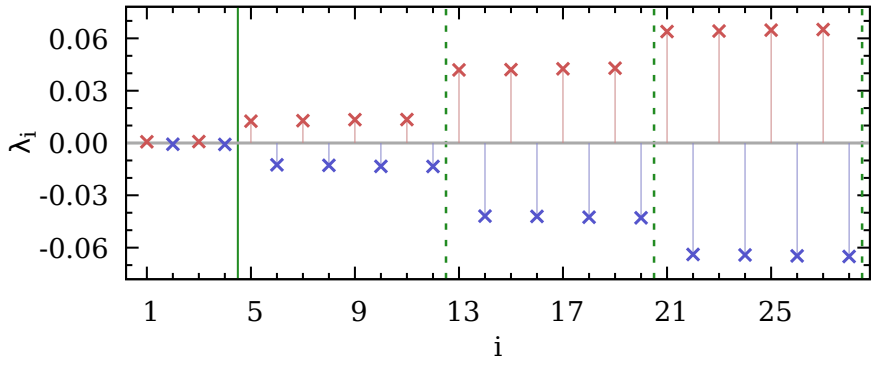

(b) λ_i

Figure 4.3: Eigenvalue spectrum of staggered Dirac operator on a $Q = -1$ gauge configuration.

eight-fold degeneracy for non-zero modes are also observed in the case of $Q = -2$ and $Q = -3$, which are presented in Subsection 4.2.2.

At this point, you might have already concluded that we can distinguish would-be zero modes of staggered quarks from non-zero modes by counting the degeneracy of the eigenvalues [8,9,60]. This is true but has some possibility to lead to a wrong answer in practice. The reason

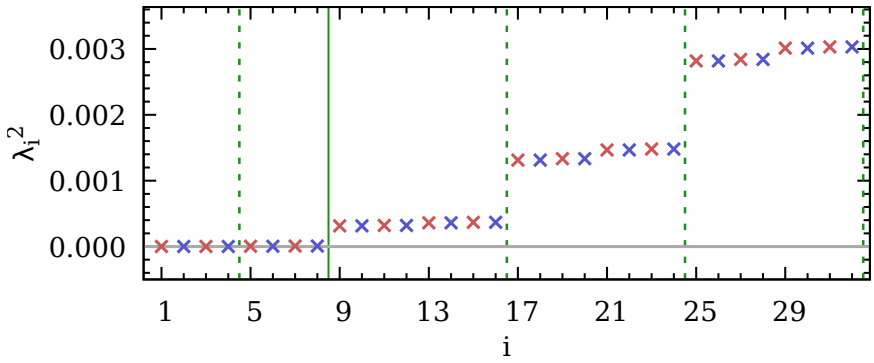

(a) λ_i^2

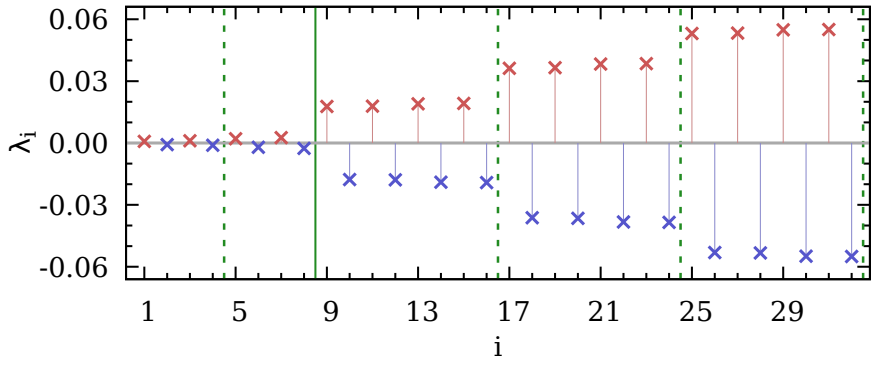

(b) λ_i

Figure 4.4: The same as Fig. 4.2 except for $Q = -2$.

is that, on large lattices, the eigenvalues are so dense that it is not easy to distinguish four-fold and eight-fold degeneracies in our eyes. Hence, we need a significantly more robust method to identify would-be zero modes and non-zero modes in staggered fermion formalism.

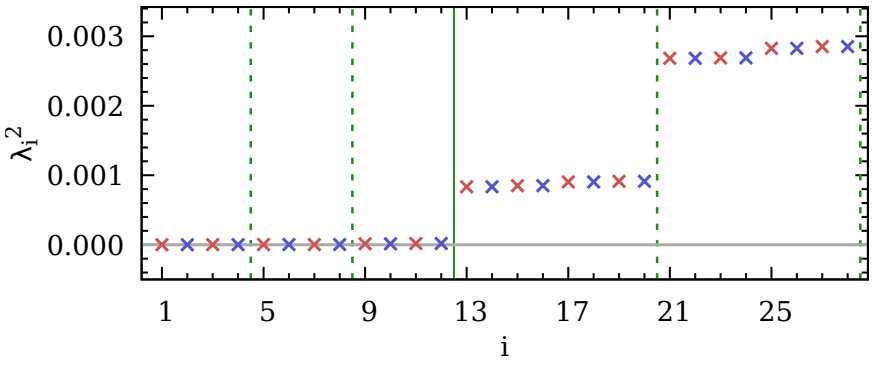

(a) λ_i^2

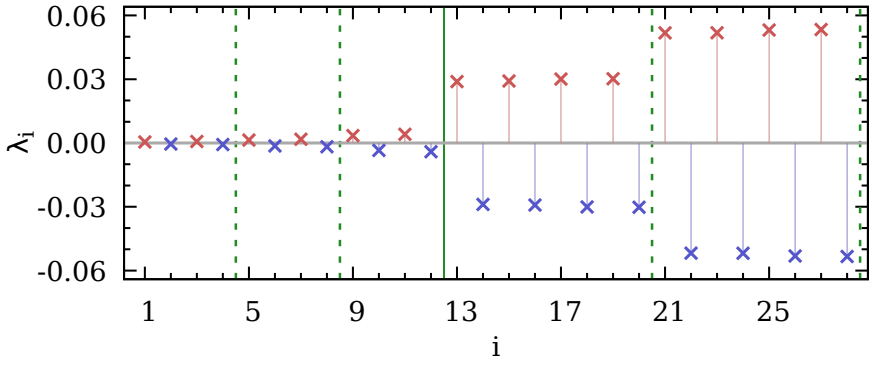

(b) λ_i

Figure 4.5: The same as Fig. 4.2 except for $Q = -3$.

4.2.2 Eigenvalue spectrum for $Q = -2$ and $Q = -3$

In Figs. 4.4 and 4.5, examples of the eigenvalue spectrums are presented for $Q = -2$ and $Q = -3$, respectively. Figs. 4.4(a) and 4.5(a) show eigenvalues λ^2 for eigenvectors $\left|g^s_{\lambda^2}\right\rangle$ defined in Eq. (4.1). In Fig. 4.4, one can find two sets of four-fold degenerate eigenstates: $\{\lambda_1, \lambda_2, \lambda_3, \lambda_4\}$ and $\{\lambda_5, \lambda_6, \lambda_7, \lambda_8\}$. Each of them indicates a quartet of would-be zero modes. The number of quartets corresponds to

the topological charge $Q = -2$, which corresponds to the index theorem of Eq. (3.39) when all would-be zero modes are assumed to have the same sign of chirality, i.e., $n_- = 0$ and $n_+ = 2$. Apart from the would-be zero modes, non-zero modes are observed to be eight-fold degenerate as in the cases of $Q = 0$ (Fig. 4.2) and $Q = -1$ (Fig. 4.3).

Similarly, in Fig. 4.5, one can find three quartets of would-be zero modes with $n_- = 0$ and $n_+ = 3$ ($Q = -3$): $\{\lambda_1, \lambda_2, \lambda_3, \lambda_4\}$, $\{\lambda_5, \lambda_6, \lambda_7, \lambda_8\}$, and $\{\lambda_9, \lambda_{10}, \lambda_{11}, \lambda_{12}\}$. Because the number of quartets equals the absolute value of the topological charge $|Q| = 3$, it is possible to deduce that all the would-be zero modes have the same sign of chirality in accordance with the index theorem of Eq. (3.39), i.e., $n_- = 0$ and $n_+ = 3$. For non-zero modes, the pattern of eight-fold degeneracy is observed as in other examples for $Q = 0$ in Fig. 4.2, $Q = -1$ in Fig. 4.3, and $Q = -2$ in Fig. 4.4.

Chapter 5

Chiral symmetry of staggered fermions

5.1 Chirality of staggered fermions

5.1.1 Chirality operator

In order to simplify the notation, let us introduce the following convention for eigenvalue indices:

$$D_s \left| f_j \right\rangle = i\lambda_j \left| f_j \right\rangle \ , \tag{5.1}$$

where $\left| f_j \right\rangle = \left| f^s_{\lambda_j} \right\rangle$ which is defined in Eq. (3.5). Considering the relevance with the continuum QCD with SU(4) flavor symmetry, a natural definition of chirality for staggered fermions is given by the taste

singlet form:

$$\begin{aligned}\Gamma_5(\lambda_i,\lambda_j) &\equiv \langle f_i|[\gamma_5\otimes 1]|f_j\rangle \\ &\equiv \sum_x [f^s_{\lambda_i}(x_A)]^\dagger\,[\gamma_5\otimes 1]_{AB}\,f^s_{\lambda_j}(x_B) \\ &= \sum_x [f^s_{\lambda_i}(x_A)]^\dagger\,\overline{(\gamma_5\otimes 1)}_{AB}\,U(x_A,x_B)\,f^s_{\lambda_j}(x_B)\,, \qquad (5.2)\end{aligned}$$

where x_A and $[\gamma_5\otimes 1]$ are defined in Eqs. (2.16)-(2.18), and λ_i and λ_j represent eigenvalues of D_s. The phase $\overline{(\gamma_5\otimes 1)}$ is given by

$$\overline{(\gamma_5\otimes 1)}_{AB} = \frac{1}{4}\,\mathrm{Tr}\Big(\gamma_A^\dagger\gamma_5\gamma_B\Big)\,. \qquad (5.3)$$

Here,

$$\begin{aligned}&\gamma_A^\dagger\gamma_5\gamma_B \\ &= (\gamma_4^{A_4}\gamma_3^{A_3}\gamma_2^{A_2}\gamma_1^{A_1})\,\gamma_5\,(\gamma_1^{B_1}\gamma_2^{B_2}\gamma_3^{B_3}\gamma_4^{B_4}) \qquad (5.4)\\ &= (-1)^{A_1+A_2+A_3+A_4}(-1)^{(A_1+B_1)(A_2+A_3+A_4)}(-1)^{(A_2+B_2)(A_3+A_4)}(-1)^{(A_3+B_3)(A_4)} \\ &\quad \gamma_5\,\gamma_1^{A_1+B_1}\gamma_2^{A_2+B_2}\gamma_3^{A_3+B_3}\gamma_4^{A_4+B_4}\,. \qquad (5.5)\end{aligned}$$

Since $\mathrm{Tr}\Big(\gamma_5\,\gamma_1^{A_1+B_1}\gamma_2^{A_2+B_2}\gamma_3^{A_3+B_3}\gamma_4^{A_4+B_4}\Big)$ does not vanish only for $(A_1+B_1)\%2=(A_2+B_2)\%2=(A_3+B_3)\%2=(A_4+B_4)\%2=1$,

$$
\begin{aligned}
&\mathrm{Tr}\Big(\gamma_A^\dagger\gamma_5\gamma_B\Big)\\
&=\mathrm{Tr}\big[\delta_{\,\overline{A}B}(-1)^{A_1+A_2+A_3+A_4}(-1)^{A_2+A_3+A_4}(-1)^{A_3+A_4}(-1)^{A_4}\gamma_5\gamma_1\gamma_2\gamma_3\gamma_4\big]\\
&=\delta_{\,\overline{A}B}(-1)^{A_1}(-1)^{A_1+A_2}(-1)^{A_1+A_2+A_3}\,\mathrm{Tr}\big({\gamma_5}^2\big)\\
&=4\,\delta_{\,\overline{A}B}\,\eta_1(A)\,\eta_2(A)\,\eta_3(A)\,\eta_4(A)\,, \qquad (5.6)
\end{aligned}
$$

where $\overline{A}_\mu=(A_\mu+1)\ \%\ 2$, and $\eta_\mu(A)=(-1)^{\sum_{\nu<\mu}A_\nu}$. Let us define $\eta_5(A)\equiv\eta_1(A)\,\eta_2(A)\,\eta_3(A)\,\eta_4(A)$, then this reduces to $\eta_5(A)=(-1)^{A_1+A_3}$. Hence,

$$
\overline{(\gamma_5\otimes 1)}_{AB}=\delta_{\,\overline{A}B}\,\eta_5(A)\,. \qquad (5.7)
$$

Inserting this into Eq. (5.2) gives

$$
\langle f_i|[\gamma_5\otimes 1]|f_j\rangle=\sum_x\,[f^s_{\lambda_i}(x_A)]^\dagger\,\eta_5(A)\,U(x_A,x_{\,\overline{A}})\,f^s_{\lambda_j}(x_{\,\overline{A}})\,. \qquad (5.8)
$$

Here, $U(x_A,x_{\,\overline{A}})$ is called a distance-4 link since the minimum number of links connecting A and $\overline{A}$ is four.

An important consequence of this definition of the chirality operator is that the following relationships hold as the continuum chirality

operator γ_5 does.

$$[\gamma_5 \otimes 1]^{2n+1} = [\gamma_5 \otimes 1]\,, \tag{5.9}$$

$$[\gamma_5 \otimes 1]^{2n} = [1 \otimes 1]\,, \tag{5.10}$$

$$\left[\frac{1}{2}(1 \pm \gamma_5) \otimes 1\right]^n = \left[\frac{1}{2}(1 \pm \gamma_5) \otimes 1\right]\,, \tag{5.11}$$

$$\left[\frac{1}{2}(1 + \gamma_5) \otimes 1\right]\left[\frac{1}{2}(1 - \gamma_5) \otimes 1\right] = 0\,, \tag{5.12}$$

where $n \geq 0$ and $n \in \mathbb{Z}$. A rigorous proof of Eqs. (5.9)-(5.12) is given in Subsection 5.1.2.

In addition to the chirality operator $\Gamma_5 = [\gamma_5 \otimes 1]$, let us also consider the following spin singlet operator $[1 \otimes \xi_5]$:

$$\begin{aligned}
\Xi_5(\lambda_i, \lambda_j) &\equiv \langle f_i | [1 \otimes \xi_5] | f_j \rangle \\
&\equiv \sum_x [f^s_{\lambda_i}(x_A)]^\dagger [1 \otimes \xi_5]_{AB}\, f^s_{\lambda_j}(x_B) \\
&= \sum_x [f^s_{\lambda_i}(x_A)]^\dagger\, \overline{(1 \otimes \xi_5)}_{AB}\, U(x_A, x_B)\, f^s_{\lambda_j}(x_B)\,.
\end{aligned} \tag{5.13}$$

$\Xi_5 \equiv [1 \otimes \xi_5]$ is named as "(maximal) shift operator". The phase $\overline{(1 \otimes \xi_5)}$ is given by

$$\overline{(1 \otimes \xi_5)}_{AB} = \frac{1}{4}\ \mathrm{Tr}\Big(\gamma_A^\dagger \gamma_B \gamma_5\Big)\,. \tag{5.14}$$

Here,

$$\gamma_A^\dagger \gamma_B \gamma_5 = (\gamma_4^{A_4}\gamma_3^{A_3}\gamma_2^{A_2}\gamma_1^{A_1})(\gamma_1^{B_1}\gamma_2^{B_2}\gamma_3^{B_3}\gamma_4^{B_4})\gamma_5 \tag{5.15}$$

$$= (-1)^{(A_1+B_1)(A_2+A_3+A_4)}(-1)^{(A_2+B_2)(A_3+A_4)}(-1)^{(A_3+B_3)(A_4)}$$
$$\gamma_1^{A_1+B_1}\gamma_2^{A_2+B_2}\gamma_3^{A_3+B_3}\gamma_4^{A_4+B_4}\gamma_5\,. \tag{5.16}$$

As before, this term survives only when $(A_1+B_1)\%2 = (A_2+B_2)\%2 = (A_3+B_3)\%2 = (A_4+B_4)\%2 = 1$. Hence,

$$\mathrm{Tr}\Big(\gamma_A^\dagger \gamma_B \gamma_5\Big)$$
$$= \mathrm{Tr}\big[\delta_{\overline{A}B}(-1)^{A_2+A_3+A_4}(-1)^{A_3+A_4}(-1)^{A_4}\gamma_1\gamma_2\gamma_3\gamma_4\gamma_5\big] \tag{5.17}$$
$$= 4\,\delta_{\overline{A}B}\,\zeta_1(A)\,\zeta_2(A)\,\zeta_3(A)\,\zeta_4(A)\,, \tag{5.18}$$

where $\zeta_\mu(A) = (-1)^{\sum_{\nu>\mu} A_\nu}$. Let us define $\zeta_5(A) \equiv \zeta_1(A)\,\zeta_2(A)\,\zeta_3(A)\,\zeta_4(A)$, then this reduces to $\zeta_5(A) = (-1)^{A_2+A_4}$. Therefore,

$$\overline{(1\otimes\xi_5)}_{AB} = \delta_{\overline{A}B}\,\zeta_5(A)\,. \tag{5.19}$$

Inserting this into Eq. (5.13) gives the final result:

$$\langle f_i|[1\otimes\xi_5]|f_j\rangle = \sum_x [f^s_{\lambda_i}(x_A)]^\dagger\ \zeta_5(A)\ U(x_A, x_{\overline{A}})\ f^s_{\lambda_j}(x_{\overline{A}})\,. \tag{5.20}$$

Here, $U(x_A, x_{\overline{A}})$ is again a distance-4 link as in Eq. (5.8).

Shift operator also satisfies the recursion relations:

$$[1 \otimes \xi_5]^{2n+1} = [1 \otimes \xi_5]\,, \tag{5.21}$$

$$[1 \otimes \xi_5]^{2n} = [1 \otimes 1]\,, \tag{5.22}$$

where $n \geq 0$ and $n \in \mathbb{Z}$. Another good property inherent to our definitions of the chirality operator and the shift operator is that the conserved $\mathrm{U(1)_A}$ axial symmetry transformation can be decomposed into their product:

$$\begin{aligned} \Gamma_\epsilon &\equiv [\gamma_5 \otimes \xi_5] \\ &= [\gamma_5 \otimes 1][1 \otimes \xi_5] \\ &= [1 \otimes \xi_5][\gamma_5 \otimes 1]\,. \end{aligned} \tag{5.23}$$

One can show that the following relations also hold:

$$\Gamma_\epsilon[\gamma_5 \otimes 1] = [\gamma_5 \otimes 1]\Gamma_\epsilon = [1 \otimes \xi_5]\,, \tag{5.24}$$

$$\Gamma_\epsilon[1 \otimes \xi_5] = [1 \otimes \xi_5]\Gamma_\epsilon = [\gamma_5 \otimes 1]\,. \tag{5.25}$$

Eqs. (5.23)-(5.25) are Ward identities of the conserved $\mathrm{U(1)_A}$ axial symmetry for staggered fermions.

Our definition of the chirality operator is different from Golterman's definition described in Subsection 2.3.2. As a true irreducible

representation of the lattice rotational symmetry group [28, 61, 62], Golterman's definition of the chirality operator has been conventionally used such as in Refs. [8, 13, 46]. However, due to its complexity, Golterman's operator does not satisfy the recursion relations of Eqs. (5.9)-(5.12) and the chiral Ward identities of Eqs. (5.23)-(5.25).

Before closing this subsection, let us simplify the notation for later use:

$$(\Gamma_5)^i_j \equiv \Gamma_5(\lambda_i, \lambda_j)\,, \tag{5.26}$$

$$|\Gamma_5|^i_j \equiv |\Gamma_5(\lambda_i, \lambda_j)|\,, \tag{5.27}$$

$$(\Xi_5)^i_j \equiv \Xi_5(\lambda_i, \lambda_j)\,, \tag{5.28}$$

$$|\Xi_5|^i_j \equiv |\Xi_5(\lambda_i, \lambda_j)|\,. \tag{5.29}$$

5.1.2 Recursion relationships for chirality operators

In this subsection, the recursion relations of Eqs. (5.9)-(5.12) which hold for the chirality operator and the shift operator are proved. Re-

minding of the definition of the chirality operator,

$$\left\langle f_\alpha^s \middle| [\gamma_5 \otimes 1] \middle| f_\beta^s \right\rangle \equiv \sum_x \left[f_\alpha^s(x_A) \right]^\dagger \overline{(\gamma_5 \otimes 1)}_{AB} \, U(x_A, x_B) \, f_\beta^s(x_B) \,, \tag{5.30}$$

$$\overline{(\gamma_5 \otimes 1)}_{AB} = \frac{1}{4} \operatorname{Tr}\Big(\gamma_A^\dagger \gamma_5 \gamma_B 1 \Big) = \delta_{\,\overline{A}B} \, \eta_5(A) \,, \tag{5.31}$$

$$U(x_A, x_B) = \mathbb{P}_{\mathrm{SU}(3)} \left[\sum_{p \in \mathcal{C}} V(x_A, x_{p_1}) V(x_{p_1}, x_{p_2}) V(x_{p_2}, x_{p_3}) V(x_{p_3}, x_B) \right] . \tag{5.32}$$

First, let us prove the following theorem.

Theorem 1.

$$[\gamma_5 \otimes 1][\gamma_5 \otimes 1] = [1 \otimes 1] \,. \tag{5.33}$$

Proof. The left-hand side is expressed as

$$\begin{aligned} [\gamma_5 \otimes 1]^2_{AC} &= \sum_B \overline{(\gamma_5 \otimes 1)}_{AB} U(x_A, x_B) \, \overline{(\gamma_5 \otimes 1)}_{BC} U(x_B, x_C) \\ &= \sum_B [\overline{(\gamma_5 \otimes 1)}_{AB} \overline{(\gamma_5 \otimes 1)}_{BC}] \, [U(x_A, x_B) \, U(x_B, x_C)] \\ &= \sum_B [\delta_{\,\overline{A}B} \, \eta_5(A) \, \delta_{\,\overline{B}C} \, \eta_5(B)] [U(x_A, x_B) \, U(x_B, x_C)] \\ &= \delta_{AC} [U(x_A, x_{\bar{A}}) \, U(x_{\bar{A}}, x_A)] \,. \end{aligned} \tag{5.34}$$

In the last equality, $\eta_5(\bar{A}) = \eta_5(A)$ is used. Thanks to the SU(3) projection in Eq. (5.32), $U(x_{\bar{A}}, x_A) = [U(x_A, x_{\bar{A}})]^\dagger \in \mathrm{SU}(3)$, which

implies $U(x_A, x_{\bar{A}})U(x_{\bar{A}}, x_A) = 1$. Therefore,

$$[\gamma_5 \otimes 1]^2_{AC} = \delta_{AC} = [1 \otimes 1]_{AC} \,. \tag{5.35}$$

(Q.E.D.) □

Using theorem 1, it is straightforward to prove two recursion relationships:

$$\begin{aligned}
[\gamma_5 \otimes 1]^{2n+1} &= \left([\gamma_5 \otimes 1]^2\right)^n \cdot [\gamma_5 \otimes 1] && (5.36)\\
&= ([1 \otimes 1])^n \cdot [\gamma_5 \otimes 1] && (5.37)\\
&= [1 \otimes 1] \cdot [\gamma_5 \otimes 1] && (5.38)\\
&= [\gamma_5 \otimes 1] \,, && (5.39)
\end{aligned}$$

and

$$\begin{aligned}
[\gamma_5 \otimes 1]^{2n} &= \left([\gamma_5 \otimes 1]^2\right)^n && (5.40)\\
&= ([1 \otimes 1])^n && (5.41)\\
&= [1 \otimes 1] \,. && (5.42)
\end{aligned}$$

Finally, let us claim the following theorem.

Theorem 2.

$$\left[\frac{1+\gamma_5}{2} \otimes 1\right]\left[\frac{1+\gamma_5}{2} \otimes 1\right] = \left[\frac{1+\gamma_5}{2} \otimes 1\right] . \tag{5.43}$$

Proof.

$$\begin{aligned}\left[\frac{1+\gamma_5}{2}\otimes 1\right]^2 &= \frac{1}{4}\left([1\otimes 1]+[\gamma_5\otimes 1]\right)^2 \\ &= \frac{1}{4}\left([1\otimes 1]+2[\gamma_5\otimes 1]+[\gamma_5\otimes 1]^2\right) \\ &= \frac{1}{2}\left([1\otimes 1]+[\gamma_5\otimes 1]\right) \\ &= \left[\frac{1+\gamma_5}{2}\otimes 1\right]. \end{aligned} \tag{5.44}$$

(Q.E.D.) □

It is trivial to extend theorem 2 to any $n > 0$ and $n \in \mathbb{Z}$ by induction:

$$\left[\frac{1+\gamma_5}{2}\otimes 1\right]^n = \left[\frac{1+\gamma_5}{2}\otimes 1\right]. \tag{5.45}$$

In a similar manner, the last recursion relation is derived easily:

$$\begin{aligned}&\left[\frac{1+\gamma_5}{2}\otimes 1\right]\left[\frac{1-\gamma_5}{2}\otimes 1\right] \\ &= \frac{1}{4}\left[1\otimes 1+\gamma_5\otimes 1\right]\left[1\otimes 1-\gamma_5\otimes 1\right] \\ &= \frac{1}{4}\left[1\otimes 1-{\gamma_5}^2\otimes 1\right] \\ &= 0\,. \end{aligned} \tag{5.46}$$

5.1.3 Chirality measurement

Fig. 5.1 presents some measurement results of the chirality $\Gamma_5(\lambda_i,\lambda_i)$ in Eq. (5.2) for staggered Dirac eigenmodes. Results in Figs. 5.1(a)-

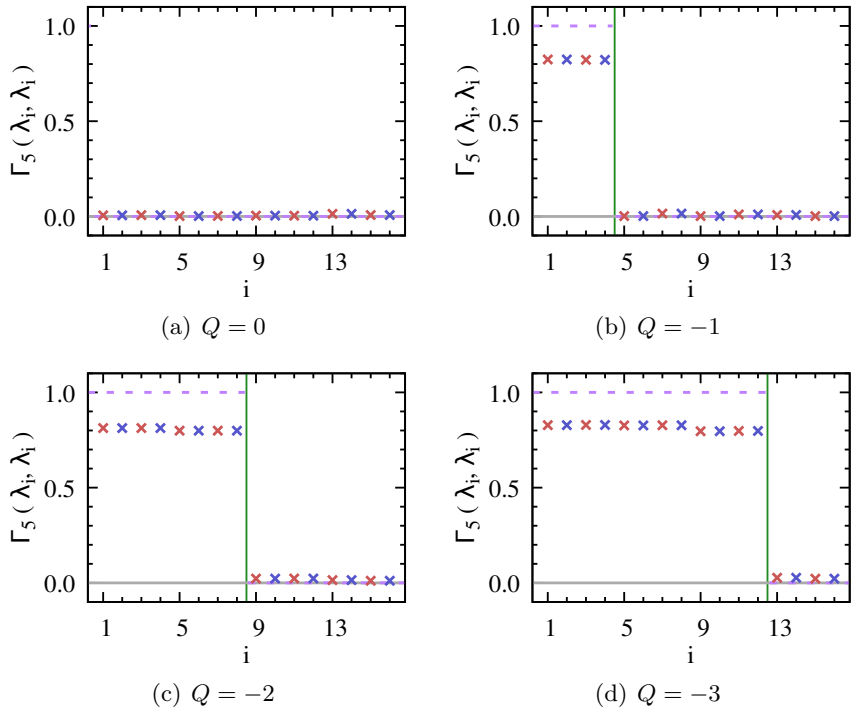

(a) $Q = 0$ (b) $Q = -1$

(c) $Q = -2$ (d) $Q = -3$

Figure 5.1: Chirality measurements when $Q = 0, -1, -2, -3$. Cross symbols represent measurement data and purple dashed lines represent theoretical expectations in the continuum QCD.

5.1(d) are measured on gauge configurations with different topological charges($Q = 0, -1, -2, -3$) so that they have different numbers of would-be zero modes [1]. In theory, we expect that zero modes have an exact chirality of $+1$ or -1, while non-zero modes have no chirality (zero). However, for staggered fermions chiral symmetry is somewhat broken, so would-be zero modes do not have an exact chirality. Instead, as Fig. 5.1 shows, they have chiralities less than 1. These magnitudes

[1] Usually, all would-be zero modes measured on a gauge configuration have chiralities of the same sign

of chirality mainly depend on improvements of Dirac operator and the performance of smearing/cooling [8, 9], but the definition of chirality operator also affects them. It is turned out that this loss of chirality is related with the renormalization factors of the chirality operator $[\gamma_5 \otimes 1]$ and $\mathrm{U(1)_A}$ symmetry transformation operator $[\gamma_5 \otimes \xi_5]$. Details on the renormalization factor are discussed in Section 7.1.

In the results shown in Fig. 5.1, would-be zero modes have chiralities around 0.8. It is somewhat smaller than the theory expectation (+1), nonetheless, it is enough to determine their true chiralities (+1) since non-zero modes have definitely negligible chiralities. Hence, one can say that there is no would-be zero modes ($n_+ = 0$, $n_- = 0$) in Fig. 5.1(a), there are four of right-handed zero modes ($n_+ = 4$, $n_- = 0$) in Fig. 5.1(b), eight of right-handed ($n_+ = 8$, $n_- = 0$) in Fig. 5.1(c), and twelve of right-handed ($n_+ = 12$, $n_- = 0$) in Fig. 5.1(d). These observations indeed correspond to the index theorem of Eq. (3.39) with taking account of SU(4) taste symmetry: $Q = \frac{1}{4}(n_- - n_+)$.

In Fig. 5.2, examples of the chirality measurement when $Q = 1$ and $Q = 2$ are presented. In these examples, would-be zero modes have chiralities around -0.8, which is somewhat deviated from the theory expectation (-1) but again enough to determine their true values (-1). Similarly with the previous examples when there are only right-handed would-be zero modes, here one can conclude that

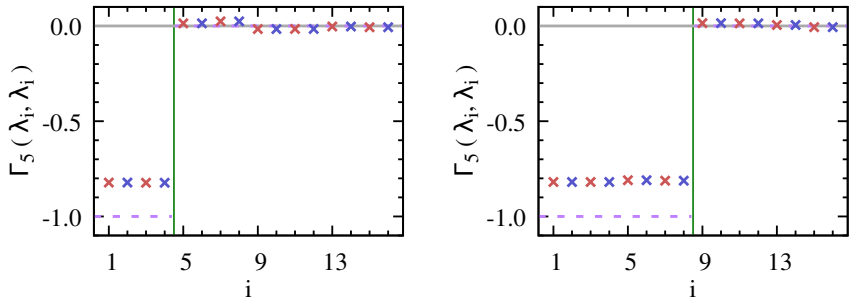

(a) $Q = 1$ (b) $Q = 2$

Figure 5.2: Chirality measurements when $Q = 1, 2$. Details are same with Fig. 5.1

there are four left-handed would-be zero modes ($n_+ = 0$, $n_- = 4$) in Fig. 5.2(a) and eight left-handed ($n_+ = 0$, $n_- = 8$) in Fig. 5.2(b). And they correspond to the index theorem.

5.2 Chiral Ward identity

5.2.1 Ward identities on eigenvalue spectrum

Combining Ward identities in Eq. (5.24) and Eq. (3.11), the following Ward identities are obtained:

$$\begin{aligned} e^{+i\theta}[\gamma_5 \otimes 1]\,|f_{-i}\rangle &= [1 \otimes \xi_5]\,|f_{+i}\rangle\ , \\ e^{-i\theta}[\gamma_5 \otimes 1]\,|f_{+i}\rangle &= [1 \otimes \xi_5]\,|f_{-i}\rangle\ , \end{aligned} \tag{5.47}$$

where $|f_{\pm i}\rangle \equiv \left|f^s_{\pm\lambda_i}\right\rangle$. These Ward identities relate parity partner eigenstates with eigenvalues $\pm\lambda_i$ through the chirality operator and

the shift operator. Now, let us consider the spectral decompositions

$$[\gamma_5 \otimes 1]\,|f_j\rangle = \sum_i (\Gamma_5)^i_j\,|f_i\rangle\ , \tag{5.48}$$

$$\begin{aligned}(\Gamma_5)^i_j &= \langle f_i|[\gamma_5 \otimes 1]|f_j\rangle \\ &= \Gamma_5(\lambda_i, \lambda_j)\,,\end{aligned} \tag{5.49}$$

and

$$[1 \otimes \xi_5]\,|f_j\rangle = \sum_i (\Xi_5)^i_j\,|f_i\rangle\ , \tag{5.50}$$

$$\begin{aligned}(\Xi_5)^i_j &= \langle f_i|[1 \otimes \xi_5]|f_j\rangle \\ &= \Xi_5(\lambda_i, \lambda_j)\,.\end{aligned} \tag{5.51}$$

$(\Gamma_5)^i_j$ and $(\Xi_5)^i_j$ are matrix elements on staggered Dirac eigenspace. Rewriting the Ward identities of Eq. (5.47) in terms of $(\Gamma_5)^i_j$ and $(\Xi_5)^i_j$ gives the following equalities:

$$\begin{aligned}& e^{-i\theta}\,\Gamma_5(\lambda_i, +\lambda_j) = \Xi_5(\lambda_i, -\lambda_j) \\ \Leftrightarrow \qquad & e^{-i\theta}(\Gamma_5)^i_{+j} = (\Xi_5)^i_{-j} \\ \Leftrightarrow \qquad & |\Gamma_5|^i_{+j} = |\Xi_5|^i_{-j}\,,\end{aligned} \tag{5.52}$$

and

$$
\begin{aligned}
& e^{+i\theta}\,\Gamma_5(\lambda_i,-\lambda_j) = \Xi_5(\lambda_i,+\lambda_j) \\
\Leftrightarrow \qquad & e^{+i\theta}(\Gamma_5)^i_{-j} = (\Xi_5)^i_{+j} \\
\Leftrightarrow \qquad & |\Gamma_5|^i_{-j} = |\Xi_5|^i_{+j}\,. \qquad (5.53)
\end{aligned}
$$

In the meantime, applying Γ_ϵ on both sides of Eq. (5.48) gives

$$
[1\otimes\xi_5]\,|f_j\rangle = \sum_\ell (\Gamma_5)^\ell_j e^{i\theta_\ell}\,|f_{-\ell}\rangle\ . \qquad (5.54)
$$

Comparing with Eq. (5.50), we get another Ward identity:

$$
|\Gamma_5|^{-i}_j = |\Xi_5|^{+i}_j \qquad (5.55)
$$

Similarly, one can show that the following Ward identities also hold:

$$
|\Gamma_5|^{-i}_{-j} = |\Xi_5|^{+i}_{-j}\,, \qquad (5.56)
$$

$$
|\Gamma_5|^{+i}_j = |\Xi_5|^{-i}_j\,. \qquad (5.57)
$$

All the results of Eqs. (5.52)-(5.57) can be summarized as

$$|\Gamma_5|^i_j = |\Xi_5|^{-i}_j = |\Xi_5|^i_{-j} = |\Gamma_5|^{-i}_{-j} \tag{5.58}$$

$$\left(\Leftrightarrow \; |\Gamma_5(\lambda_i, \lambda_j)| = |\Xi_5(-\lambda_i, \lambda_j)| = |\Xi_5(\lambda_i, -\lambda_j)| = |\Gamma_5(-\lambda_i, -\lambda_j)| \right). \tag{5.59}$$

In addition, the Hermiticity of Γ_5 and Ξ_5 insures interchanging λ_i and λ_j. This gives the final form of chiral Ward identities:

$$\begin{aligned} |\Gamma_5|^i_j &= |\Xi_5|^{-i}_j = |\Xi_5|^i_{-j} = |\Gamma_5|^{-i}_{-j} \\ &= |\Gamma_5|^j_i = |\Xi_5|^{-j}_i = |\Xi_5|^j_{-i} = |\Gamma_5|^{-j}_{-i} \end{aligned} \tag{5.60}$$

$$\begin{aligned} \Bigg(\Leftrightarrow |\Gamma_5(\lambda_i, \lambda_j)| &= |\Xi_5(-\lambda_i, \lambda_j)| = |\Xi_5(\lambda_i, -\lambda_j)| = |\Gamma_5(-\lambda_i, -\lambda_j)| \\ &= |\Gamma_5(\lambda_j, \lambda_i)| = |\Xi_5(-\lambda_j, \lambda_i)| = |\Xi_5(\lambda_j, -\lambda_i)| = |\Gamma_5(-\lambda_j, -\lambda_i)| \Bigg). \end{aligned} \tag{5.61}$$

Another simple derivation is also described in Ref. [17].

5.2.2 Ward identities: numerical results

Tables 5.1 and 5.2 present numerical demonstrations of chiral Ward identities in Eq. (5.60). The results indicate that the chiral Ward identities are valid within a numerical precision. In Table 5.1, λ_1 and λ_2 are would-be zero modes and they are parity partners of each other.

parameter	value
$\lvert\,\Gamma_5(\lambda_1,\lambda_1)\,\rvert$	0.8238257
$\lvert\,\Xi_5(\lambda_2,\lambda_1)\,\rvert$	0.8238257
$\lvert\,\Xi_5(\lambda_1,\lambda_2)\,\rvert$	0.8238257
$\lvert\,\Gamma_5(\lambda_2,\lambda_2)\,\rvert$	0.8238257

Table 5.1: Numerical results of the chiral Ward identity for diagonal matrix elements. Here, $\lambda_2 = -\lambda_1$.

parameter	value	parameter	value
$\lvert\,\Gamma_5(\lambda_{75},\lambda_{70})\,\rvert$	0.5008622	$\lvert\,\Gamma_5(\lambda_{70},\lambda_{75})\,\rvert$	0.5008622
$\lvert\,\Xi_5(\lambda_{69},\lambda_{75})\,\rvert$	0.5008622	$\lvert\,\Xi_5(\lambda_{75},\lambda_{69})\,\rvert$	0.5008622
$\lvert\,\Xi_5(\lambda_{70},\lambda_{76})\,\rvert$	0.5008622	$\lvert\,\Xi_5(\lambda_{76},\lambda_{70})\,\rvert$	0.5008622
$\lvert\,\Gamma_5(\lambda_{69},\lambda_{76})\,\rvert$	0.5008622	$\lvert\,\Gamma_5(\lambda_{76},\lambda_{69})\,\rvert$	0.5008622

Table 5.2: Numerical results of the chiral Ward identity for off-diagonal matrix elements. Here, $\lambda_{70} = -\lambda_{69}$, $\lambda_{76} = -\lambda_{75}$.

Here, $\lvert\,\Gamma_5(\lambda_1,\lambda_1)\,\rvert$ represents the (diagonal) chirality of λ_1. The accordance of four matrix elements in Table 5.1 implies that chirality of λ_1 can also be measured by other three matrix elements: $\lvert\,\Xi_5(\lambda_2,\lambda_1)\,\rvert$, $\lvert\,\Xi_5(\lambda_1,\lambda_2)\,\rvert$, $\lvert\,\Gamma_5(\lambda_2,\lambda_2)\,\rvert$. In the case of Table 5.2, λ_{75} and λ_{70} are non-zero modes in a quartet, and $\lambda_{69} = -\lambda_{70}$ and $\lambda_{76} = -\lambda_{75}$ are parity partners of them, respectively. Here, $\lvert\,\Gamma_5(\lambda_{75},\lambda_{70})\,\rvert$ represents an amount of transition of λ_{70}'s chirality to λ_{75} state — This leakage of chirality is discussed in detail in Chapter 6. The fact that eight matrix elements are identical in their magnitudes implies the four eigenstates $(\lambda_{69},\lambda_{70},\lambda_{75},\lambda_{76})$ are related with each others by the chiral Ward

identity, which is a non-trivial result. More details on numerical evidence of the chiral Ward identity are discussed in Chapter 6.

Chapter 6

Leakage of chirality

6.1 Taste symmetry of staggered fermions

6.1.1 Taste symmetry in the continuum

In this subsection, staggered quark actions in the continuum at $a = 0$ are considered. As $a \to 0$, the staggered fermion field $\chi^c(x_A)$ is mapped into the continuum fermion field $\psi^c_{\alpha;t}(x)$, where α represents a Dirac spinor index, c represents a color index, $t = 1, 2, 3, 4$ represents a taste index. For a given eigenvalue λ_j, there remain four degrees of freedom which come from the taste index. Accordingly for a given eigenvalue λ_j, there are four degenerate eigenstates $|f_{j,m}\rangle$ such that

$$D_s |f_{j,m}\rangle = i\lambda_j |f_{j,m}\rangle \ , \tag{6.1}$$

with $m = 1, 2, 3, 4$. The set of $|f_{j,m}\rangle$ is called a quartet, where j is a quartet index and m is a taste index which represents the four-fold degeneracy for the eigenvalue λ_j.

Now, let us define a general form of the shift operator which corresponds to a generator of the SU(4) taste symmetry:

$$\Xi_F = [1 \otimes \xi_F] \,, \tag{6.2}$$

$$\xi_F \in \{ \, \xi_5, \, \xi_\mu, \, \xi_{\mu 5}, \, \xi_{\mu\nu} \, \} \;\; \text{for} \; \mu \neq \nu \,, \tag{6.3}$$

where ξ_μ respects the Clifford algebra $\{\xi_\mu, \xi_\nu\} = 2\delta_{\mu\nu}$ in the Euclidean spacetime. If all the four eigenstates $\{|f_{j,m}\rangle\}$ are known for a certain eigenvalue λ_j, the trace of Ξ_F on them vanishes:

$$\begin{aligned} \mathrm{Tr}(\Xi_F) &= \sum_{m=1}^{4} (\Xi_F)^{j,m}_{j,m} \\ &= \sum_{m=1}^{4} \langle f_{j,m} | \Xi_F | f_{j,m} \rangle = 0 \,. \end{aligned} \tag{6.4}$$

This is because the SU(4) group generators are traceless in the fundamental representation.

Let us consider the following quantity W_1 in the continuum at $a = 0$:

$$W_1 \equiv \langle f_\ell | \Xi_F D_s | f_n \rangle \;, \tag{6.5}$$

where f are eigenvectors of D_s satisfying

$$D_s \left| f_n \right\rangle = i\lambda_n \left| f_n \right\rangle \ . \tag{6.6}$$

Since the SU(4) taste symmetry is exactly conserved in the continuum,

$$[\Xi_F, D_s] = 0 \, . \tag{6.7}$$

Hence, the following Ward identity holds:

$$\begin{aligned} W_1 = & \ \langle f_\ell | \Xi_F D_s | f_n \rangle = i\lambda_n \langle f_\ell | \Xi_F | f_n \rangle \\ = & \ \langle f_\ell | D_s \Xi_F | f_n \rangle = i\lambda_\ell \langle f_\ell | \Xi_F | f_n \rangle \ , \end{aligned} \tag{6.8}$$

which leads to

$$i(\lambda_\ell - \lambda_n) \cdot \langle f_\ell | \Xi_F | f_n \rangle = 0 \, . \tag{6.9}$$

Eq. (6.9) implies the following properties:

- If $\lambda_\ell \neq \lambda_n$, $(\Xi_F)^\ell_n = \langle f_\ell | \Xi_F | f_n \rangle = 0$. In other words, if eigenvalues of two eigenstates are different, there is no leakage of Ξ_F between them.

- If $\lambda_j \equiv \lambda_\ell = \lambda_n$, $(\Xi_F)^\ell_n \neq 0$ is possible. In other words, if two eigenstates are degenerate, the leakage of Ξ_F between them is allowed. Here, $|f_\ell\rangle$ and $|f_n\rangle$ are linear combinations of the quartet $\{|f_{j,m}\rangle\}$ and they are orthogonal to each other by construction

because Lanczos algorithm calculates orthogonal eigenvectors.

6.1.2 Taste symmetry breaking on eigenvalue spectrum

On the lattice at $a \neq 0$, the taste symmetry is broken by those terms of order $a^2\alpha_s^n$ with $n \geq 1$ which is explained in Ref. [22]. For instance, the eigenvalue equation of Eq. (6.1) should be rewritten as

$$D_s \left| f_{j,m} \right\rangle = i\lambda_{j,m} \left| f_{j,m} \right\rangle \ . \tag{6.10}$$

Here, $\lambda_{j,m} \neq \lambda_{j,m'}$ in general for $m \neq m'$, which reflects the taste symmetry breaking effect at $a \neq 0$. However, the difference $|\lambda_{j,m} - \lambda_{j,m'}|$ is not so large as discussed in Section 4.2. It is also expected that other continuum properties described in Subsection 6.1.1 have some small deviations on the lattice.

A good barometer to measure this effect is monitoring T_5 which is defined as

$$T_5 \equiv \frac{1}{4}\,\mathrm{Tr}(\Xi_5) = \frac{1}{4}\sum_m (\Xi_5)^{j,m}_{j,m}\,. \tag{6.11}$$

If the taste symmetry is exactly conserved, then T_5 must vanish by Eq. (6.4). Hence, a non-trivial value of T_5 indicates size of taste symmetry breaking. In Table 6.1, T_5 is measured on around 7500 numbers of quartets including both would-be zero mode quartets ($j = 0$) and non-zero mode quartets ($j > 0$). The results show that $|\,\mathrm{Re}(T_5)|$ is of the order of a sub-percent level ($\sim 10^{-3}$) per quartet, while

Table 6.1: Numerical results for T_5. The measurement is done on 292 gauge configurations with input parameters in Table 4.1. N_q represents the number of quartets used to obtain the statistical error. Here, $j = 0$ represents would-be zero mode quartets, and $j > 0$ represents non-zero mode quartets.

j	$\lvert \mathrm{Re}(T_5) \rvert$	$\lvert \mathrm{Im}(T_5) \rvert$	N_q
$j = 0$	$7.2(130) \times 10^{-4}$	$5.9(46) \times 10^{-12}$	490
$j > 0$	$6.2(120) \times 10^{-3}$	$3.3(25) \times 10^{-12}$	7034

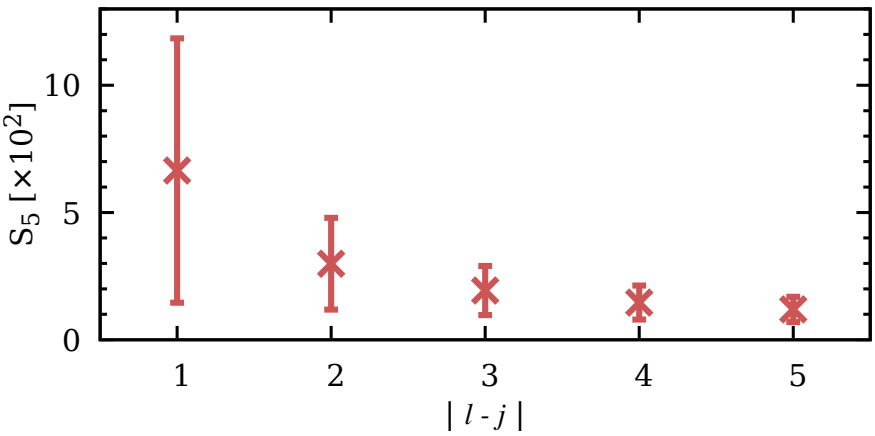

Figure 6.1: S_5 as a function of $|\ell - j|$. Numerical values are given in Table 6.2.

$|\mathrm{Im}(T_5)| = 0$ essentially. This indicates that the effect of taste symmetry breaking is very small.

Another direct barometer of the taste symmetry breaking is monitoring the leakage S_5 from one quartet (λ_ℓ) to another quartet (λ_j) when $\lambda_\ell \neq \lambda_j$:

$$S_5 \equiv \frac{1}{16} \sum_{m,m'} |\Xi_5|^{\ell,m}_{j,m'} = \frac{1}{16} \sum_{m,m'} |\left\langle f_{\ell,m} \middle| \Xi_5 \middle| f_{j,m'} \right\rangle| \,. \tag{6.12}$$

Table 6.2: Numerical results for S_5. The leakages are measured between two different quartets ($\ell \neq j$ and $\ell, j \geq 0$). N_p represents the number of (ℓ, j) pairs with $\ell \neq j$.

$\lvert\ell - j\rvert$	S_5	N_p
1	$6.6(52) \times 10^{-2}$	7185
2	$3.0(18) \times 10^{-2}$	6893
3	$1.9(10) \times 10^{-2}$	6601
4	$1.5(7) \times 10^{-2}$	6309
5	$1.2(5) \times 10^{-2}$	6017

The size of S_5 indicates directly how much the taste symmetry is broken at $a \neq 0$, because $S_5 = 0$ in the continuum at $a = 0$. In Fig. 6.1, S_5 is measured as a function of $|\ell - j|$ with ℓ, $j \geq 0$. Here, $|\ell - j| = 1$ represents a pair of nearest neighbor quartets, $|\ell - j| = 2$ represents a pair of next to the nearest neighbor quartets, and so on. The results show that the values of S_5 are as big as their statistical error. This means that this taste symmetry breaking effect gives just a random noise to the physical signal ($S_5 = 0$). For $|\ell - j| = 1$, it gives a random noise of $\approx 7\%$, and for $|\ell - j| = 2$, it gives a random noise of $\approx 3\%$. In this way, the random noise decreases as $|\ell - j|$ increases. The numerical values of S_5 in Fig. 6.1 are presented in Table 6.2.

6.2 Leakage pattern and symmetry

The $(|\Gamma_5|^i_j)^2$ represents the leakage probability of the chirality operator if $i \neq j$ (or $\lambda_i \neq \lambda_j$). $|\Gamma_5|^i_j$ is called the leakage parameter for the

Table 6.3: One to one mapping of a normal index i of the λ_i eigenstate into a quartet index j and a taste index m for the $\lambda_{j,m}$. $\lambda_i = \lambda_{j,m}$. Here, $\lambda_{2n} = -\lambda_{2n-1}$ and $\lambda_{-j,m} = -\lambda_{+j,m}$. The zero represents would-be zero modes. The non-zero represents non-zero modes. Here, we assume that $|Q| = 1$.

λ_i	$\lambda_{j,m}$	i	j	m	mode
λ_1	$\lambda_{0,1}$	1	0	1	zero
λ_2	$\lambda_{0,2}$	2	0	2	zero
λ_3	$\lambda_{0,3}$	3	0	3	zero
λ_4	$\lambda_{0,4}$	4	0	4	zero
λ_5	$\lambda_{+1,1}$	5	$+1$	1	non-zero
λ_7	$\lambda_{+1,2}$	7	$+1$	2	non-zero
λ_9	$\lambda_{+1,3}$	9	$+1$	3	non-zero
λ_{11}	$\lambda_{+1,4}$	11	$+1$	4	non-zero
λ_6	$\lambda_{-1,1}$	6	-1	1	non-zero
λ_8	$\lambda_{-1,2}$	8	-1	2	non-zero
λ_{10}	$\lambda_{-1,3}$	10	-1	3	non-zero
λ_{12}	$\lambda_{-1,4}$	12	-1	4	non-zero

chirality operator. Similarly, $|\Xi_5|^i_j$ is called the leakage parameter for the shift operator. By monitoring the leakage pattern, it is possible to distinguish zero modes from non-zero modes, which is the main subject of this section.

6.2.1 Quartet index

In this section, dual notations are used for eigenmodes; one is the normal index i for λ_i, and the other is the quartet index j with taste index m for $\lambda_{j,m}$. The normal index is convenient for the plots, ta-

bles, and leakage patterns such as $|\Gamma_5|^a_b$, while the quartet index is convenient to explain the eigenstates classified by the taste symmetry group. Examples of the one-to-one mapping from the normal index system i to the quartet index system j, m are given in Table 6.3 for the quartet index $j = 0, \pm 1$ when $|Q| = 1$.

6.2.2 Leakage pattern of chirality and shift operators

In Fig. 6.2, leakage patterns of chirality operator and shift operator for the would-be zero mode λ_1 and its parity partner $\lambda_2 = -\lambda_1$ are present. Here, $Q = -1$, it is expected to observe four-fold degenerate would-be zero modes within a single quartet (quartet index $j = 0$):

$$\lim_{a \to 0} \lambda_i = 0 \quad \text{for } i = 1, 2, 3, 4\,. \tag{6.13}$$

In the continuum limit ($a = 0$), the SU(4) taste symmetry becomes exactly conserved, thus, would-be zero modes become exact zero modes. However, at finite lattice spacing of $a \neq 0$, the gauge configuration is so rough that would-be zero modes have non-zero eigenvalues: $\lambda_2 = -\lambda_1$, $\lambda_4 = -\lambda_3$, and $\lambda_1 \neq \lambda_3$ for $\lambda_1, \lambda_3 > 0$. Therefore, the size of the eigenvalue does not guarantee a zero mode as discussed in Section 4.2.

Fig. 6.2(a) shows the leakage pattern of $|\Gamma_5|^i_1 = |\Gamma_5(\lambda_i, \lambda_1)| = |\langle f_i|\Gamma_5|f_1\rangle|$. There is, in practice, no leakage to other eigenstates ($i \neq 1$). The only non-zero component is the chirality $|\Gamma_5|^1_1 = |\Gamma_5(\lambda_1, \lambda_1)|$

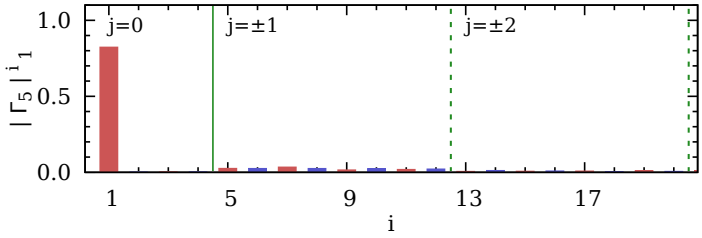

(a) $|\Gamma_5|^i_1 = |\Gamma_5(\lambda_i, \lambda_1)|$

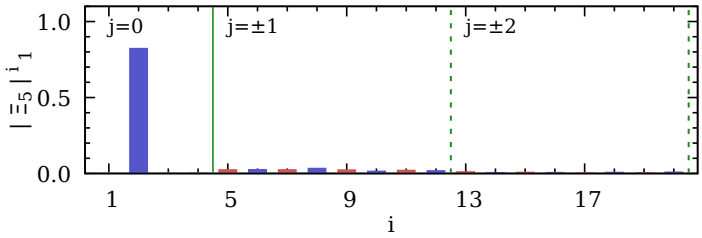

(b) $|\Xi_5|^i_1 = |\Xi_5(\lambda_i, \lambda_1)|$

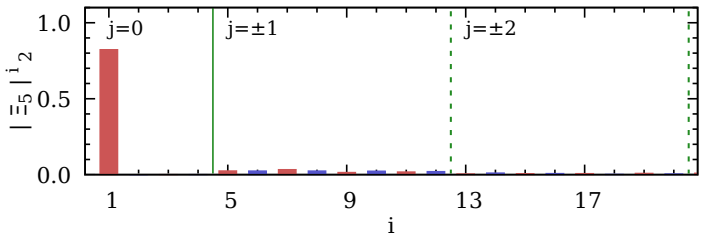

(c) $|\Xi_5|^i_2 = |\Xi_5(\lambda_i, \lambda_2 = -\lambda_1)|$

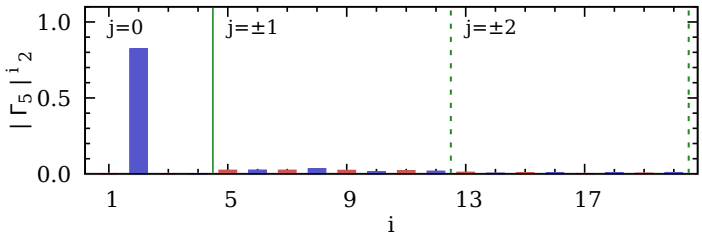

(d) $|\Gamma_5|^i_2 = |\Gamma_5(\lambda_i, \lambda_2 = -\lambda_1)|$

Figure 6.2: Leakage pattern for would-be zero modes at $Q = -1$. Here, the red bar represents leakage to $\lambda_{i=2n-1} > 0$ with odd number i, and the blue bar represents leakage to its parity partner $\lambda_{i=2n} = -\lambda_{2n-1}$ with even number i .

Table 6.4: Numerical values for leakage patterns from the λ_1 eigenstate to the λ_i eigenstate in Fig. 6.2. Here, j represents a quartet index for the λ_i eigenstate.

j	leakage	value	Ward id.
0	$\|\Gamma_5\|_1^1$	0.82382566818582	$= \|\Xi_5\|_1^2$
0	$\|\Xi_5\|_1^2$	0.82382566818581	$= \|\Xi_5\|_2^1$
0	$\|\Xi_5\|_2^1$	0.82382566818580	$= \|\Gamma_5\|_2^2$
0	$\|\Gamma_5\|_2^2$	0.82382566818579	$= \|\Gamma_5\|_1^1$
0	$\|\Gamma_5\|_1^2$	6.67×10^{-4}	
0	$\|\Gamma_5\|_1^3$	1.34×10^{-3}	
0	$\|\Gamma_5\|_1^4$	1.79×10^{-3}	
$+1$	$\|\Gamma_5\|_1^5$	2.56×10^{-2}	
-1	$\|\Gamma_5\|_1^6$	2.54×10^{-2}	
$+2$	$\|\Gamma_5\|_1^{13}$	5.77×10^{-3}	
-2	$\|\Gamma_5\|_1^{14}$	1.18×10^{-2}	

and the rest is practically zero. In Fig. 6.2(b), 6.2(c), and 6.2(d), the Ward identity of Eq. (5.60) is well respected: $|\Gamma_5|_1^1 = |\Xi_5|_1^2 = |\Xi_5|_2^1 = |\Gamma_5|_2^2$. Refer to Table 6.4 for numerical details. The table also shows that a typical size of the leakage between different would-be zero modes in $j = 0$ quartet is of order 10^{-3} (*e.g.* $|\Gamma_5|_1^3$), which is not visible in the figures. On the contrary, leakages into other quartets ($j = \pm 1, \pm 2$) are small but visible in the figures. The sizes of them are of order $10^{-2} \sim 10^{-3}$ (*e.g.* $|\Gamma_5|_1^5$).

Now let us switch to non-zero modes in the $j = +1$ quartet. Fig. 6.3 shows the leakage patterns for the non-zero modes of λ_5 and its parity

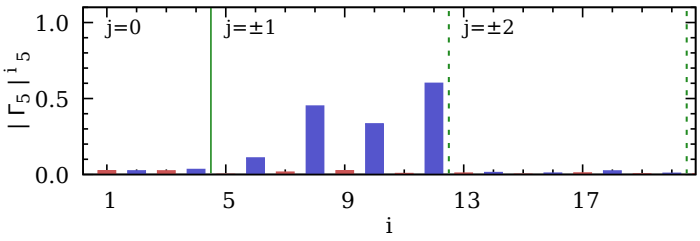

(a) $|\Gamma_5|^i_5 = |\Gamma_5(\lambda_i, \lambda_5)|$

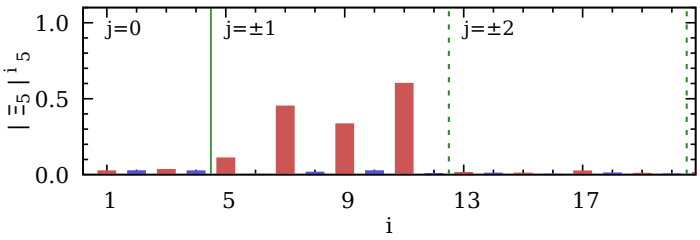

(b) $|\Xi_5|^i_5 = |\Xi_5(\lambda_i, \lambda_5)|$

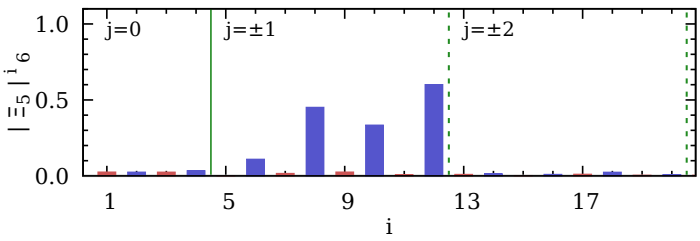

(c) $|\Xi_5|^i_6 = |\Xi_5(\lambda_i, \lambda_6 = -\lambda_5)|$

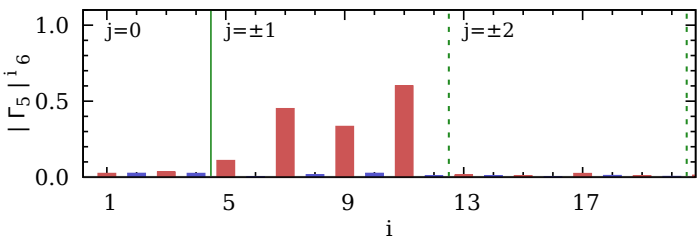

(d) $|\Xi_5|^i_6 = |\Gamma_5(\lambda_i, \lambda_6 = -\lambda_5)|$

Figure 6.3: Leakage pattern for non-zero modes at $Q = -1$.

partner $\lambda_6 = -\lambda_5$. Even in the continuum limit ($a = 0$), $\lambda_5 \neq 0$ and so it is a non-zero mode. Thanks to the approximate SU(4) taste symmetry and the exact $\mathrm{U(1)_A}$ axial symmetry, there is an eight-fold degeneracy in the family of eight eigenstates composed of the $j = +1$ quartet to which λ_5 belongs and $j = -1$ quartet (parity partners). These eight-fold degenerate modes are grouped in the name of the $j = \pm 1$ quartets in Fig. 6.3, which corresponds to a set of $\{\lambda_i\}$ with $5 \leq i \leq 12$.

Let us scrutinize the leakage pattern of the non-zero mode $\lambda_5 = \lambda_{j=+1,m=1}$. In Fig. 6.3(a), first, note that there is practically no leakage in the Γ_5 chirality measurement from λ_5 state into λ_{2n-1} state with $n > 0$ and $n \in \mathbb{Z}$. In short, $|\Gamma_5|_5^{2n-1} = |\Gamma_5(\lambda_{2n-1}, \lambda_5)| \cong 0$. This implies that the measurement of the chirality operator on the non-zero mode with $\lambda > 0$ causes its leakage into only the parity partner modes with $\lambda < 0$. In Fig. 6.3(a), second, note that the non-trivial leakage goes to those eigenstates in the $j = -1$ quartet such as $\{\lambda_6, \lambda_8, \lambda_{10}, \lambda_{12}\} = \{\lambda_{j,m} |\ j = -1,\ m = 1, 2, 3, 4\}$. In addition, the Ward identity of Eqs. (5.60) is well respected within the numerical precision in Fig. 6.3(a), 6.3(b), 6.3(c), and 6.3(d). Table 6.5 presents numerical values of $|\Gamma_5|_5^i$ in Fig. 6.3(a).

Let us examine the $\Gamma_5 = [\gamma_5 \otimes 1]$ leakage pattern for the $j = +1$ quartet of the non-zero modes $\{\lambda_5, \lambda_7, \lambda_9, \lambda_{11}\}$. In Fig. 6.4, the chirality measurement vanishes: $(\Gamma_5)_i^i = \Gamma_5(\lambda_i, \lambda_i) = 0$ for λ_i in the $j = +1$

Table 6.5: Numerical values for data in Fig. 6.3.

j	leakage	value	Ward identities
-1	$\|\Gamma_5\|^6_5$	0.110	$= \|\Xi_5\|^5_5 = \|\Xi_5\|^6_6 = \|\Gamma_5\|^5_6$
-1	$\|\Gamma_5\|^8_5$	0.452	$= \|\Xi_5\|^7_5 = \|\Xi_5\|^8_6 = \|\Gamma_5\|^7_6$ $= \|\Gamma_5\|^5_8 = \|\Xi_5\|^5_7 = \|\Xi_5\|^6_8 = \|\Gamma_5\|^6_7$
-1	$\|\Gamma_5\|^{10}_5$	0.334	$= \|\Xi_5\|^9_5 = \|\Xi_5\|^{10}_6 = \|\Gamma_5\|^9_6$ $= \|\Gamma_5\|^5_{10} = \|\Xi_5\|^5_9 = \|\Xi_5\|^6_{10} = \|\Gamma_5\|^6_9$
-1	$\|\Gamma_5\|^{12}_5$	0.601	$= \|\Xi_5\|^{11}_5 = \|\Xi_5\|^{12}_6 = \|\Gamma_5\|^{11}_6$ $= \|\Gamma_5\|^5_{12} = \|\Xi_5\|^5_{11} = \|\Xi_5\|^6_{12} = \|\Gamma_5\|^6_{11}$
$+1$	$\|\Gamma_5\|^5_5$	2.05×10^{-3}	$= \|\Xi_5\|^6_5 = \|\Xi_5\|^5_6 = \|\Gamma_5\|^6_6$
$+1$	$\|\Gamma_5\|^7_5$	16.7×10^{-3}	$= \|\Xi_5\|^8_5 = \|\Xi_5\|^7_6 = \|\Gamma_5\|^8_6$ $= \|\Gamma_5\|^5_7 = \|\Xi_5\|^5_8 = \|\Xi_5\|^6_7 = \|\Gamma_5\|^6_8$
$+1$	$\|\Gamma_5\|^9_5$	25.6×10^{-3}	$= \|\Xi_5\|^{10}_5 = \|\Xi_5\|^9_6 = \|\Gamma_5\|^{10}_6$ $= \|\Gamma_5\|^5_9 = \|\Xi_5\|^5_{10} = \|\Xi_5\|^6_9 = \|\Gamma_5\|^6_{10}$
$+1$	$\|\Gamma_5\|^{11}_5$	7.32×10^{-3}	$= \|\Xi_5\|^{12}_5 = \|\Xi_5\|^{11}_6 = \|\Gamma_5\|^{12}_6$ $= \|\Gamma_5\|^5_{11} = \|\Xi_5\|^5_{12} = \|\Xi_5\|^6_{11} = \|\Gamma_5\|^6_{12}$
0	$\|\Gamma_5\|^3_5$	2.52×10^{-2}	
0	$\|\Gamma_5\|^4_5$	3.43×10^{-2}	
$+2$	$\|\Gamma_5\|^{13}_5$	1.02×10^{-2}	
-2	$\|\Gamma_5\|^{14}_5$	1.38×10^{-2}	

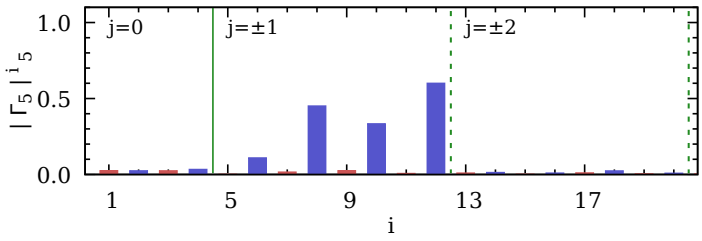

(a) $|\Gamma_5|^i_5 = |\Gamma_5(\lambda_i, \lambda_5)|$

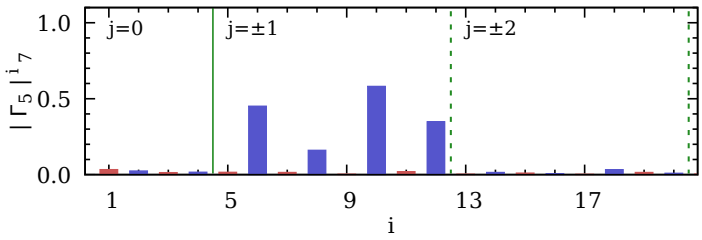

(b) $|\Gamma_5|^i_7 = |\Gamma_5(\lambda_i, \lambda_7)|$

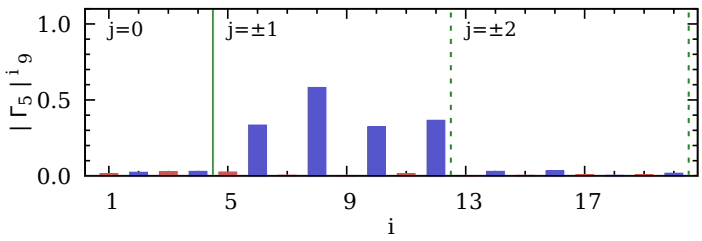

(c) $|\Gamma_5|^i_9 = |\Gamma_5(\lambda_i, \lambda_9)|$

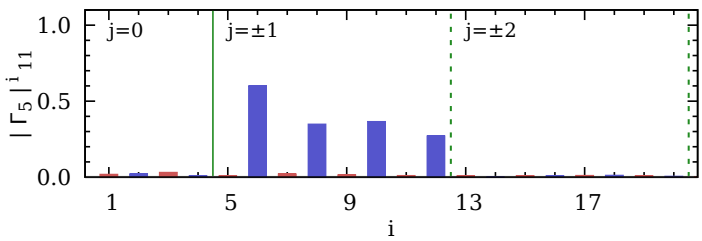

(d) $|\Gamma_5|^i_{11} = |\Gamma_5(\lambda_i, \lambda_{11})|$

Figure 6.4: $[\gamma_5 \otimes 1]$ leakage pattern for non-zero modes at $Q = -1$.

Table 6.6: $|\Gamma_5|^{-1,m}_{+1,m'}$ values in Fig. 6.4.

λ_i \ λ_j	λ_5	λ_7	λ_9	λ_{11}
λ_6	0.110	0.452	0.334	0.601
λ_8	0.452	0.161	0.582	0.349
λ_{10}	0.334	0.582	0.323	0.366
λ_{12}	0.601	0.349	0.366	0.271

quartet of the non-zero modes. Instead, the Γ_5 leakage for $\lambda_{+1,m} > 0$ of the $j = +1$ quartet goes to the parity partners of $\lambda_{-1,m'} < 0$ of the $j = -1$ quartet, and the leakage to other quartets such as $j = \pm 2$ is negligibly smaller than the leakage to the $j = -1$ quartet. The numerical values of $|\Gamma_5|^{-1,m}_{+1,m'}$ are summarized in Table 6.6.

Let us examine the $\Xi_5 = [1 \otimes \xi_5]$ leakage pattern for the $j = +1$ quartet of the non-zero modes: $\{\lambda_5, \lambda_7, \lambda_9, \lambda_{11}\}$. In Fig. 6.5, one can conclude that the Ξ_5 leakage from the $j = +1$ quartet to the $j = -1$ quartet (parity partners) vanishes in practice. Since the leakage pattern of Ξ_5 is related to the leakage pattern of Γ_5 by the Ward identity

$$|\Xi_5|^{j,m}_{j',m'} = |\Gamma_5|^{-j,m}_{j',m'}\,, \tag{6.14}$$

Fig. 6.5 is just a mirror image of Fig. 6.4 by the conserved $\mathrm{U(1)_A}$ symmetry. As in the case of Γ_5, the Ξ_5 leakage from the $j = +1$ quartet to other quartets such as $j = \pm 2$ quartets is negligibly smaller

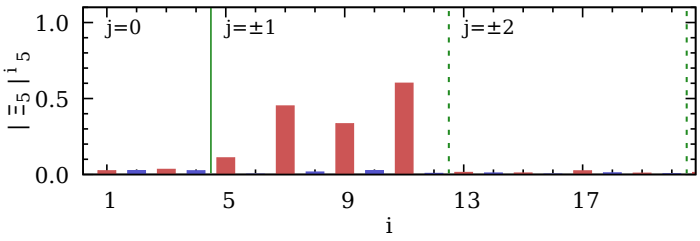

(a) $|\Xi_5|^i_5 = |\Xi_5(\lambda_i, \lambda_5)|$

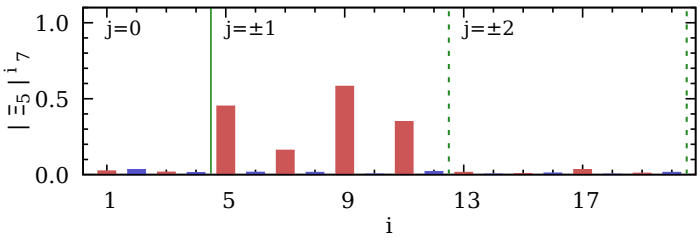

(b) $|\Xi_5|^i_7 = |\Xi_5(\lambda_i, \lambda_7)|$

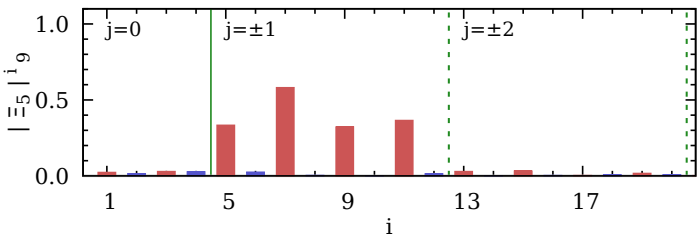

(c) $|\Xi_5|^i_9 = |\Xi_5(\lambda_i, \lambda_9)|$

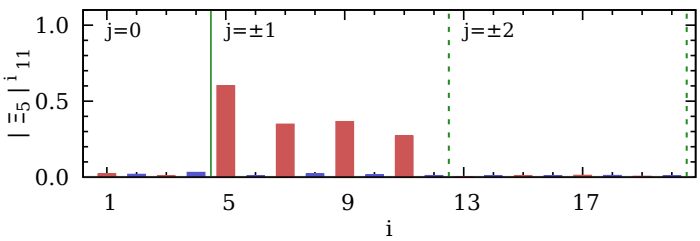

(d) $|\Xi_5|^i_{11} = |\Xi_5(\lambda_i, \lambda_{11})|$

Figure 6.5: $[1 \otimes \xi_5]$ leakage pattern for non-zero modes at $Q = -1$.

than its leakage to itself (the $j = +1$ quartet).

Let us summarize the leakage pattern for would-be zero modes and that for non-zero modes. For would-be zero modes,

1. In the chirality $\Gamma_5 = [\gamma_5 \otimes 1]$ measurement, an would-be zero mode has practically no leakage to other eigenstates.

2. In the shift $\Xi_5 = [1 \otimes \xi_5]$ measurement, an would-be zero mode with eigenvalue λ has a full (100%) leakage into its parity partner mode with eigenvalue $-\lambda$, and no leakage into any other eigenmodes.

For non-zero modes,

1. In the chirality $\Gamma_5 = [\gamma_5 \otimes 1]$ measurement, a non-zero mode with eigenvalue $\lambda_{j,m}$ has no leakage to its own quartet, but has leakage only to the parity partner quartet of $\{\lambda_{-j,m'} | m' = 1, 2, 3, 4\}$. It has no leakage to any eigenmode which belongs to other quartets such as $\ell \neq \pm j$ quartets.

2. In the shift $\Xi_5 = [1 \otimes \xi_5]$ measurement, a non-zero mode with eigenvalue $\lambda_{j,m}$ has no leakage to its parity partner quartet at all. On the contrary, it has leakage only to the eigenstates in its own quartet $\{\lambda_{j,m'} | m' = 1, 2, 3, 4\}$. This comes directly from the Ward identity. The Ξ_5 leakage pattern is a mirror image reflecting Γ_5 by the mirror of Ward identity. It has no leakage

to any eigenmode which belongs to other quartet such as $\ell \neq \pm j$ quartets.

It is also good to remember that thanks to the conserved $\mathrm{U(1)_A}$ symmetry the leakage pattern of $|\Gamma_5|^{-j,m}_{\ell,m'}$ is identical to that of $|\Xi_5|^{+j,m}_{\ell,m'}$ by the Ward identity. Subsection 6.2.3 provides more examples to demonstrate that our claim on the leakage pattern for zero modes holds valid in general. And Subsection 6.2.4 provides more examples to demonstrate that our claim on the leakage pattern for non-zero modes holds valid in general. Numerical studies on hundreds of gauge configurations were performed in order to check the above leakage pattern, and it turned out that the leakage pattern is valid for all of them except for some gauge configurations with unstable topological charge [1]

6.2.3 Examples of the leakage pattern for zero modes

Let us begin with the case of $Q = -2$. Fig. 6.6 presents leakage patterns of the chirality operator for the first set of the would-be zero modes at $Q = -2$. Fig. 6.7 presents leakage patterns of the shift operator for the first set of the would-be zero modes at $Q = -2$. Comparing Fig. 6.6 with Fig. 6.7 ensures that the chiral Ward identity of Eq. (5.60) is well respected.

Similarly, Fig. 6.8 presents leakage patterns of the chirality oper-

[1] 8 gauge configurations with unstable topological charge were found among the 300 gauge configurations used in this work.

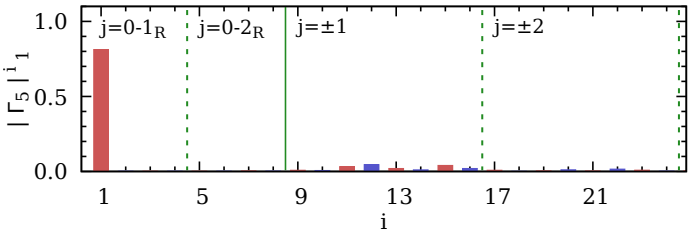

(a) $|\Gamma_5|_1^i = |\Gamma_5(\lambda_i, \lambda_1)|$

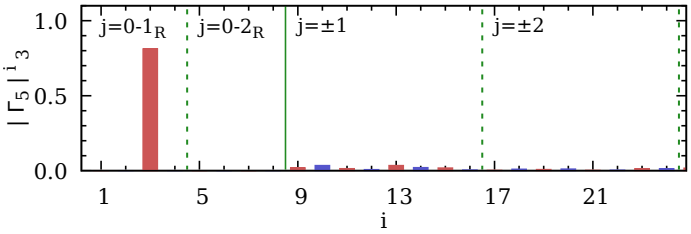

(b) $|\Gamma_5|_3^i = |\Gamma_5(\lambda_i, \lambda_3)|$

Figure 6.6: $[\gamma_5 \otimes 1]$ leakage pattern for the first quartet of would-be zero modes at $Q = -2$.

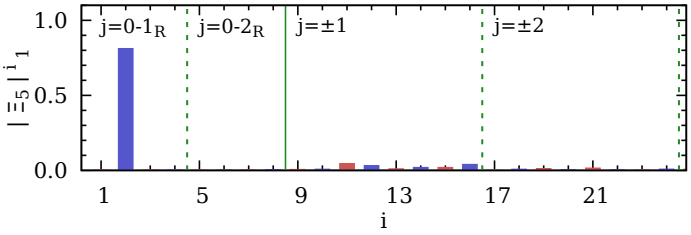

(a) $|\Xi_5|_1^i = |\Xi_5(\lambda_i, \lambda_1)|$

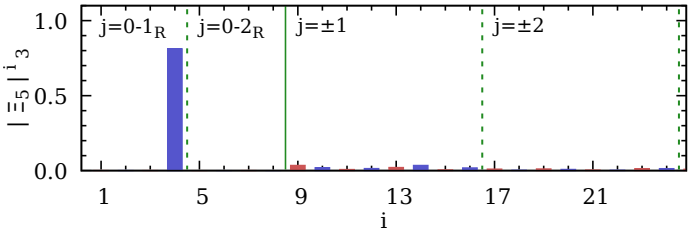

(b) $|\Xi_5|_3^i = |\Xi_5(\lambda_i, \lambda_3)|$

Figure 6.7: $[1 \otimes \xi_5]$ leakage pattern for the first quartet of would-be zero modes at $Q = -2$.

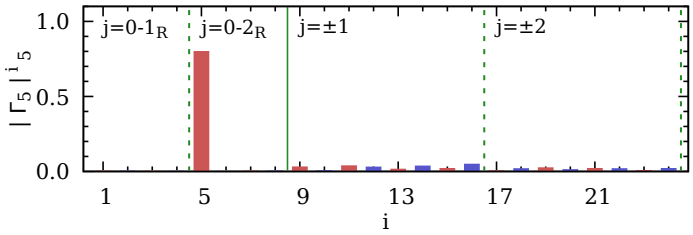

(a) $|\Gamma_5|^i_5 = |\Gamma_5(\lambda_i, \lambda_5)|$

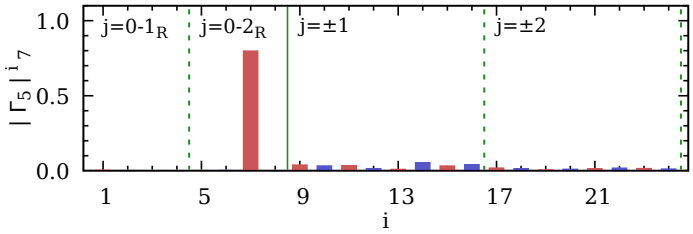

(b) $|\Gamma_5|^i_7 = |\Gamma_5(\lambda_i, \lambda_7)|$

Figure 6.8: $[\gamma_5 \otimes 1]$ leakage pattern for the second quartet of would-be zero modes at $Q = -2$.

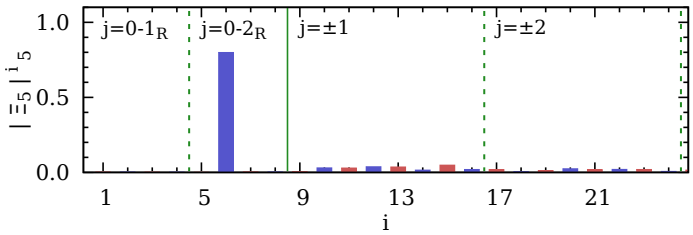

(a) $|\Xi_5|^i_5 = |\Xi_5(\lambda_i, \lambda_5)|$

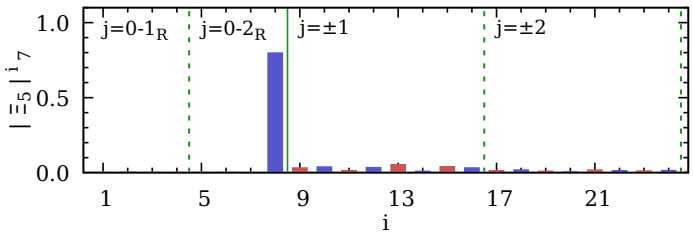

(b) $|\Xi_5|^i_7 = |\Xi_5(\lambda_i, \lambda_7)|$

Figure 6.9: $[1 \otimes \xi_5]$ leakage pattern for the second quartet of would-be zero modes at $Q = -2$.

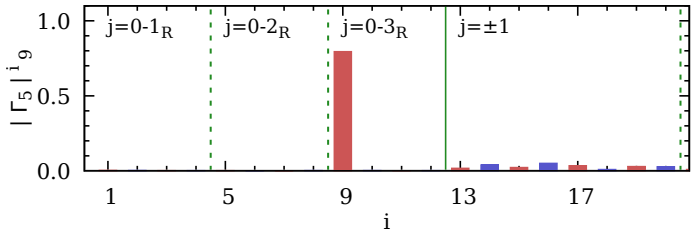

(a) $|\Gamma_5|^i_9 = |\Gamma_5(\lambda_i, \lambda_9)|$

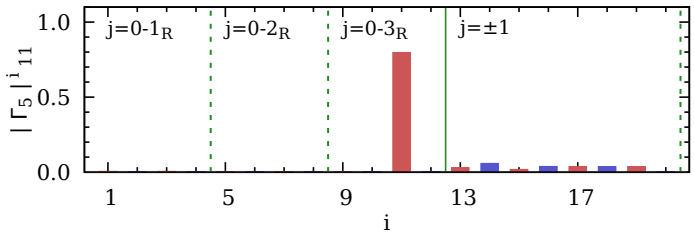

(b) $|\Gamma_5|^i_{11} = |\Gamma_5(\lambda_i, \lambda_{11})|$

Figure 6.10: $[\gamma_5 \otimes 1]$ leakage pattern for the third quartet of would-be zero modes at $Q = -3$.

ator for the second set of the would-be zero modes at $Q = -2$. And Fig. 6.9 presents the leakage patterns of the shift operator for the second set of the would-be zero modes at $Q = -2$. Comparing Fig. 6.8 with Fig. 6.9 ensures that the chiral Ward identity of Eq. (5.60) is well preserved.

Now, let us see examples with $Q = -3$. The leakage patterns for the first and second sets of would-be zero modes are similar to those at $Q = -2$. In Fig. 6.10, leakage patterns of the chirality operator are shown for the third set of the would-be zero modes at $Q = -3$. In Fig. 6.11, leakage patterns of the shift operator are shown for the third set of the would-be zero modes at $Q = -3$. As in other cases,

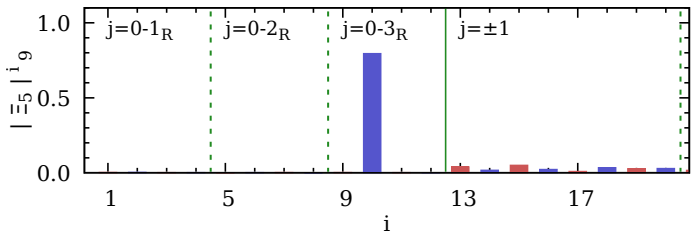

(a) $|\Xi_5|^i_9 = |\Xi_5(\lambda_i, \lambda_9)|$

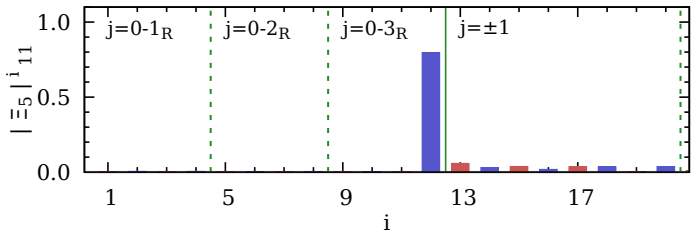

(b) $|\Xi_5|^i_{11} = |\Xi_5(\lambda_i, \lambda_{11})|$

Figure 6.11: $[1 \otimes \xi_5]$ leakage pattern for the third quartet of would-be zero modes at $Q = -3$.

by comparing Fig. 6.10 with Fig. 6.11, one finds that the chiral Ward identity of Eq. (5.60) is well preserved.

6.2.4 Examples of the leakage pattern for non-zero modes

Let us begin with an example with $Q = 0$. Since the gauge configuration with $Q = 0$ usually has no zero mode ($n_- = n_+ = 0$), it is relatively easy to study non-zero modes. Fig. 6.12 presents leakage patterns of the chirality operator $\Gamma_5 = [\gamma_5 \otimes 1]$ for non-zero modes $\{\lambda_1, \lambda_3, \lambda_5, \lambda_7\} = \{\lambda_{j,m} |\ j = +1,\ m = 1, 2, 3, 4\}$ in the $j = +1$ quartet when $Q = 0$. The results show that the Γ_5 leakages for non-zero modes $\lambda_{+1,m}$ mostly go into their parity partners of $\{\lambda_2, \lambda_4, \lambda_6, \lambda_8\} =$

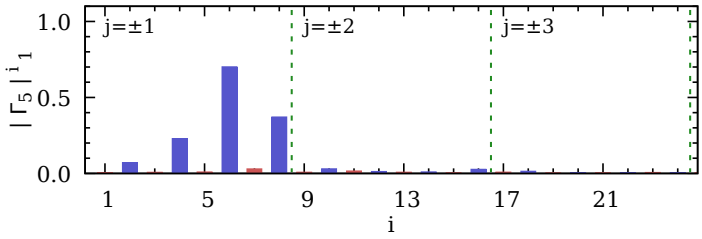

(a) $|\Gamma_5|^i_1 = |\Gamma_5(\lambda_i, \lambda_1)|$

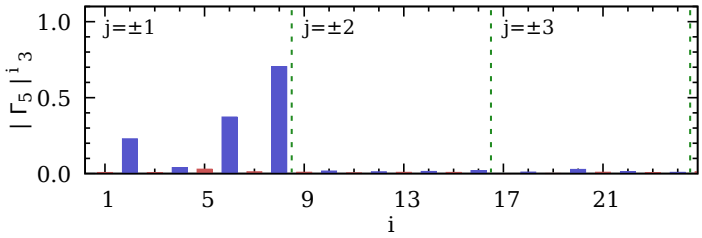

(b) $|\Gamma_5|^i_3 = |\Gamma_5(\lambda_i, \lambda_3)|$

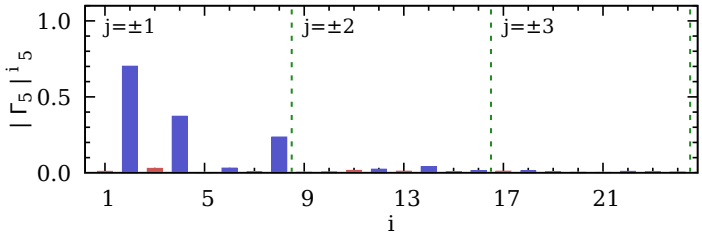

(c) $|\Gamma_5|^i_5 = |\Gamma_5(\lambda_i, \lambda_5)|$

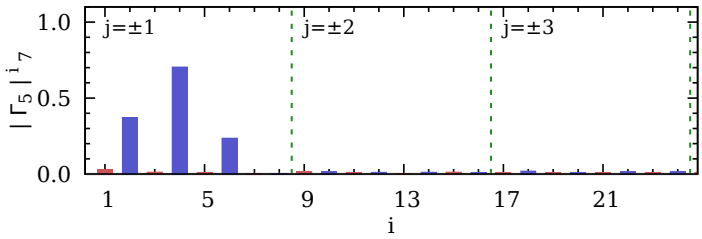

(d) $|\Gamma_5|^i_7 = |\Gamma_5(\lambda_i, \lambda_7)|$

Figure 6.12: $[\gamma_5 \otimes 1]$ leakage pattern for the first quartet of non-zero modes at $Q = 0$.

$\{\lambda_{j,m}|\ j=-1,\ m=1,2,3,4\}$ in the $j=-1$ quartet. Meanwhile, the leakages to other quartets such as $j=\pm 2,\pm 3$ are negligibly smaller than those to $j=-1$ quartet elements. This observation is consistent with that for $Q=-1$ in Fig. 6.4.

Fig. 6.13 presents leakage patterns of the shift operator $\Xi_5=[1\otimes\xi_5]$ for the non-zero modes $\{\lambda_1,\lambda_3,\lambda_5,\lambda_7\}$ of $\lambda_{+1,m}$ in the $j=+1$ quartet when $Q=0$. For the Ξ_5 operator, we find a great part of leakages from non-zero modes $\lambda_{+1,m}$ within their quartet members of $j=+1$. Meanwhile, there are only negligible amounts of leakages to its parity partner quartet elements of $j=-1$ and other quartets such as $j=\pm 2,\pm 3$. This observation corresponds to the case of $Q=-1$ in Fig. 6.5. In addition, the leakages of Γ_5 in Fig. 6.12 and those of Ξ_5 in Fig. 6.13 are related to each other by the Ward identity of Eq. (6.14).

In Figs. 6.14 and 6.15, leakage patterns of Γ_5 and Ξ_5 operators are presented, respectively, for non-zero modes $\{\lambda_9,\lambda_{11},\lambda_{13},\lambda_{15}\}=\{\lambda_{j,m}|\ j=+2,\ m=1,2,3,4\}$ in the $j=+2$ quartet when $Q=0$. Similar to the above cases for $j=+1$, Γ_5 leakages for non-zero modes of $j=+2$ mostly go to their parity partner quartet elements of $j=-2$: $\{\lambda_{10},\lambda_{12},\lambda_{14},\lambda_{16}\}=\{\lambda_{j,m}|\ j=-2,\ m=1,2,3,4\}$, and Ξ_5 leakages for them mostly go to within their quartet members of $j=+2$: $\{\lambda_9,\lambda_{11},\lambda_{13},\lambda_{15}\}$. There are only negligible amount of leakages to other quartets for both operators.

Now let us examine the leakage patterns when would-be zero

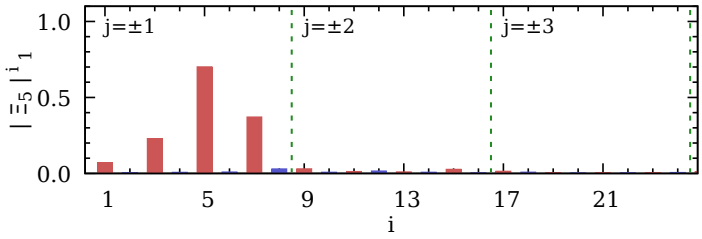

(a) $|\Xi_5|^i_1 = |\Xi_5(\lambda_i, \lambda_1)|$

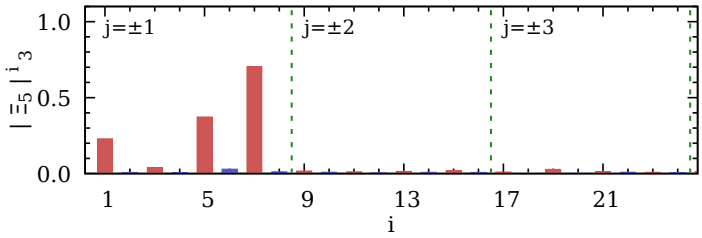

(b) $|\Xi_5|^i_3 = |\Xi_5(\lambda_i, \lambda_3)|$

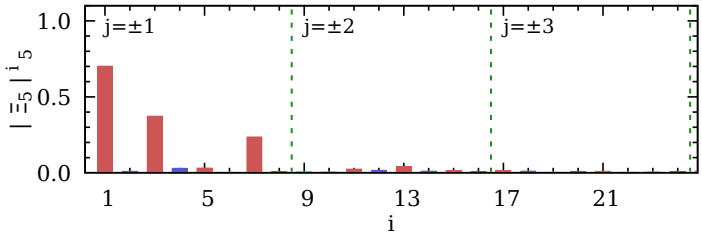

(c) $|\Xi_5|^i_5 = |\Xi_5(\lambda_i, \lambda_5)|$

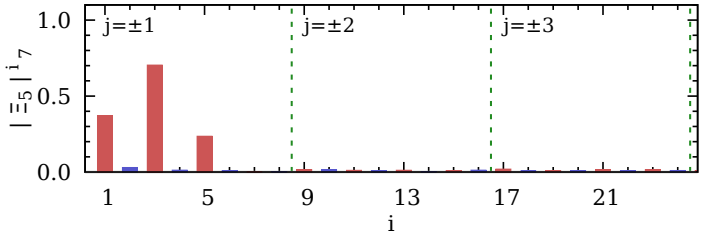

(d) $|\Xi_5|^i_7 = |\Xi_5(\lambda_i, \lambda_7)|$

Figure 6.13: $[1 \otimes \xi_5]$ leakage pattern for the first quartet of non-zero modes at $Q = 0$.

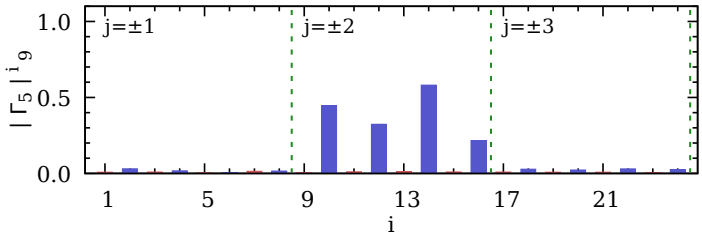

(a) $|\Gamma_5|^i_9 = |\Gamma_5(\lambda_i, \lambda_9)|$

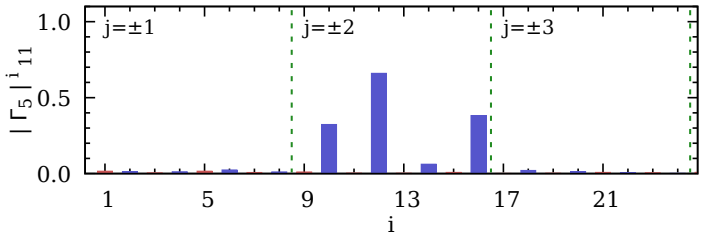

(b) $|\Gamma_5|^i_{11} = |\Gamma_5(\lambda_i, \lambda_{11})|$

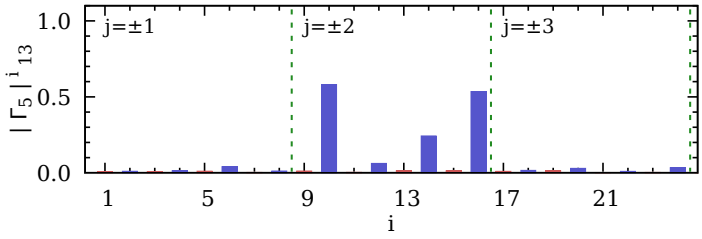

(c) $|\Gamma_5|^i_{13} = |\Gamma_5(\lambda_i, \lambda_{13})|$

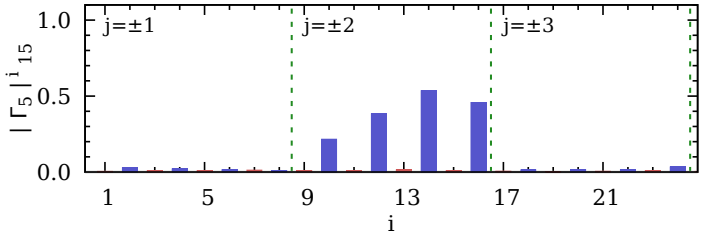

(d) $|\Gamma_5|^i_{15} = |\Gamma_5(\lambda_i, \lambda_{15})|$

Figure 6.14: $[\gamma_5 \otimes 1]$ leakage pattern for the second quartet of non-zero modes at $Q = 0$.

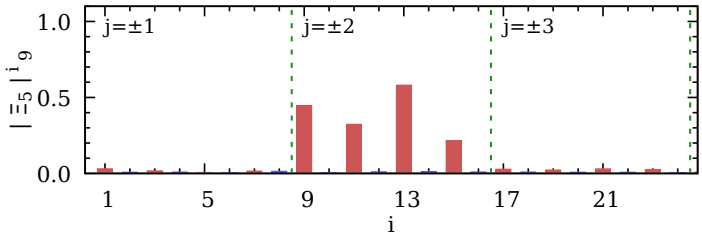

(a) $|\Xi_5|^i_9 = |\Xi_5(\lambda_i, \lambda_9)|$

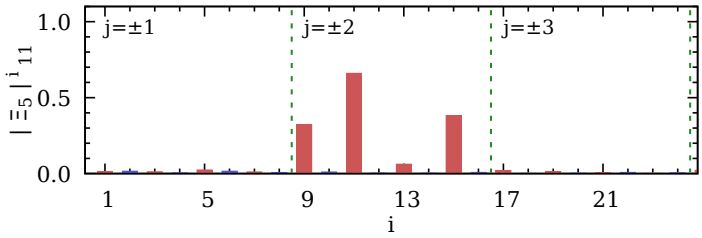

(b) $|\Xi_5|^i_{11} = |\Xi_5(\lambda_i, \lambda_{11})|$

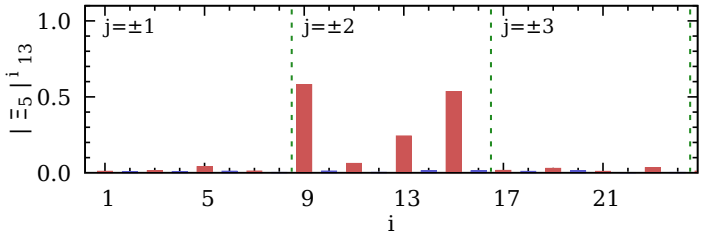

(c) $|\Xi_5|^i_{13} = |\Xi_5(\lambda_i, \lambda_{13})|$

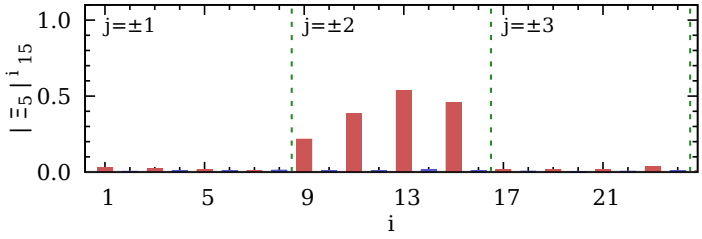

(d) $|\Xi_5|^i_{15} = |\Xi_5(\lambda_i, \lambda_{15})|$

Figure 6.15: $[1 \otimes \xi_5]$ leakage pattern for the second quartet of non-zero modes at $Q = 0$.

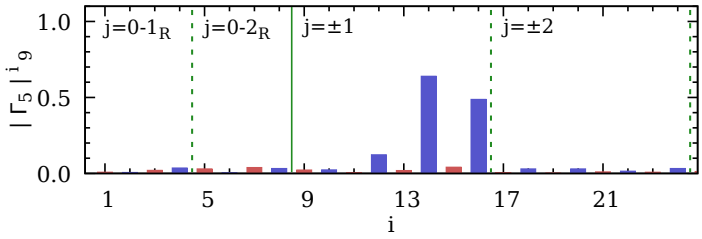

(a) $|\Gamma_5|^i_9 = |\Gamma_5(\lambda_i, \lambda_9)|$

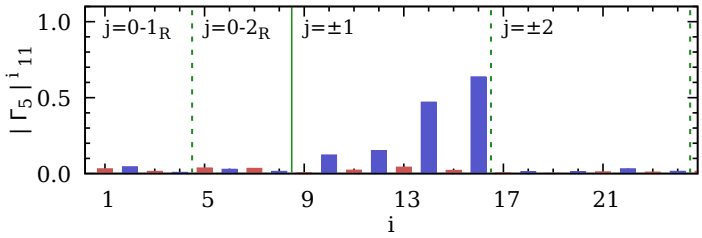

(b) $|\Gamma_5|^i_{11} = |\Gamma_5(\lambda_i, \lambda_{11})|$

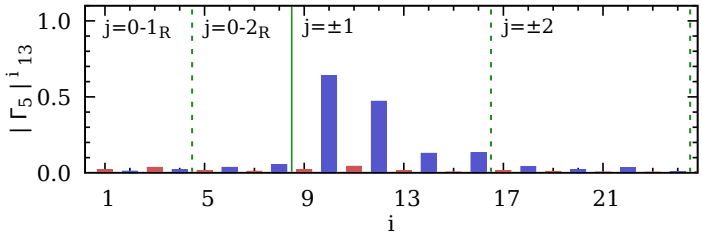

(c) $|\Gamma_5|^i_{13} = |\Gamma_5(\lambda_i, \lambda_{13})|$

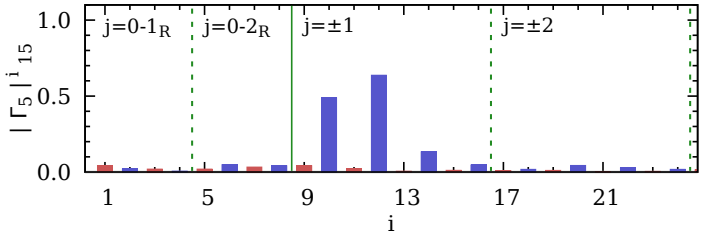

(d) $|\Gamma_5|^i_{15} = |\Gamma_5(\lambda_i, \lambda_{15})|$

Figure 6.16: $[\gamma_5 \otimes 1]$ leakage pattern for the first quartet of non-zero modes at $Q = -2$.

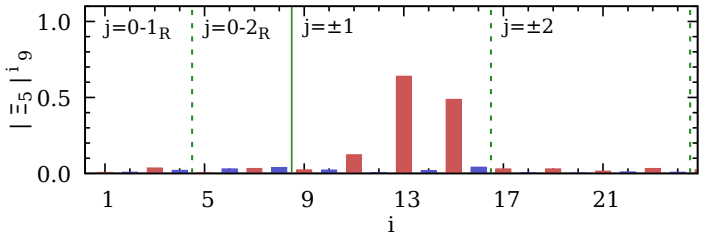

(a) $|\Xi_5|^i_9 = |\Xi_5(\lambda_i, \lambda_9)|$

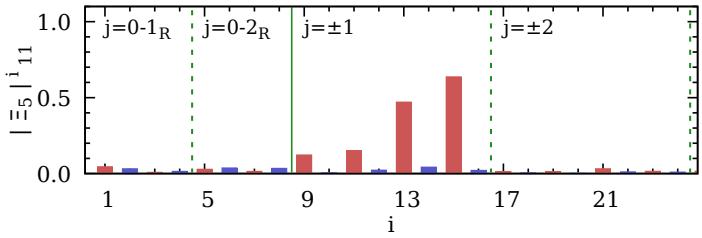

(b) $|\Xi_5|^i_{11} = |\Xi_5(\lambda_i, \lambda_{11})|$

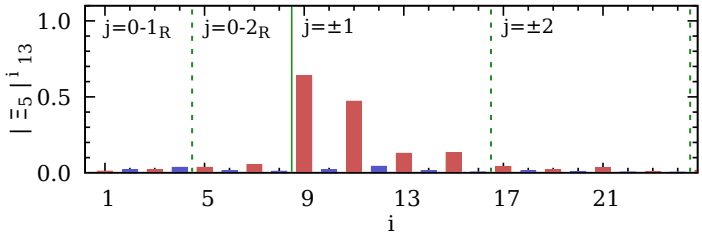

(c) $|\Xi_5|^i_{13} = |\Xi_5(\lambda_i, \lambda_{13})|$

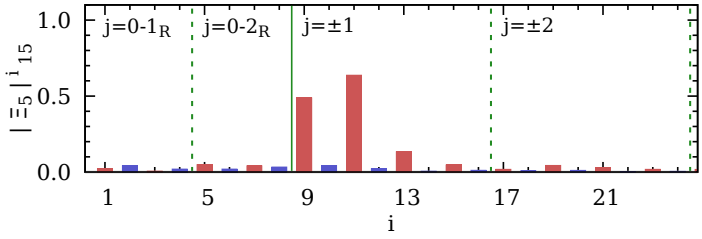

(d) $|\Xi_5|^i_{15} = |\Xi_5(\lambda_i, \lambda_{15})|$

Figure 6.17: $[1 \otimes \xi_5]$ leakage pattern for the first quartet of non-zero modes at $Q = -2$.

modes exist ($Q \neq 0$). In Figs. 6.16 and 6.17, leakage patterns of Γ_5 and Ξ_5 operators are presented, respectively, for non-zero modes $\{\lambda_9, \lambda_{11}, \lambda_{13}, \lambda_{15}\}$ in the $j = +1$ quartet when $Q = -2$. There are two quartets of right-handed would-be zero modes where $j = 0 - 1_R$ and $0 - 2_R$, which corresponds to $n_- = 0$ and $n_+ = 2$ with $Q = -2$ by the index theorem ($Q = n_- - n_+$).

As in the case of $Q = -1$ (Figs. 6.4 and 6.5) and $Q = 0$ (Figs. 6.12 and 6.13), Γ_5 leakages from non-zero modes of $j = +1$ mostly go to $j = -1$ quartet, and Ξ_5 leakages from non-zero modes of $j = +1$ mostly go to within $j = +1$ quartet itself. Leakages to other non-zero mode quartets and would-be zero mode quartets are negligibly small. The Ward identity also holds between two leakage patterns.

Lastly, in Figs. 6.18 and 6.19, leakage patterns of Γ_5 and Ξ_5 operators are presented, respectively, for non-zero modes $\{\lambda_{13}, \lambda_{15}, \lambda_{17}, \lambda_{19}\}$ in the $j = +1$ quartet when $Q = -3$. Their leakage patterns are also consistent with those for $Q = 0, -1, -2$ in our previous discussion.

6.3 Machine learning of leakage pattern

Staggered fermions respect the $\mathrm{U(1)_A}$ symmetry which induces the chiral Ward identities in Eq. (5.60), and also respect an approximate SU(4) taste symmetry which brings in the quartet behavior of the eigenvalue spectrum. Furthermore, a combined effect of those sym-

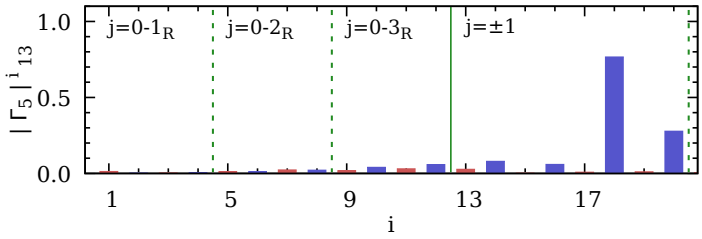

(a) $|\Gamma_5|^i_{13} = |\Gamma_5(\lambda_i, \lambda_{13})|$

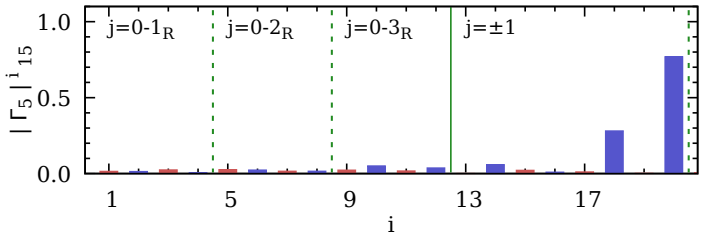

(b) $|\Gamma_5|^i_{15} = |\Gamma_5(\lambda_i, \lambda_{15})|$

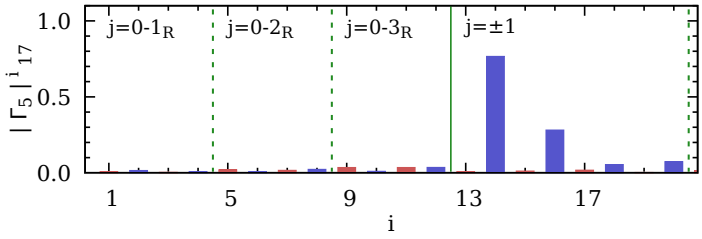

(c) $|\Gamma_5|^i_{17} = |\Gamma_5(\lambda_i, \lambda_{17})|$

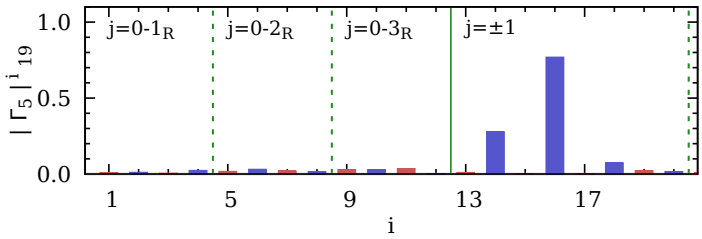

(d) $|\Gamma_5|^i_{19} = |\Gamma_5(\lambda_i, \lambda_{19})|$

Figure 6.18: $[\gamma_5 \otimes 1]$ leakage pattern for the first quartet of non-zero modes at $Q = -3$.

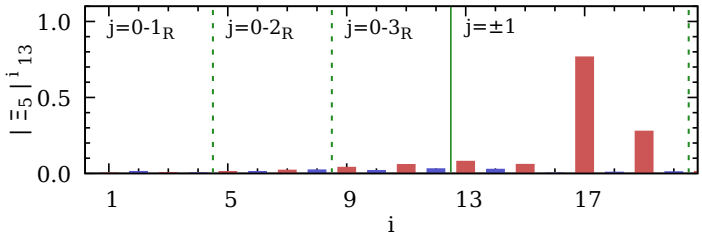

(a) $|\Xi_5|^i_{13} = |\Xi_5(\lambda_i, \lambda_{13})|$

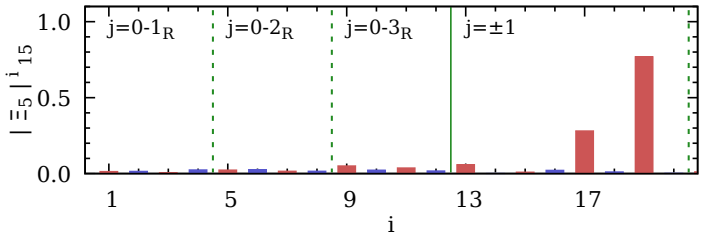

(b) $|\Xi_5|^i_{15} = |\Xi_5(\lambda_i, \lambda_{15})|$

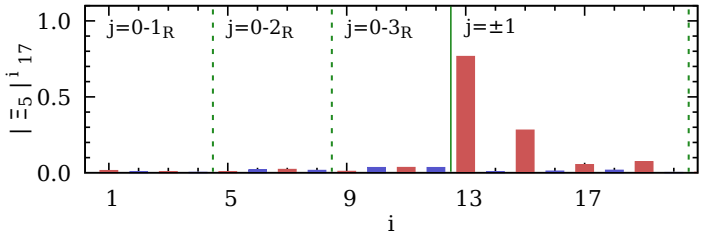

(c) $|\Xi_5|^i_{17} = |\Xi_5(\lambda_i, \lambda_{17})|$

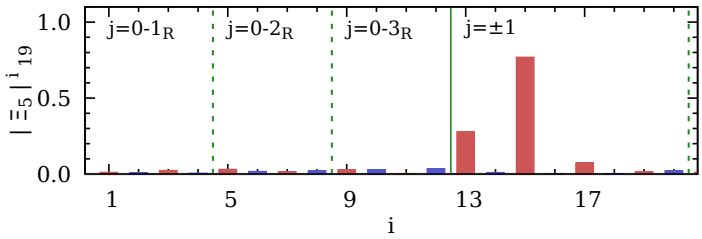

(d) $|\Xi_5|^i_{19} = |\Xi_5(\lambda_i, \lambda_{19})|$

Figure 6.19: $[1 \otimes \xi_5]$ leakage pattern for the first quartet of non-zero modes at $Q = -3$.

metries gives us distinctive leakage patterns for the chirality operator Γ_5 and the shift operator Ξ_5. In this section, the machine learning technique is applied to classify a quartet structure from the leakage pattern of chirality.

Fig. 6.20 illustrates matrix elements $|\Gamma_5|^i_j$ on a gauge configuration with $Q = 2$. Fig. 6.20(a) is for the 200 lowest eigenmodes and Fig. 6.20(b) is a zoomed-in version of Fig. 6.20(a) for the 32 lowest eigenmodes. Here, the depth of the blue color represents the magnitude of $|\Gamma_5|^i_j$ matrix element, and i, j run over the range of $[0, 199]$. One can identify two zero mode quartets (red boxes) by looking at the magnitude of diagonal components, which agrees with the topological charge $Q = 2$. Excluding the would-be zero modes, one can randomly choose a 15×15 sub-matrix of $|\Gamma_5|^i_j$ along the diagonal line of $|\Gamma_5|^i_j$ matrix elements. This 15×15 sub-matrix is the largest square sub-matrix of $|\Gamma_5|$ which contains all elements of only one quartet of non-zero modes and its parity partner quartet. Fig. 6.21 shows examples of classification for this sub-matrix. Here, the purpose of the machine learning is to find borders (black lines) of the non-zero mode quartet (or octet when the parity partners are included) in each sample. Arbitrary samples can be classified into eight different classes according to the location of the border line. Each class is labeled as in Fig. 6.21.

A deep learning model which combines the multi-layer perceptron

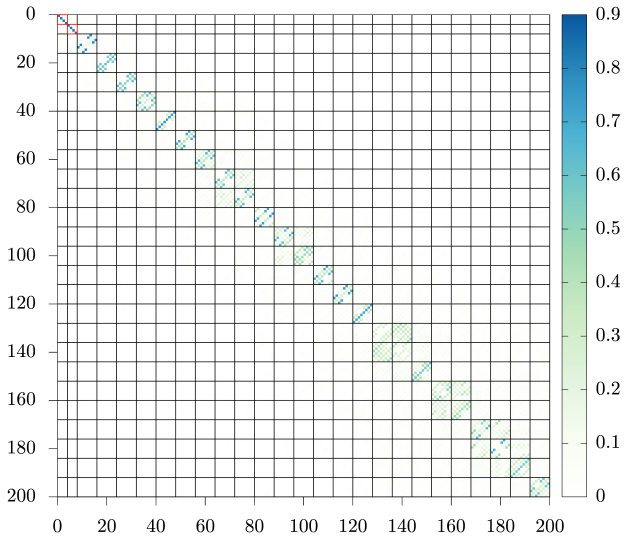

(a) 200×200

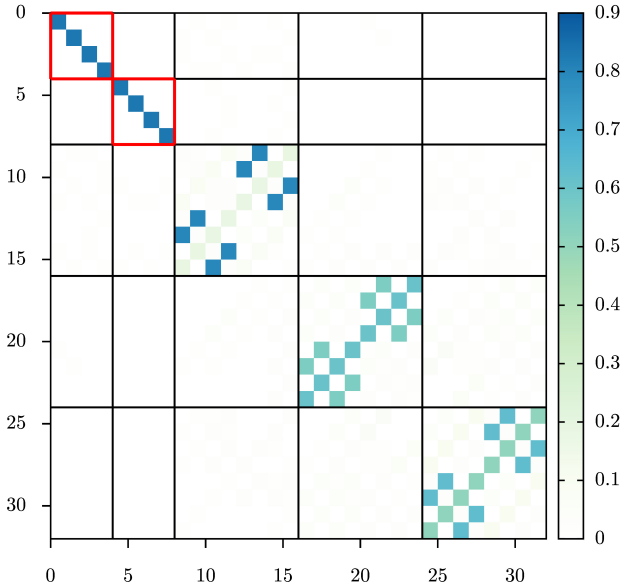

(b) 32×32

Figure 6.20: Matrix elements of $|\Gamma_5|$ for 200 and 32 of the lowest eigenmodes on a gauge configuration with $Q = 2$. Here, indices on both axes are the eigenvalue index. The color of each square represents the magnitude of corresponding matrix element. Black lines indicate borders of non-zero mode quartets, and red lines are of zero mode quartets.

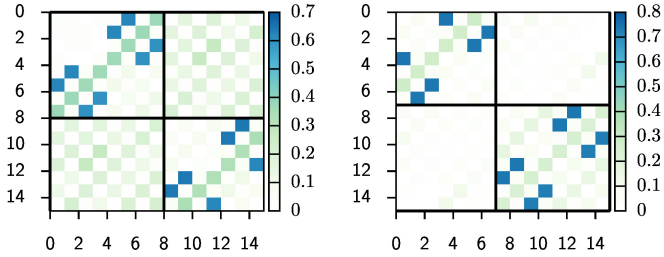

(a) class 0

(b) class 1

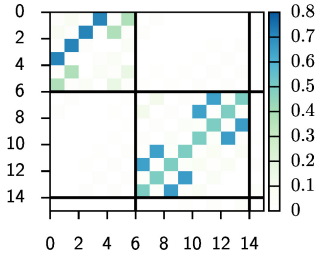

(c) class 2

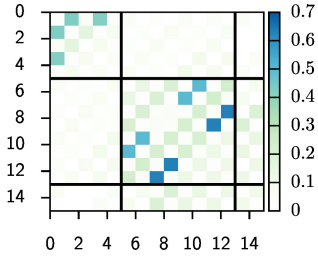

(d) class 3

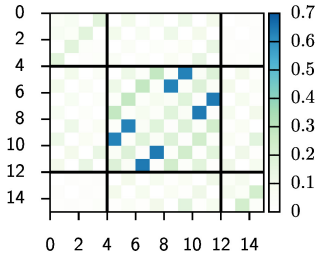

(e) class 4

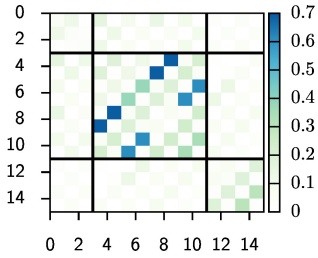

(f) class 5

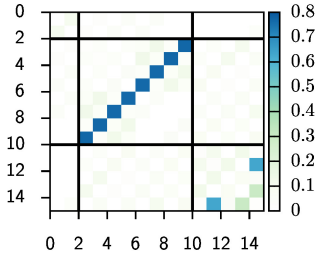

(g) class 6

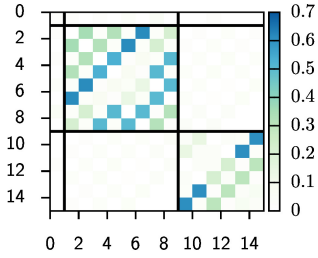

(h) class 7

Figure 6.21: Examples for our samples. Every sample contains only one non-zero mode quartet. There are eight kinds of classes according to the location of the borders of the quartet.

Table 6.7: Parameters for machine learning.

parameters	values
number of training configurations	120
number of training samples	1223
number of validation configurations	30
number of validation samples	308
number of test configurations	142
number of test samples	1448
loss function	categorical cross-entropy [63, 64]
optimization method	Adam [65]
activation function for hidden layers	ReLU [63]
activation function for output layer	softmax [63]

Table 6.8: Hyper-parameters for neural networks. One of the best performance model is shown, in which only MLP is used.

layer	type	number of units	activation
input	-	225	-
hidden #1	MLP	160	ReLU
hidden #2	MLP	1210	ReLU
hidden #3	MLP	1490	ReLU
output	MLP	8	Softmax

(MLP) [63] and the convolutional neural network (CNN) [63] is studied for this purpose. In Table 6.7, basic setups for the machine learning are written. The data measured over 292 gauge configurations are distributed over training set, validation set, and test set as in Table 6.7. Details on the gauge configuration ensemble are described in Table 4.1. For each gauge configuration, around tens of 15×15 matrix samples are generated from the 200 lowest eigenmodes without overlapping. The choice of loss function, optimization method, and activation functions are also described in Table 6.7. The best hyper-parameters such as the number of layers and the number of units for each layer are determined by Keras Tuner [64].

The accuracy of classification per gauge configuration is obtained by averaging the accuracies of the machine learning (ML) prediction for all the samples on a single gauge configuration. Hyper-parameters for the best performance are given in Table 6.8, which achieves an average accuracy of 96.5(156)% for 142 test gauge configurations. Among the test set, five gauge configurations are observed on which the average accuracy per gauge configuration is lower than 50%. Data show that some ghost (unphysical) eigenvectors are present in the eigenvalue spectrum on these gauge configurations, so that the ML prediction gives a wrong answer, not due to failure of the ML algorithm but due to human mistakes in labeling quartet samples based on the eigenvalue index. Excluding these five gauge configurations, the aver-

age accuracy of 99.4(23)% is achieved. This result demonstrates that our claim on the leakage pattern is universal over all the normal gauge configuration ensembles. Details on results of this ML research will be reported separately in Ref. [66].

Chapter 7

Renormalization of chirality

7.1 Zero modes and renormalization

As discussed in Sec. 6.2, there is practically no leakage for would-be zero modes in the chirality measurement. Hence, it is possible to determine the renormalization factor of chirality by imposing the index theorem.

Let us consider renormalization factors for the bilinear operators $\bar{\chi}\Gamma_5\chi$ and $\bar{\chi}\Gamma_\epsilon\chi$ as follows:

$$[\bar{\chi}\Gamma_5\chi]_R(\mu) = Z_{P\times S}(\mu)[\bar{\chi}\Gamma_5\chi]_B\,, \tag{7.1}$$

$$[\bar{\chi}\Gamma_\epsilon\chi]_R(\mu) = Z_{P\times P}(\mu)[\bar{\chi}\Gamma_\epsilon\chi]_B\,, \tag{7.2}$$

where the subscripts $[\cdots]_R$ and $[\cdots]_B$ represent renormalized and bare operators, respectively. Imposing the index theorem, Eq. (3.36) can be rewritten as

$$\begin{aligned} Q &= \frac{m_R}{N_t} \int d^4x \, [\bar{\chi}\Gamma_5\chi]_R \\ &= \frac{Z_m m_B}{N_t} \, Z_{P\times S} \int d^4x \, [\bar{\chi}\Gamma_5\chi]_B \, , \end{aligned} \tag{7.3}$$

where N_t is the number of tastes. By spectral decomposition,

$$N_t \, Q = Z_m Z_{P\times S} \, m_B \left(- \sum_\lambda \frac{\langle f^s_\lambda | \Gamma_5 | f^s_\lambda \rangle}{i\lambda + m_B} \right) . \tag{7.4}$$

Here, $\langle f^s_\lambda | \Gamma_5 | f^s_\lambda \rangle$ vanishes for $\lambda \neq 0$. Note that conserved $\mathrm{U(1)_A}$ symmetry implies $m_R[\bar{\chi}\Gamma_\epsilon\chi]_R = m_B[\bar{\chi}\Gamma_\epsilon\chi]_B$, thus, $Z_m Z_{P\times P} = 1$. Finally,

$$\begin{aligned} N_t \, Q &= - \frac{Z_{P\times S}}{Z_{P\times P}} \sum_{\lambda \in S_0} \langle f^s_\lambda | \Gamma_5 | f^s_\lambda \rangle \\ &\equiv - \kappa_P \sum_{\lambda \in S_0} \langle f^s_\lambda | \Gamma_5 | f^s_\lambda \rangle \, , \end{aligned} \tag{7.5}$$

where S_0 is the set of the would-be zero modes in staggered fermion formalism and

$$\kappa_P = \frac{Z_{P\times S}(\mu)}{Z_{P\times P}(\mu)} \, . \tag{7.6}$$

For $Q \neq 0$, κ_P can be easily computed by

$$\kappa_P = - \frac{4Q}{C_0} \, , \tag{7.7}$$

Table 7.1: Numerical results for κ_P.

topological charge	number of samples	κ_P
$\lvert Q\rvert = 1$	72	1.26(13)
$\lvert Q\rvert = 2$	68	1.22(3)
$\lvert Q\rvert = 3$	45	1.23(2)
weighted average	241	1.23(2)

where $C_0 = \sum_{\lambda \in S_0} \Gamma_5(\lambda, \lambda)$. One advantage of this scheme is that κ_P is independent of valence quark masses, even though the measurement can be performed with arbitrary masses for valence quarks. Numerical results for κ_P are summarized in Table 7.1. Since the topological charge Q is independent of renormalization scale and the C_0 is independent of renormalization scale, κ_P must be independent of the renormalization scale μ. This means that the scale dependence of $Z_{P\times S}(\mu)$ must cancel off that of $Z_{P\times P}(\mu)$. It would be nice to cross-check this property of κ_P in the RI-MOM scheme [67], and in the RI-SMOM scheme [68].

Chapter 8

Conclusion

General properties of the eigenvalue spectrum of Dirac operators in staggered fermion formalism are studied while focusing on the chiral symmetry and the taste symmetry. A new chirality operator Γ_5 and a new shift operator Ξ_5 are introduced and it is proved that they respect the continuum recursion relationships in Eqs. (5.9)-(5.12) and Eqs. (5.21)-(5.22). Using these advanced operators with nice chiral property, the leakage pattern of $|\Gamma_5|^{-j,m}_{\ell,m'}$ is related to that of $|\Xi_5|^{j,m}_{\ell,m'}$ through the Ward identity of the conserved $\mathrm{U(1)_A}$ symmetry.

Leakage patterns of Γ_5 and Ξ_5 for would-be zero modes are quite different from those for non-zero modes. This difference in leakage pattern allows us to distinguish the would-be zero modes from the non-zero modes even though we do not know a priori about the topological charge. Conversely, it is possible to determine the topological charge

from the leakage patterns of Γ_5 and Ξ_5, which is as reliable as typical field theoretical methods in the market such as the cooling, smearing, and gradient flow methods. The universality of this leakage patterns is verified by a machine learning analysis over the ensemble of gauge configurations.

It is also possible to determine the ratio of renormalization factors $\kappa_P = Z_{P\times S}(\mu)/Z_{P\times P}(\mu)$ from the chirality measurement of Γ_5.

The leakage pattern is a completely new concept introduced in this thesis and relevant papers in Ref. [14, 16, 17]. It allows us to study the low lying eigenvalue spectrum of staggered Dirac operators systematically. It helps us to understand how to fish out the taste symmetry and chiral symmetry embedded in the staggered eigenvalue spectrum. It will help us to dig out its related physics more efficiently.

Bibliography

[1] M. F. Atiyah and I. M. Singer, *The index of elliptic operators on compact manifolds*, *Bull. Am. Math. Soc.* **69** (1963) 422.

[2] T. Banks and A. Casher, *Chiral Symmetry Breaking in Confining Theories*, *Nucl. Phys.* **B169** (1980) 103.

[3] E. V. Shuryak and J. J. M. Verbaarschot, *Random matrix theory and spectral sum rules for the Dirac operator in QCD*, *Nucl. Phys.* **A560** (1993) 306 [hep-th/9212088].

[4] H. Leutwyler and A. V. Smilga, *Spectrum of Dirac operator and role of winding number in QCD*, *Phys. Rev.* **D46** (1992) 5607.

[5] A. Hasenfratz and F. Knechtli, *Flavor symmetry and the static potential with hypercubic blocking*, *Phys. Rev.* **D64** (2001) 034504 [hep-lat/0103029].

[6] W.-j. Lee and S. R. Sharpe, *One loop matching coefficients for improved staggered bilinears*, *Phys. Rev.* **D66** (2002) 114501 [hep-lat/0208018].

[7] HPQCD, UKQCD collaboration, *Highly improved staggered quarks on the lattice, with applications to charm physics*, *Phys. Rev.* **D75** (2007) 054502 [hep-lat/0610092].

[8] HPQCD, UKQCD collaboration, *The Index theorem and universality properties of the low-lying eigenvalues of improved staggered quarks*, *Phys. Rev. Lett.* **93** (2004) 241601 [hep-lat/0406010].

[9] HPQCD, UKQCD collaboration, *The Low-lying Dirac spectrum of staggered quarks*, *Phys. Rev.* **D72** (2005) 054501 [hep-lat/0507011].

[10] S. Durr, C. Hoelbling and U. Wenger, *Staggered eigenvalue mimicry*, *Phys. Rev.* **D70** (2004) 094502 [hep-lat/0406027].

[11] V. Azcoiti, G. Di Carlo, E. Follana and A. Vaquero, *Topological Index Theorem on the Lattice through the Spectral Flow of Staggered Fermions*, *Phys. Lett.* **B744** (2015) 303 [1410.5733].

[12] S. Durr, *Taste-split staggered actions: eigenvalues, chiralities and Symanzik improvement*, *Phys. Rev.* **D87** (2013) 114501 [1302.0773].

[13] D. H. Adams, *Theoretical foundation for the Index Theorem on the lattice with staggered fermions*, *Phys. Rev. Lett.* **104** (2010) 141602 [0912.2850].

[14] SWME collaboration, *How to fish out chiral symmetry and taste symmetry embedded in the eigenvalue spectrum of staggered Dirac operators*, 2005.10596.

[15] N. D. Cundy, H. Jeong and W. Lee, *Calculation of strange and light quark condensate using improved staggered fermions and overlap fermions*, *PoS* **LATTICE2015** (2016) 066.

[16] SWME collaboration, *How to identify zero modes for improved staggered fermions*, in *Proceedings, 35th International Symposium on Lattice Field Theory (Lattice 2017): Granada, Spain, June 18-24, 2017*, 2017, 1711.01826.

[17] SWME collaboration, *Chiral Ward identities for Dirac eigenmodes with staggered fermions*, *PoS* **LATTICE2019** (2019) 031 [2001.06568].

[18] T. DeGrand and C. E. Detar, *Lattice methods for quantum chromodynamics*. 2006.

[19] Particle Data Group collaboration, *Review of particle physics*, *Phys. Rev. D* **98** (2018) 030001.

[20] K. G. Wilson, *Confinement of Quarks*, .

[21] H. B. Nielsen and M. Ninomiya, *No Go Theorem for Regularizing Chiral Fermions*, *Phys. Lett. B* **105** (1981) 219.

[22] W.-J. Lee and S. R. Sharpe, *Partial flavor symmetry restoration for chiral staggered fermions*, *Phys. Rev.* **D60** (1999) 114503 [hep-lat/9905023].

[23] M. F. L. Golterman and J. Smit, *Selfenergy and Flavor Interpretation of Staggered Fermions*, *Nucl. Phys.* **B245** (1984) 61.

[24] MILC collaboration, *Nonperturbative QCD Simulations with 2+1 Flavors of Improved Staggered Quarks*, *Rev. Mod. Phys.* **82** (2010) 1349 [0903.3598].

[25] W.-j. Lee, *Perturbative improvement of staggered fermions using fat links*, *Phys. Rev.* **D66** (2002) 114504 [hep-lat/0208032].

[26] MILC collaboration, *Variants of fattening and flavor symmetry restoration*, *Phys. Rev.* **D60** (1999) 054503 [hep-lat/9903032].

[27] G. P. Lepage, *Flavor symmetry restoration and Symanzik improvement for staggered quarks*, *Phys. Rev.* **D59** (1999) 074502 [hep-lat/9809157].

[28] M. F. Golterman, *STAGGERED MESONS*, *Nucl. Phys. B* **273** (1986) 663.

[29] S. Weinberg, *The quantum theory of fields. Vol. 2: Modern applications*. Cambridge University Press, 2013.

[30] CP-PACS collaboration, *Topological susceptibility in lattice QCD with two flavors of dynamical quarks*, *Phys. Rev. D* **64** (2001) 114501 [hep-lat/0106010].

[31] P. Weisz, *Continuum Limit Improved Lattice Action for Pure Yang-Mills Theory. 1.*, *Nucl. Phys. B* **212** (1983) 1.

[32] P. Weisz and R. Wohlert, *Continuum Limit Improved Lattice Action for Pure Yang-Mills Theory. 2.*, *Nucl. Phys. B* **236** (1984) 397.

[33] M. Luscher and P. Weisz, *On-Shell Improved Lattice Gauge Theories*, *Commun. Math. Phys.* **97** (1985) 59.

[34] P. de Forcrand et al., *Improved cooling algorithm for gauge theories*, *Nucl. Phys. Proc. Suppl.* **47** (1996) 777 [hep-lat/9509064].

[35] P. de Forcrand et al., *Topology of the SU(2) vacuum: A Lattice study using improved cooling*, *Nucl. Phys.* **B499** (1997) 409 [hep-lat/9701012].

[36] A. Hasenfratz and C. Nieter, *Instanton content of the SU(3) vacuum*, *Phys. Lett.* **B439** (1998) 366 [hep-lat/9806026].

[37] M. Falcioni, M. L. Paciello, G. Parisi and B. Taglienti, *AGAIN ON SU(3) GLUEBALL MASS*, *Nucl. Phys.* **B251** (1985) 624.

[38] R. Narayanan and H. Neuberger, *Infinite N phase transitions in continuum Wilson loop operators*, *JHEP* **03** (2006) 064 [hep-th/0601210].

[39] M. Luscher and P. Weisz, *Perturbative analysis of the gradient flow in non-abelian gauge theories*, *JHEP* **02** (2011) 051 [1101.0963].

[40] R. Lohmayer and H. Neuberger, *Continuous smearing of Wilson Loops*, *PoS* **LATTICE2011** (2011) 249 [1110.3522].

[41] C. Alexandrou, A. Athenodorou, K. Cichy, A. Dromard, E. Garcia-Ramos, K. Jansen et al., *Comparison of topological charge definitions in Lattice QCD*, *Eur. Phys. J. C* **80** (2020) 424 [1708.00696].

[42] K. Cichy et al., *Comparison of different lattice definitions of the topological charge*, *PoS* **LATTICE2014** (2014) 075 [1411.1205].

[43] C. Lanczos, *An iteration method for the solution of the eigenvalue problem of linear differential and integral operators*, *J. Res. Natl. Bur. Stand. B Math. Sci.* **45** (1950) 255.

[44] T. A. DeGrand and P. Rossi, *Conditioning Techniques for Dynamical Fermions*, *Comput. Phys. Commun.* **60** (1990) 211.

[45] Y. Saad, *Chebyshev acceleration techniques for solving nonsymmetric eigenvalue problems*, *Math. Comp.* **42** (1984) 567.

[46] J. Smit and J. C. Vink, *Remnants of the Index Theorem on the Lattice*, *Nucl. Phys.* **B286** (1987) 485.

[47] R. Lehoucq and D. C. Sorensen, *Deflation techniques for an implicitly re-started arnoldi iteration*, *SIAM J. Matrix Anal. Appl* **17** (1996) 789.

[48] Y. Saad, *Chebyshev acceleration techniques for solving nonsymmetric eigenvalue problems*, *Math. Comp.* **42** (1984) 567.

[49] J. Cullum and R. Willoughby, *A survey of lanczos procedures for very large real 'symmetric' eigenvalue problems*, *Journal of Computational and Applied Mathematics* **s 12–13** (1985) 37–60.

[50] J. Cullum and R. A. Willoughby, *Computing eigenvalues of very large symmetric matrices—an implementation of a lanczos algorithm with no reorthogonalization*, *Journal of Computational Physics* **44** (1981) 329 .

[51] J. Cullum and R. Willoughby, *Lanczos algorithms for large symmetric eigenvalue computations. vol. i: Theory*, *Classics in Applied Mathematics* **I** (2002) .

[52] M. A. Clark, C. Jung and C. Lehner, *Multi-Grid Lanczos*, *EPJ Web Conf.* **175** (2018) 14023 [1710.06884].

[53] Y.-C. Jang and C. Jung, *Split Grid and Block Lanczos Algorithm for Efficient Eigenpair Generation*, *PoS* **LATTICE2018** (2019) 309.

[54] M. Luscher, *Local coherence and deflation of the low quark modes in lattice QCD*, *JHEP* **07** (2007) 081 [0706.2298].

[55] M. Luscher and P. Weisz, *Computation of the Action for On-Shell Improved Lattice Gauge Theories at Weak Coupling*, *Phys. Lett.* **158B** (1985) 250.

[56] M. G. Alford, W. Dimm, G. P. Lepage, G. Hockney and P. B. Mackenzie, *Lattice QCD on small computers*, *Phys. Lett.* **B361** (1995) 87 [hep-lat/9507010].

[57] F. D. R. Bonnet, D. B. Leinweber, A. G. Williams and J. M. Zanotti, *Improved smoothing algorithms for lattice gauge theory*, *Phys. Rev.* **D65** (2002) 114510 [hep-lat/0106023].

[58] J. Kim, W. Lee and S. R. Sharpe, *One-loop matching of improved four-fermion staggered operators with an improved gluon action*, *Phys. Rev.* **D83** (2011) 094503 [1102.1774].

[59] J. Kim, W. Lee and S. R. Sharpe, *One-loop matching factors for staggered bilinear operators with improved gauge actions*, *Phys. Rev.* **D81** (2010) 114503 [1004.4039].

[60] G. C. Donald, C. T. H. Davies, E. Follana and A. S. Kronfeld, *Staggered fermions, zero modes, and flavor-singlet mesons*, *Phys. Rev.* **D84** (2011) 054504 [1106.2412].

[61] M. F. L. Golterman, *Irreducible Representations of the Staggered Fermion Symmetry Group*, *Nucl. Phys.* **B278** (1986) 417.

[62] D. Verstegen, *Symmetry Properties of Fermionic Bilinears*, *Nucl. Phys.* **B249** (1985) 685.

[63] I. Goodfellow, Y. Bengio and A. Courville, *Deep Learning*. MIT Press, 2016.

[64] F. Chollet et al., "Keras." https://keras.io, 2015.

[65] D. P. Kingma and J. Ba, *Adam: A Method for Stochastic Optimization*, 1412.6980.

[66] H. Jeong, S. Lee and W. Lee.

[67] Y. Aoki et al., *Non-perturbative renormalization of quark bilinear operators and B(K) using domain wall fermions*, *Phys. Rev.* **D78** (2008) 054510 [0712.1061].

[68] C. Sturm, Y. Aoki, N. H. Christ, T. Izubuchi, C. T. C. Sachrajda and A. Soni, *Renormalization of quark bilinear operators in a momentum-subtraction scheme with a nonexceptional subtraction point*, *Phys. Rev.* **D80** (2009) 014501 [0901.2599].

[69] W. E. Arnoldi, *The principle of minimized iterations in the solution of the matrix eigenvalue problem*, *Quarterly of Applied Mathematics* **9** (1951) 17.

[70] L. N. Trefethen and I. David Bau, *Numerical Liniear Algebra*. 1997.

[71] D. C. Sorensen, *Implicitly restarted Arnoldi/Lanczos methods for large scale eigenvalue calculations*, in *Parallel numerical algorithms (Hampton, VA, 1994)*, vol. 4 of *ICASE/LaRC Interdiscip. Ser. Sci. Eng.*, pp. 119–165, Kluwer Acad. Publ., Dordrecht, (1997), DOI.

[72] Wikipedia contributors, "Eigenvalue algorithm — Wikipedia, the free encyclopedia." https://en.wikipedia.org/w/index.php?title=Eigenvalue_algorithm&oldid=966116991, 2020.

[73] J. H. Wilkinson, *Global convergence of tridiagonal* QR *algorithm with origin shifts*, *Linear Algebra and Appl.* **1** (1968) 409.

[74] T.-L. Wang and W. B. Gragg, *Convergence of the shifted QR algorithm for unitary Hessenberg matrices*, *Math. Comp.* **71** (2002) 1473.

Appendix A

Lanczos iteration method

A.1 Iterative eigenvalue-finding procedure

Let us assume the matrix A of our interest is an $m \times m$ square complex matrix. Finding eigenvalues λ of a square matrix A is equivalent to solving its characteristic equation $\det(A - \lambda I) = 0$. However, Abel-Ruffini theorem states that there is no general solution for polynomial equations of degree five or higher, which implies that we cannot find a direct eigenvalue-finding algorithm applicable to general matrices of dimensions higher than or equal to five. Even if we have a direct method under some restrictions, it would take very long computing time to find eigenvalues and eigenvectors of a high dimensional matrix such as Dirac matrix of our interest — Usually the dimension of Dirac matrix is around $10^5 \sim 10^9$.

Instead of direct method, 'iterative' methods are considered to find eigenvalues and eigenvectors of a very large matrix. Different from the direct method, where a finite number of sequences is required to solve the problem, an iterative method, in principle, requires infinite number of sequences to get the exact solution of the problem. In practice, however, a target precision for a problem is finite, usually lower than the machine precision, so the corresponding number of sequences is also enough to be finite. In particular for the matrix of very large size but a sparse form as the Dirac matrix, the iterative methods converge very fast, require much less computations than direct methods.

There are several iterative eigenvalue-finding algorithms in the market; QR iteration, Jacobi, bisection, divide-and-conquer, etc.. Among them, QR iteration method is reviewed in Section A.6. A useful preconditioning for those eigenvalue-finding algorithms is transforming into the so called Hessenberg form. A Hessenberg matrix H is an $m \times m$ square matrix satisfying $H_{ij} = 0$ for $i > j + 1$, i.e., entries below the first subdiagonal are zero. For example, when $m = 5$, a

Hessenberg matrix of dimension $m \times m$ can be expressed as

$$H = \begin{pmatrix} H_{11} & H_{12} & H_{13} & H_{14} & H_{15} \\ H_{21} & H_{22} & H_{23} & H_{24} & H_{25} \\ 0 & H_{32} & H_{33} & H_{34} & H_{35} \\ 0 & 0 & H_{43} & H_{44} & H_{45} \\ 0 & 0 & 0 & H_{54} & H_{55} \end{pmatrix}.$$

If A is Hermitian, then the Hessenberg transformation of A will become a Hermitian tridiagonal matrix. Transforming a matrix into the Hessenberg or Hermitian tridiagonal form can be done by a unitary transformation which preserves the eigenvalue spectrum. Such algorithms for the process are Arnolid algorithm [69] and Lanczos algorithm [43]. The former can be applied to any square matrix, while the latter is only applicable to the Hermitian matrices. If one obtains a Hessenberg (or Hermitian tridiagonal) transformation of the given matrix A, its eigenvalues and eigenvectors can be calculated by one of iterative eigenvalue-finding algorithms mentioned above, and then from those eigenvalues and eigenvectors it is straightforward to get the eigenvalues of eigenvectors of A.

Why is it better to transform into the Hessenberg form? Fig. A.1 shows a schematic diagram of finding eigenvalues by two phases. The first phase is the transformation into the Hessenberg form. It is a direct routine usually requires $O(m^3)$ flops (floating-point operations) [70].

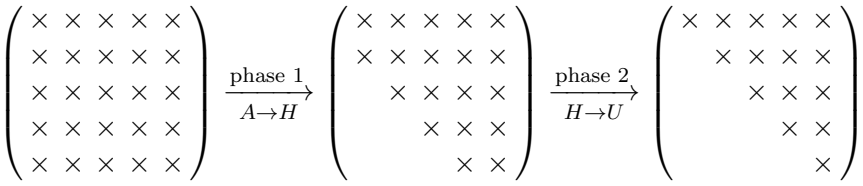

Figure A.1: Schematic diagram of eigenvalue finding process. × symbol indicates arbitrary numbers, and blank spaces are zero entries. H is a Hessenberg matrix and U is an upper triangular matrix.

The second phase is to transform the Hesesenberg matrix into upper triangular form, which is done by iterative eigenvalue algorithms. Finally, we get eigenvalues from the upper triangular matrix. Because the second phase is an iterative process, it requires infinite number of flops, in principle. In practice, however, it usually converges to double precision accuracy ($2^{-53} \approx 10^{-16}$) by $O(m)$ iterations, where each iteration requires $O(m^2)$ flops, thus $O(m^3)$ flops are required in total [70]. But if we skip the phase 1, each iteration of the phase 2 will require $O(m^3)$ flops and $O(m)$ or higher numbers of iterations, thus, in total $O(m^4)$ or higher flops will be required.

In addition to that, a real power of this iterative two phase method turns out when we need not all eigenvalues of the matrix. In the phase 1, Arnoldi (or Lanczos) algorithm generates each column of the Hessenberg (or Hermitian tridiagonal) matrix one by one, from left to right. Hence, at any iteration, we have a sub-matrix of the final Hessenberg(or Hermitian tridiagonal) matrix. Then, it is known that

the eigenvalues of this sub-Hessenberg matrix give estimates of the eigenvalues of the full matrix. Therefore, if we want to obtain only a portion of eigenvalues of a given matrix, it would be enough to run the phase 2 with the sub-matrix with much less computations. This is why Arnoldi and Lanczos algorithms are so favourable. The details on them are discussed in the following sections.

A.2 Krylov subspace and Arnoldi algorithm

Let A be an $m \times m$ square matrix and b be an m dimensional vector. The order-n Krylov subspace $\mathcal{K}_n(A, b)$ is defined as

$$\mathcal{K}_n(A, b) = \text{span}\{b, Ab, A^2b, \cdots, A^{n-1}b\}\,. \tag{A.1}$$

Let us consider $\mathcal{K}_{n+1}(A, b) = \text{span}\{b, Ab, A^2b, \cdots, A^{n-1}b, A^nb\}$. From here, the arguments (A, b) will be omitted for simplicity. Assume $b, Ab, A^2, \cdots, A^nb$ are linearly independent, in other words the subspace $\mathcal{K}_{n+1}$ has dimension $n + 1$. Let $\{q_1, q_2, \cdots, q_n\}$ be a basis of $\mathcal{K}_n$. One can find another unit vector $q_{n+1} \in \mathcal{K}_{n+1}$ orthogonal to $q_1, q_2, \cdots, q_n$ by, e.g., Gram-Schmidt orthogonalization. Then the set $\{q_1, q_2, \cdots, q_n, q_{n+1}\}$ becomes the basis of $\mathcal{K}_{n+1}$ and uniquely represents any vector in $\mathcal{K}_{n+1}$. Since $q_n \in \mathcal{K}_n$, it is evident that $Aq_n \in \mathcal{K}_{n+1}$,

so Aq_n can be represented by

$$Aq_n = h_{1,n}q_1 + h_{2,n}q_2 + \cdots + h_{n,n}q_n + h_{n+1,n}q_{n+1}\,. \tag{A.2}$$

Coefficients $h_{i,n}$ can be determined using the orthonormality of q_i:

$$h_{i,n} = q_i^\dagger A q_n\,. \tag{A.3}$$

As the basis vectors of $\mathcal{K}_{n+1}$ are constructed from the basis vectors of $\mathcal{K}_n$, one can construct the whole basis vectors from q_1, the basis of $\mathcal{K}_0 = b$, by induction. On this basis $\{q_1, q_2, \cdots, q_n\}$, the following relations hold for $Aq_1, Aq_2, \cdots, Aq_{n-1}$ in a similar fashion with Eq. (A.2):

$$Aq_1 = h_{1,1}q_1 + h_{2,1}q_2\,, \tag{A.4}$$

$$Aq_2 = h_{1,2}q_1 + h_{2,2}q_2 + h_{3,2}q_3\,, \tag{A.5}$$

$$\vdots$$

$$Aq_{n-1} = h_{1,n-1}q_1 + h_{2,n-1}q_2 + \cdots + h_{n,n-1}q_n\,. \tag{A.6}$$

Combining Eqs. (A.4)-(A.6) together with Eq. (A.2) in a matrix

form,

$$A\left(\begin{array}{c|c|c|c|c} q_1 & q_2 & \cdots & q_n & \end{array}\right) = \left(\begin{array}{c|c|c|c|c|c} q_1 & q_2 & \cdots & q_n & q_{n+1} & \end{array}\right) \begin{pmatrix} h_{1,1} & h_{1,2} & & \cdots & & h_{1,n} \\ h_{2,1} & h_{2,2} & & \cdots & & h_{2,n} \\ 0 & h_{3,2} & h_{3,3} & \cdots & & h_{3,n} \\ 0 & 0 & h_{4,3} & \cdots & & h_{4,n} \\ 0 & 0 & 0 & \ddots & & \vdots \\ \vdots & \vdots & \vdots & \ddots & h_{n,n-1} & h_{n,n} \\ 0 & 0 & 0 & \cdots & 0 & h_{n+1,n} \end{pmatrix} . \tag{A.7}$$

Here $(q_1|q_2|\cdots|q_n)$ represents a matrix of which the elements of each vector q_i fill i-th column. Let us rewrite this matrix equation simply as

$$AQ_n = Q_{n+1}\widetilde{H}_n \,. \tag{A.8}$$

Note that $\widetilde{H}_n$ — we save the notation H_n for later use — is not a square but $(n+1)\times n$ matrix of which elements below the subdiagonal are zero. Q_n and Q_{n+1} are $m \times n$ and $m \times (n+1)$ matrices satisfying

$$Q_n^\dagger Q_n = \mathbb{I}_n \,, \tag{A.9}$$

$$Q_{n+1}^\dagger Q_{n+1} = \mathbb{I}_{n+1} \,, \tag{A.10}$$

because q_i are orthonormal vectors. Note that the reverse forms $Q_n Q_n^\dagger$ and $Q_{n+1} Q_{n+1}^\dagger$ are not identities in general.

An important consequence of Eq. (A.8) is obtained by taking $Q_n^\dagger$ on the left:

$$Q_n^\dagger A Q_n = Q_n^\dagger Q_{n+1} \widetilde{H}_n = \left(\begin{array}{c|c} & 0 \\ \mathbb{I}_n & \vdots \\ & 0 \end{array}\right) \widehat{H}_n$$

$$= \begin{pmatrix} h_{1,1} & h_{1,2} & & \cdots & & h_{1,n} \\ h_{2,1} & h_{2,2} & & \cdots & & h_{2,n} \\ 0 & h_{3,2} & h_{3,3} & \cdots & & h_{3,n} \\ 0 & 0 & h_{4,3} & \cdots & & h_{4,n} \\ \vdots & \vdots & \ddots & \ddots & & \vdots \\ 0 & 0 & \cdots & 0 & h_{n,n-1} & h_{n,n} \end{pmatrix} \equiv H_n \,. \tag{A.11}$$

$H_n = Q_n^\dagger A Q_n$ is called a Hessenberg matrix of dimension n. It is just removing the last row of $\widetilde{H}_n$. In this way, one can transform the matrix A into the Hessenberg form H_n of any dimension $n < m$. Note that H_{n+1} can be constructed from $\widetilde{H}_n$ by putting one more column to the right. Arnoldi algorithm is constructing these $\widetilde{H}_n$ and Q_n.

Fig. A.2 describes the Arnoldi algorithm using modified Gram-Schmidt method. The modified Gram-Schmidt algorithm is more sta-

```
q_1 = b/‖b‖
for n = 1, 2, ··· , m
{
    v = A q_n
    for i = 1, 2, ··· , n
    {
        h_{i,n} = q_i^† v
        v = v − h_{i,n} q_i
    }
    h_{n+1,n} = ‖v‖
    q_{n+1} = v/h_{n+1,n}
}
```

Figure A.2: Arnoldi algorithm using modified Gram-Schmidt method

ble algorithm than its original one in numerical computation since it reduces the round-off error. Details on the modified Gram-Schmidt algorithm are introduced in Section A.7.

When A has full rank, Arnoldi algorithm gives a Hessenberg matrix $H \equiv H_m$ and a *unitary* matrix $Q \equiv Q_m$. They satisfy

$$H = Q^\dagger A Q \,, \tag{A.12}$$

$$A = Q H Q^\dagger \,. \tag{A.13}$$

Since Q is unitary, $Q^\dagger A Q$ is a unitary transformation which preserves the spectrum of eigenvalues. Hence, the eigenvalues of A can be obtained directly by computing the eigenvalues of H. As mentioned in section A.1, this process involving the transformation into Hessenberg

form requires less computations than computing the eigenvalues of A directly.

A.3 Arnoldi iteration method

In most practices, not all the eigenvalues of $m \times m$ matrix A are needed, but only a small portions of them. In those cases, there is no need of performing all the iterations of n, i.e., until $n = m$. Each n-th step gives a Hessenberg matrix H_n as in Eq. (A.11). It is known that the eigenvalues of H_n, which is a submatrix of H in Eq. (A.12), estimate 'some' eigenvalues of A. Only intuitive understandings of this phenomenon exist at this moment. One of them is described here.

Let us consider the characteristic polynomial p_A of the matrix A. By Cayley-Hamilton theorem, $p_A(A) = 0$. If a matrix B has eigenvalues approximate to those of A, its characteristic polynomial p_B has zeros near the eigenvalues of A. When whole eigenvalue spectrum of B is close to that of A or a sub-group of eigenvalue spectrum of A, $p_B(A)$ also close to zero, or $\|p_B(A)\|$ is small ($\|\|$ is the matrix norm.). Note that the characteristic polynomial of an $n \times n$ matrix is a monic polynomial of degree n. A monic polynomial is a polynomial for which the coefficient of the highest degree term is 1.

Now, let us consider the following theorem:

Theorem 3. *For monic polynomials p of degree n, the norm $\|p(A)b\|$*

has minimum when $p = p_n$ where p_n is the characteristic polynomial of Hessenberg matrix H_n. If Krylov subspace $\mathcal{K}_n(A, b)$ has full dimension n, p_n is the unique minimizer.

Proof. Since p is monic, $p(A)b = A^n b + \sum_{i=0}^{n-1} c_i A^i b$. Noting that $\sum_{i=0}^{n-1} c_i A^i b \in \mathcal{K}_n$ and Q_n is composed of the bases of $\mathcal{K}_n$, we can rewrite $p(A)b$ as

$$p(A)b = A^n b - Q_n y\,, \tag{A.14}$$

for some $y \in \mathbb{C}^n$. To minimize $\|A^n b - Q_n y\|$, $A^n b - Q_n y = p(A)b$ must be perpendicular to $Q_n y \in \mathcal{K}_n$. Hence, the problem minimizing $\|p(A)b\|$ is equal to find p satisfying $p(A)b \perp \mathcal{K}_n$. This implies $Q_n^\dagger\, p(A)\, b = 0$. Using Eq. (A.13),

$$Q_n^\dagger Q\, p(H) Q^\dagger b = 0\,. \tag{A.15}$$

Note that

$$Q_n^\dagger Q = \left(\begin{array}{c|ccc} & 0 & \cdots & 0 \\ \mathbb{I}_n & \vdots & \ddots & \vdots \\ & 0 & \cdots & 0 \end{array}\right), \qquad Q^\dagger b = \begin{pmatrix} q_1^\dagger b \\ 0 \\ \vdots \\ 0 \end{pmatrix}, \tag{A.16}$$

because of the orthonormality of q_i's and $q_1 \parallel b$. Thus, Eq. (A.15) implies that the first n elements of the first column of $p(H)$ must be

zero. Now let us think of the structure of H:

$$H = \left(\begin{array}{c|c} H_n & X \\ \hline Y & Z \end{array} \right) . \tag{A.17}$$

where elements of Y are zero except the top right corner: $Y_{1,n} = H_{n+1,n} \neq 0$. Noting that $(H_n^l)_{i,j} = 0$ for $i > j + l$, one can show that for $l \leq n$ the first n elements of the first column of H^l are those of H_n^l. Since the degree of p is n, the condition from Eq. (A.15) — the first n elements of the first column of $p(H)$ must be zero — is equivalent to those of $p(H_n)$ must be zero. And the characteristic polynomial p_n of H_n satisfies that condition because $p_n(H_n) = 0$.

Now, let us assume Krylov subspace $\mathcal{K}_n$ has a dimension n. In other words, $\{b, Ab, \cdots A^{n-1}b\}$ are linearly independent. Suppose there exists another monic polynomial q of degree n satisfying $q(A)b \perp \mathcal{K}_n$. Since both p_n and q are monic, $r \equiv p_n - q$ is of degree $n - 1$, and r satisfies $r(A)b = 0$. Since $r(A)b \in \mathcal{K}_n$, by assumption $r(A)b = 0$ only when $r = 0$. Therefore, the characteristic polynomial p_n of H_n is a unique monic polynomial of degree n minimizing $\|p(A)b\|$. □

From Theorem 3, although not rigorous, one would deduce the characteristic polynomial of H_n has zeros close to those of p_A, so that the eigenvalues of H_n give estimates of 'some' eigenvalues of A. Thus, when applying the Arnoldi algorithm in Fig. A.2, for each or every a

few iterations of n one computes the eigenvalues of the sub-matrix H_n by using the iterative eigenvalue algorithms such as QR iteration. It will give estimates of some eigenvalues of A. This procedure is called Arnoldi *iteration*.

Then, what are those 'some' eigenvalues of A which H_n mimics? Because H_n has only $n \leq m$ eigenvalues, it can approximate at most n eigenvalues of A. Basically Arnoldi (or Lanczos) algorithm is based on Krylov subspace, which is constructed by powers of A, generating its basis vectors essentially amplifies the contribution by the largest or the smallest eigenvalues as in usual power method. Hence, the eigenvalues of H_n could converge to the largest or the smallest eigenvalues of A first. However, a more crucial property regarding the convergence of Arnoldi and Lanczos algorithm is that the sequence of the eigenvalues of H_n converges to *extreme* eigenvalues of A first [70]. Here, extreme means geometrically 'not dense' in the eigenvalue spectrum. For example, let us consider a case that all eigenvalues swarm in a $\mathbb{C}$ ball except an eigenvalue fairly apart from them. In the Arnoldi iteration, an eigenvalue of H_n will converge to the separated eigenvalue first and quickly. But the other eigenvalues of H_n converge to the eigenvalues in the ball slowly. Techniques to get Arnoldi iteration converges to wanted eigenvalues fast are discussed in Section A.5.

Before closing this section, let us consider when A has some degenerate eigenvalues. If A has only $n < m$ numbers of different eigen-

values, one can find the minimal polynomial μ_A of A, which is a monic polynomial of degree n satisfying $\mu_A(A) = 0$. Since $\|\mu_A(A)b\|$ is zero, μ_A gives the minimum of the norm $\|p(A)b\|$ in Theorem 3. Hence, μ_A must be the characteristic polynomial of H_n, and as a result, Arnoldi iteration finds all eigenvalues of A exactly after n-th iterations.

A.4 Lanczos algorithm and Lanczos iteration method

Now let us focus on our real interest, Hermitian case. Although lattice Dirac operators are not Hermitian itself in general, they can be transformed to Hermitian form easily. In staggered fermion formalism, the massless staggered Dirac operator D_s is anti-Hermitian. However, for example, if we consider $D_s{}' \equiv iD_s$, $D_s{}'$ is Hermitian and the eigenvalues of D_s can be obtained from the eigenvalues of $D_s{}'$ easily without further computational cost.

Eigenvalues of a Hermitian $m \times m$ matrix A can be calculated in the same way as for non-Hermitian case in Fig. A.1, but here H is Hermitian tridiagonal and U is diagonal. It can be shown easily that if A is Hermitian, H and U are also Hermitian (see Eq. (A.12)). Hence, the recurrence relation Eq. (A.2) becomes a simpler three term

$q_0 = 0$
$\beta_0 = 0$
$q_1 = b/\|b\|$
`for` $n = 1, 2, \cdots, m$
{
    $v = Aq_n$
    $\alpha_n = q_n^\dagger v$ `// diagonal elements :` $\alpha_n = h_{n,n}$
    $v = v - \beta_{n-1} q_{n-1} - \alpha_n q_n$
    $\beta_n = \|v\|$ `// subdiagonal elements :` $\beta_n = h_{n+1,n}$
    $q_{n+1} = v/\beta_n$
}

Figure A.3: Lanczos algorithm using modified Gram-Schmidt method

formula:

$$Aq_n = h_{n-1,n} q_{n-1} + h_{n,n} q_n + h_{n+1,n} q_{n+1} \,. \tag{A.18}$$

Note that only two precedent basis vectors q_{n-1} and q_n are required to construct a new basis q_{n+1} from them, by which we don't have to keep all the basis vectors. In addition, $h_{n-1,n} = h^*_{n,n-1}$, so it is already computed in the previous step. Using these properties, the Arnoldi algorithm in Fig. A.2 can be simplified for Hermitian case, which is so called *Lanczos* algorithm. Fig. A.3 illustrates the Lanczos algorithm. Instead of saving two-dimensional array (matrix) $H_m = (h_{i,j})$, to save the memory, here two one-dimensional arrays α and β are used.

Since Lanczos algorithm is just Hermitian matrix version of the

Arnoldi algorithm, properties of Arnoldi algorithm are still applicable in the same way. The eigenvalues of the Hermitian tridiagonal matrix H_n, a sub-matrix of H_m, obtained by Lanczos algorithm give estimates of *some* eigenvalues of the Hermitian matrix A. They converge to extreme eigenvalues of A first and fast. Lanczos iteration method is to compute eigenvalues of a Hermitian matrix using iterative eigenvalue-finding routines with Lanczos algorithm as in the Arnoldi iteration method.

A.5 Improvements on Arnoldi and Lanczos iterations

Arnoldi (Lanczos) iteration works with the sub-matrix H_n of $n \times n$ dimension, not with the full Hessenberg matrix H of $m \times m$. Hence, one may wish that Arnoldi (Lanczos) iteration finds the wanted eigenvalues of a required precision with as less iterations as possible. There are two popular improvement techniques for Arnoldi (Lanczos) iteration: (1) Implicit restart is to remove unwanted eigenvalues, so that Arnoldi (Lanczos) iteration finds wanted eigenvalues from a smaller sub-matrix with lower density of the spectrum. (2) Polynomial acceleration enhances the convergence of the eigenvalue estimates.

A.5.1 implicit restart

In Arnoldi (Fig. A.2) and Lanczos (Fig. A.3) algorithms, as the iteration count n increases, the amount of the calculations in a step increases[1]. In addition, the size of the Hessenberg (or Hermitian tridiagonal) matrix H_n enlarges, so the amount of the computations required for the eigenvalue calculation of H_n increases. Problem is that one can not pick an eigenvalue of H_n which estimates a specific eigenvalue of A. Thus, one should perform the Arnoldi (Lanczos) iterations until the eigenvalues of H_n give estimates of all the wanted eigenvalues. Implicit restart, introduced by D. C. Sorensen [71], removes unnecessary eigenvalues from A, so that H_n gives estimates of the eigenvalues while retaining the size of the sub-matrix.

Let us suppose that after n iterations an eigenvalue of H_n converges to an unwanted eigenvalue μ. The idea of the implicit restart is simple: restart Arnoldi (Lanczos) iteration with a new initial vector $(A - \mu\mathbb{I})b$. This removes the contribution of the eigenvector corresponding to the eigenvalue μ from b. However, if we indeed restart the Arnoldi iteration from the beginning ($n = 1$), that may require even more calculations than without restarting. The essence of the *implicit* restart is that we can restart the Arnoldi iteration from $(n-1)$-th iteration with an updated Hessenberg matrix $\widetilde{H}'_{n-2}$ and basis matrix

[1]This is true only for Arnoldi iteration in theory. However, basic Lanczos algorithm suffers the orthogonality problem, so in practice the claim is also applied to the modified versions of the Lanczos iteration.

$Q_{n-1}{}'$.

Remind that the Arnoldi algorithm is based on Eq. (A.8), which can be rewritten by

$$AQ_n = Q_n H_n + h_{n+1,n} q_{n+1} \mathbb{e}_n^{\mathsf{T}} \,. \tag{A.19}$$

Subtracting μQ_n to both sides,

$$(A - \mu \mathbb{I}) Q_n = Q_n (H_n - \mu \mathbb{I}) + h_{n+1,n} q_{n+1} \mathbb{e}_n^{\mathsf{T}} \,. \tag{A.20}$$

Now let us perform QR decomposition to $H_n - \mu \mathbb{I}$:

$$H_n - \mu \mathbb{I} = VR \,, \tag{A.21}$$

where V is an $n \times n$ unitary matrix and R is an $n \times n$ (right) upper triangular matrix. Details on the QR decomposition are explained in Section A.6. Inserting Eq. (A.21) to Eq. (A.20),

$$(A - \mu \mathbb{I}) Q_n = Q_n VR + h_{n+1,n} q_{n+1} \mathbb{e}_n^{\mathsf{T}} \,. \tag{A.22}$$

Let $W_n \equiv Q_n V$. Q_n satisfies $Q_n^\dagger Q_n = \mathbb{I}_n$, and since V is unitary, W_n also satisfies

$$W_n^\dagger W_n = V^\dagger Q_n^\dagger Q_n V = \mathbb{I}_n \,. \tag{A.23}$$

Eq. (A.22) becomes

$$(A - \mu\mathbb{I})Q_n = W_n R + h_{n+1,n} q_{n+1} \mathbb{e}_n^{\mathsf{T}} \,. \tag{A.24}$$

Let $W_n = (w_1|w_2|\cdots|w_n)$. Reminding $Q_n = (q_1|q_2|\cdots|q_n)$, Eq. (A.24) gives

$$(A - \mu\mathbb{I})q_1 = w_1 R_{1,1} \,, \tag{A.25}$$

$$(A - \mu\mathbb{I})q_2 = w_1 R_{1,2} + w_2 R_{2,2} \,, \tag{A.26}$$

$$\vdots$$

$$(A - \mu\mathbb{I})q_{n-1} = \sum_{i=1}^{n-1} w_i R_{i,n-1} \,, \tag{A.27}$$

$$(A - \mu\mathbb{I})q_n = \sum_{i=1}^{n} w_i R_{i,n} + h_{n+1,n} q_{n+1} \,. \tag{A.28}$$

Eq. (A.25) indicates that w_1 is proportional to $(A - \mu\mathbb{I})q_1$. Since q_2 is spanned by q_1 and Aq_1, $(A - \mu\mathbb{I})q_2$ can be spanned by $(A - \mu\mathbb{I})q_1$ and $A(A - \mu\mathbb{I})q_1$, hence by w_1 and Aw_1. This implies that w_2 can be spanned by w_1 and Aw_1 according to Eq. (A.26). In the same way, one can show that for $k < n$ — not for $k = n$ — w_k can be spanned by $\{w_1, Aw_1, A^2w_1, \cdots, A^{k-1}w_1\}$, i.e., $w_k \in \mathcal{K}_k(A, w_1)$. Because w_k's are orthonormal from Eq. (A.23), they — except w_n — are indeed the basis vectors of the Krylov subspace $\mathcal{K}_{n-1}(A, w_1)$ obtained by $(n-1)$-th Arnoldi iteration for A with a new initial vector w_1.

What about the Hessenberg matrix H_n? Rewriting Eq. (A.19) by multiplying V to the right side, and inserting $\mathbb{I}_n = VV^\dagger$ gives

$$AQ_nV = Q_nVV^\dagger H_nV + h_{n+1,n}q_{n+1}\mathbb{e}_n^\intercal V\,. \tag{A.29}$$

Let ${Q_n}' \equiv Q_nV(= W)$, ${H_n}' \equiv V^\dagger H_nV$, and $\mathbb{e}_n^{\intercal\prime} \equiv \mathbb{e}_n^\intercal V$. Then,

$$A{Q_n}' = {Q_n}'{H_n}' + h_{n+1,n}q_{n+1}\mathbb{e}_n^{\intercal\prime}\,. \tag{A.30}$$

Lemma 1. *For an invertible Hessenberg matrix H, perform QR decomposition: $H = QR$. Then the unitary matrix Q is also a Hessenberg form.*

Proof. QR decomposition decomposes a matrix to the product of unitary matrix Q and (right) upper triangular matrix R. (Details are in Section A.6.) Since H is invertible, $\det\{H\} \neq 0$, so $\det\{R\} \neq 0$, thus, R is also invertible. Applying R^{-1} to the right gives $Q = HR^{-1}$. The inverse of the right triangular matrix is again an upper triangular matrix. Hence, Q is the product of a Hessenberg matrix and an upper triangular matrix.

Now let us consider an element of Q, given by $Q_{i,j} = \sum_k H_{i,k}R^{-1}_{k,j}$. Note that $H_{i,k} = 0$ if $i > k+1$ and $R^{-1}_{k,j} = 0$ if $k > j$. For given (i,j), $H_{i,k}R^{-1}_{k,j} = 0$ if $k < i-1$ or $k > j$. If $i > j+1$ (i.e., $i-1 > j$), $k < i-1$ or $k > j$ for any k, hence $H_{i,k}R^{-1}_{k,j} = 0$ for any k. As a result, $Q_{i,j} = 0$

for $i > j + 1$. This concludes Q is a Hessenberg form. □

If Arnoldi (Lanczos) algorithm has not broken until n-th iteration step, H_n is of full rank, thus, invertible. If H_n is invertible, so is $H_n - \mu\mathbb{I}$. Since $H_n - \mu\mathbb{I}$ is still a Hessenberg form, by Lemma 1, V is also a Hessenberg form.

Lemma 2. *$H_n{}' = V^\dagger H_n V$ is a Hessenberg matrix.*

Proof. From Eq. (A.21), $H_n = VR + \mu\mathbb{I}$. Inserting this into $H_n{}'$,

$$H_n{}' = V^\dagger VRV + \mu V^\dagger \mathbb{I} V \tag{A.31}$$

$$= RV + \mu\mathbb{I}\,. \tag{A.32}$$

R is a right triangular form and V is a Hessenberg form, so RV is still a Hessenberg form — this can be proved in the same way with Lemma 1. Therefore, $RV + \mu\mathbb{I}$ is also a Hessenberg form. □

Now let us inspect the last term in Eq. (A.30). Since V is a Hessenberg form,

$$\mathbb{e}_n^{\mathsf{T}\prime} = \mathbb{e}_n^{\mathsf{T}} V = \begin{pmatrix} 0 & \cdots & 0 & V_{n,n-1} & V_{n,n} \end{pmatrix}. \tag{A.33}$$

Hence $q_{n+1}\mathbb{e}_n^{\mathsf{T}\prime}$ has non-zero entries only at the rightmost two columns.

Removing those two columns from Eq. A.30 gives,

$$A\left(\begin{array}{c|c|c} & & \\ q'_1 & \cdots & q'_{n-2} \\ & & \end{array}\right) = \left(\begin{array}{c|c|c} & & \\ q'_1 & \cdots & q'_{n-1} \\ & & \end{array}\right) \begin{pmatrix} h'_{1,1} & \cdots & & h'_{1,n-2} \\ h'_{2,1} & \ddots & & \vdots \\ 0 & \ddots & & \\ \vdots & \ddots & h'_{n-2,n-3} & h'_{n-2,n-2} \\ 0 & \cdots & 0 & h'_{n-1,n-2} \end{pmatrix}, \tag{A.34}$$

where I used notation ${Q_n}' = (q'_1|\cdots|q'_n)$ and ${H_n}' = (h'_{i,j})$ as before. This is reminiscent of Eq. (A.7). It can be rewritten as Eq. (A.8):

$$AQ'_{n-2} = Q'_{n-1}\widetilde{H}'_{n-2}\,. \tag{A.35}$$

Indeed, $(n-1)\times(n-2)$ submatrix $\widetilde{H}'_{n-2}$ of ${H_n}'$ is the matrix $\widetilde{H}$ obtained by $(n-2)$-th Arnoldi iteration with the initial vector w_1. This result means that we can *implicitly restart* Arnoldi (Lanczos) iteration with the initial vector $q'_1 \propto (A-\mu\mathbb{I})q_1$ from the $(n-1)$-th iteration with Q'_{n-1} and $\widetilde{H}'_{n-2}$.

This implicit restarting can be expanded to multiple unwanted eigenvalues. Let us consider we perform the implicit restart p times in order to remove the eigenvalues $\mu_1, \mu_2, \cdots, \mu_p$. The first restart will

do QR decomposition of

$$H_n - \mu_1 \mathbb{I} = V_1 R_1 \,. \tag{A.36}$$

And the implicit restart for this step will give

$$H_n^{(1)} \equiv V_1^\dagger H_n V_1 \,. \tag{A.37}$$

The second restart to remove μ_2 does similar works.

$$H_n^{(1)} - \mu_2 \mathbb{I} = V_2 R_2 \tag{A.38}$$

$$H_n^{(2)} \equiv V_2^\dagger H_n^{(1)} V_2 \,. \tag{A.39}$$

Note that the dimension of the matrix is retained on the $n \times n$, not being reduced to $(n-2) \times (n-2)$, because the last term in Eq. (A.22) does not affect these procedures. However, one should keep in mind that the column vectors of $Q_n^{(1)} \equiv Q_n V_1$ except the n-th column constitute the bases of $\mathcal{K}_{n-1}$ and in the same manner the first $n-2$ column vectors of $Q_n^{(2)} \equiv Q_n^{(1)} V_2$ are bases of $\mathcal{K}_{n-2}$. In general for the $i \in \{1, \cdots, p\}$-th restart,

$$H_n^{(i-1)} - \mu_i \mathbb{I} = V_i R_i \,, \tag{A.40}$$

$$H_n^{(i)} \equiv V_i^\dagger H_n^{(i-1)} V_i \,, \tag{A.41}$$

where $H_n^{(0)} \equiv H_n$. The first $n-i$ column vectors of $Q_n^{(i)} \equiv Q_n^{(i-1)} V_i$ are bases of $\mathcal{K}_{n-i}$, of which initial vector is $(A-\mu_i \mathbb{I})(A-\mu_{i-1}\mathbb{I})\cdots(A-\mu_1\mathbb{I}))b$. If $H_n^{(i-1)}$ is a Hessenberg form, V_i obtained by Eq. (A.40) is again a Hessenberg form by Lemma 1, and then $H_n^{(i)}$ given by Eq. (A.41) also becomes a Hessenberg form by Lemma 1. Because $H_n^{(0)} (= H_n)$ is a Hessenberg form, by induction, every $H_n^{(i)}$ is a Hessenberg form and so is corresponding V_i.

Combining those p step restarts,

$$AQ_nV_1 = Q_nV_1V_1^\dagger H_n^{(0)} V_1 + h_{n+1,n} q_{n+1} \mathbb{e}_n^\intercal V_1 \,, \tag{A.42}$$

$$AQ_nV_1V_2 = Q_nV_1V_2V_2^\dagger H_n^{(1)} V_2 + h_{n+1,n} q_{n+1} \mathbb{e}_n^\intercal V_1V_2 \,, \tag{A.43}$$

$$\vdots$$

$$AQ_nV_1V_2\cdots V_p = Q_nV_1V_2\cdots V_pV_p^\dagger H_n^{(p-1)} V_p + h_{n+1,n} q_{n+1} \mathbb{e}_n^\intercal V_1V_2\cdots V_p \,. \tag{A.44}$$

Let $V \equiv V_1V_2\cdots V_p$. Then,

$$AQ_nV = Q_nVH_n^{(p)} + h_{n+1,n} q_{n+1} \mathbb{e}_n^\intercal V \tag{A.45}$$

$$\Leftrightarrow AQ_n{}' = Q_n{}' H_n^{(p)} + h_{n+1,n} q_{n+1} \mathbb{e}_n^{\intercal\prime} \,, \tag{A.46}$$

where $Q_n{}' \equiv Q_nV$ and $\mathbb{e}_n^{\intercal\prime} \equiv \mathbb{e}_n^\intercal V$ as before. Since $Q_n{}'$ is constructed through the p step restarts in order, its first $n-p$ column vectors constitute the basis of $\mathcal{K}_{n-p}$ of which the initial vector does not contain

the eigenvectors corresponding to the eigenvalues $\mu_1, \cdots, \mu_p$. Meanwhile, V has zeros below the p-th subdiagonal because it is the product of p Hessenberg matrices. Hence it follows that the first $n-p-1$ columns of $q_{n+1}\mathbb{e}_n^{\mathsf{T}\prime}$ are zero. In the end, we can *implicitly restart* from the $(n-p)$-th Arnoldi (Lanczos) iteration with the submatrices $Q'_{n-p} = (q'_1|\cdots|q'_{n-p})$ and $\widetilde{H}^{(p)}_{n-p-1}$ — they satisfy $AQ'_{n-p-1} = Q'_{n-p}\widetilde{H}'_{n-p-1}$ — in the absence of eigenvalues $\mu_1, \cdots, \mu_p$.

A.5.2 polynomial acceleration

As mentioned in section A.3, the convergence of the eigenvalue estimates in Arnoldi (Lanczos) iteration depends on the density of the eigenvalues. Suppose a matrix A has two near-degenerate eigenvalues λ_1 and λ_2, separated by a small distance $|\lambda_2 - \lambda_1| \ll 1$. Considering a polynomial $p(x) = x^n$ with $n > 1$, $p(A) = A^n$ has eigenvalues λ_1^n and λ_2^n with the same eigenvectors with A. If we write $\lambda_2 = \lambda_1 + \delta$, $|\delta| \ll 1$ by assumption. Then the distance between the eigenvalues of A^n is

$$\begin{aligned} |\lambda_2^n - \lambda_1^n| &= |(\lambda_1+\delta)^n - \lambda_1^n| = |n\lambda_1^{n-1}\delta + O(\delta^2)| \\ &\simeq n|\lambda_1^{n-1}||\delta| = n|\lambda_1|^{n-1}|\lambda_2 - \lambda_1|\,. \end{aligned} \tag{A.47}$$

If $|\lambda_1| \geq 1$, $|\lambda_2^n - \lambda_1^n| > |\lambda_2 - \lambda_1|$, and their ratio is $n|\lambda_1|^{n-1}$. This means the distance between two eigenvalues of A^n is farther than between

those of A, in other words, the density of the eigenvalues of A^n is lower than that of A. Therefore, Arnoldi (Lanczos) iteration for A^n would need less iterations to converge than that for A. Although the Arnoldi (Lanczos) iteration for A^n requires extra calculation of A^n and n-th root to the eigenvalues, it would be more beneficial to perform less iterations. In this way, one can *accelerate* the convergence of the Arnoldi (Lanczos) iteration method by making use of a polynomial that lowers the density of the wanted eigenvalues.

It is important to use a proper polynomial depending on the problem. Chebyshev polynomial is a popular choice. The Chebyshev polynomial has boundaries at $x = \pm 1$, so that the function value at $|x| > 1$ increases rapidly. On the contrary, inside the interval $[-1, 1]$ it is relatively flat and the absolute value of the function is bounded by 1. The convergence of the Arnoldi (Lanczos) iteration could be boosted by applying the polynomial acceleration with Chebyshev polynomial, by putting unwanted eigenvalues to the bounded region while wanted eigenvalues to the outside of the bounded region.

A.6 QR iteration

There are a number of eigenvalue algorithms such as QR iteration, Jacobi, bisection, and divide-and-conquer. For the case of Lanczos iteration where the target matrix is tridiagonal, Givens' rotation is also

applicable. They are different in the object — general, real symmetric, Hermitian —, the convergence, the number of operations in a step, etc. [72]. The QR iteration is a basic and popular method to find eigenvalues of a square matrix making use of QR decomposition. In this section, QR iteration method is described.

The QR decomposition is already mentioned several times in previous sections. It decomposes a matrix A into the product of a unitary matrix Q and a (right) upper triangular matrix R:

$$A = QR\,. \tag{A.48}$$

This can be done by algorithms such as modified Gram-Schmidt orthogonalization or Householder triangularization. The original Gram-Schmidt method is unstable in numerical computation because it is affected highly by rounding errors, so gives a larger error compared with the modified Gram-Schmidt and Householder algorithm, while the latter two give similar errors.

The QR decomposition of a matrix A can be obtained without further effort from the Gram-Schmidt orthogonalization on the column space of A. Let $A = (a_1|a_2|\cdots|a_m)$ where a_i are columns of A. Orthogonal vectors q_i's constructed by $\{a_1, \cdots, a_i\}$ form the columns of $Q = (q_1|q_2|\cdots|q_m)$, and the coefficients $r_{i,j} \equiv q_i^\dagger a_j$ for the orthogonalization construction fill the elements of R. The details are described

```
A^(0) = A
for i = 1, 2, ···
{
    Q^(i) R^(i) = A^(i−1)      // QR decomposition of A^(i−1)
    A^(i) = R^(i) Q^(i)
}
```

Figure A.4: Basic QR iteration algorithm

in Section A.7. At this moment, let us suppose a matrix A can be decomposed into $A = QR$ by the QR decomposition.

A summary of QR iteration method to find eigenvalues of a square matrix A is present in Fig. A.4. As the iteration continues, $A^{(i)}$ approaches to an upper triangular (or a diagonal if A is Hermitian) form. The details are shown in the following.

After k-th iteration,

$$A^{(k-1)} = Q^{(k)} R^{(k)} \,, \tag{A.49}$$

$$\Rightarrow R^{(k)} = (Q^{(k)})^\dagger A^{(k-1)} \,, \tag{A.50}$$

$$\Rightarrow A^{(k)} = R^{(k)} Q^{(k)} = (Q^{(k)})^\dagger A^{(k-1)} Q^{(k)} \,. \tag{A.51}$$

This implies

$$A^{(k)} = (Q^{(k)})^\dagger (Q^{(k-1)})^\dagger \cdots (Q^{(1)})^\dagger A Q^{(1)} \cdots Q^{(k-1)} Q^{(k)} \tag{A.52}$$

$$\equiv (\tilde{Q}^{(k)})^\dagger A \tilde{Q}^{(k)} \,, \tag{A.53}$$

where $\tilde{Q}^{(k)} \equiv Q^{(1)} \cdots Q^{(k-1)} Q^{(k)}$. Similarly, let us define $\tilde{R}^{(k)} \equiv R^{(k)} R^{(k-1)} \cdots R^{(1)}$. Then,

$$\begin{aligned} A^k &= A^{k-1} A = A^{k-2} A \tilde{Q}^{(1)} \tilde{R}^{(1)} = A^{k-2} \tilde{Q}^{(1)} A^{(1)} R^{(1)} \\ &= A^{k-2} \tilde{Q}^{(1)} Q^{(2)} R^{(2)} R^{(1)} = A^{k-2} \tilde{Q}^{(2)} \tilde{R}^{(2)} = A^{k-3} A \tilde{Q}^{(2)} \tilde{R}^{(2)} \\ &= \cdots = \tilde{Q}^{(k)} \tilde{R}^{(k)} \,. \end{aligned} \tag{A.54}$$

Note that $\tilde{Q}^{(k)}$ is a unitary matrix and $\tilde{R}^{(k)}$ is a right triangular matrix. Therefore, $A^k = \tilde{Q}^{(k)} \tilde{R}^{(k)}$ is indeed the QR decomposition of A^k.

In the meantime, we can consider the columns of $A^k = A^k \mathbb{I}$ as the k-th power iteration on $\{\mathbb{e}_1, \cdots, \mathbb{e}_m\}$, respectively. Hence, as k increases the columns of A^k converge to the eigenvector corresponding to the largest eigenvalue of A. Here, the largest means which has the largest norm. If that eigenvector of the largest eigenvalue is subtracted, remaining converges to the 2nd largest eigenvalue. In the same way, one could obtain all the eigenvectors of A. This is indeed how Gram-Schmidt orthogonalization process works. As a result, the columns of the unitary matrix $\tilde{Q}^{(k)}$ obtained by the QR decomposition of A^k converge to the eigenvectors of A.

Since the columns of $\tilde{Q}^{(k)}$ approximate to the eigenvectors of A, one expect that $A^{(k)} = (\tilde{Q}^{(k)})^\dagger A \tilde{Q}^{(k)}$ approximates to the diagonal matrix having eigenvalues of A on diagonal. More rigorous studies

[73,74] show that it actually converges to the upper triangular matrix for general matrices, and to the diagonal for the Hermitian matrix. Then the diagonal elements of the resulting matrix give eigenvalues of A.

Let us proceed further. Taking inverse and Hermitian conjugate, Eq. (A.54) can be rewritten as

$$(A^\dagger)^{-k} = \tilde{Q}^{(k)}((\tilde{R}^{(k)})^{-1})^\dagger \,. \tag{A.55}$$

Note that $((\tilde{R}^{(k)})^{-1})^\dagger$ is a lower triangular matrix. Let us consider a permutation matrix $P = (\mathbb{e}_m|\mathbb{e}_{m-1}|\cdots|\mathbb{e}_1)$:

$$P = \begin{pmatrix} & & & 1 \\ & & 1 & \\ & \iddots & & \\ 1 & & & \end{pmatrix} . \tag{A.56}$$

Multiplying P and inserting $P^2 = \mathbb{I}$ into Eq. (A.55),

$$(A^\dagger)^{-k}P = [\tilde{Q}^{(k)}P][P((\tilde{R}^{(k)})^{-1})^\dagger P] \,. \tag{A.57}$$

$\tilde{Q}^{(k)}P$ is still unitary, but $[P((\tilde{R}^{(k)})^{-1})^\dagger P]$ now becomes an upper triangular matrix. Hence Eq. (A.57) is the QR decomposition of $(A^\dagger)^{-k}P$. In the analogy to the interpretation of Eq. (A.54), $(A^\dagger)^{-k}P$ is the si-

```
A^(0) = A
for i = 1, 2, ···
{
    [ Set μ^(i) ]
    Q^(i) R^(i) = A^(i−1) − μ^(i) 𝕀      // QR decomposition
                                          // of A^(i−1) − μ^(i) 𝕀
    A^(i) = R^(i) Q^(i) + μ^(i) 𝕀
}
```

Figure A.5: QR iteration algorithm with shifts

multaneous inverse (power) iteration for $A^\dagger$ with the initial vectors $\{\mathbb{e}_m, \mathbb{e}_{m-1}, \cdots, \mathbb{e}_1\}$, and then its QR decomposition gives the eigenvectors of $A^\dagger$, which is the same with those of A. Because $\tilde{Q}^{(k)}P$ is just a reordering of $\tilde{Q}^{(k)}$, the QR iteration algorithm is not only the simultaneous power iteration but also the simultaneous inverse iteration.

From the above observation, one can introduce a shift to accelerate the convergence as in the inverse iteration. Fig. A.5 illustrates the QR iteration algorithm with shifts. Still, $A^{(k)}$ satisfies the same relation with Eq. (A.53):

$$A^{(k)} = (\tilde{Q}^{(k)})^\dagger A \tilde{Q}^{(k)} \,. \tag{A.58}$$

However, instead of Eq. (A.54) and Eq. (A.55), now we have

$$(A-\mu^{(k)}\mathbb{I})(A-\mu^{(k-1)}\mathbb{I})\cdots(A-\mu^{(1)}\mathbb{I}) = \tilde{Q}^{(k)}\tilde{R}^{(k)}\,, \tag{A.59}$$

$$(A^\dagger-(\mu^{(1)})^*\mathbb{I})^{-1}(A^\dagger-(\mu^{(2)})^*\mathbb{I})^{-1}\cdots(A^\dagger-(\mu^{(k)})^*\mathbb{I})^{-1}P = [\tilde{Q}^{(k)}P][P((\tilde{R}^{(k)})^{-1})^\dagger P]\,. \tag{A.60}$$

Thus, as in the inverse iteration, properly chosen $\mu^{(i)}$'s will boost the convergence of the QR iteration algorithm.

An easy choice of $\mu^{(k)}$ is the last entry of the last column of $A^{(k)}$, which is given by

$$A^{(k)}_{m,m} = \mathbb{e}_m^\dagger A^{(k)}\mathbb{e}_m = \mathbb{e}_m^\dagger(\tilde{Q}^{(k)})^\dagger A\tilde{Q}^{(k)}\mathbb{e}_m = (q_m^{(k)})^\dagger A q_m^{(k)}\,, \tag{A.61}$$

where $q_m^{(k)}$ is the m-th column of $\tilde{Q}^{(k)}$. In the QR decomposition of Eq. (A.60), the first column of $\tilde{Q}^{(k)}P$, i.e., the last column of $\tilde{Q}^{(k)}$, corresponds to the eigenvector estimate which is obtained by usual inverse iteration with the initial guess $\mathbb{e}_m$. Hence, $A^{(k)}_{m,m} = (q_m^{(k)})^\dagger A q_m^{(k)}$ is just a Rayleigh quotient, which is a general eigenvalue estimate.

There are also other popular and efficient shifts such as Wilkinson shift [70, 73].

A.7 modified Gram-Schmidt algorithm

Let us consider a set of linearly independent vectors $\{a_1, a_2, \cdots, a_n\}$. The original Gram-Schmidt orthogonalization process constructs a set of basis $\{q_1, q_2, \cdots, q_n\}$ in the following way:

$$q_1 = \frac{a_1}{r_{1,1}}\,, \tag{A.62}$$

$$q_2 = \frac{a_2 - (q_1^\dagger a_2) q_1}{r_{2,2}}\,, \tag{A.63}$$

$$q_3 = \frac{a_3 - (q_1^\dagger a_3) q_1 - (q_2^\dagger a_3) q_2}{r_{3,3}}\,, \tag{A.64}$$

$$\vdots$$

$$q_n = \frac{a_n - \sum_{i=1}^{n-1} (q_i^\dagger a_n) q_i}{r_{n,n}}\,, \tag{A.65}$$

with proper normalization $r_{i,i}$'s. In words, it projects a_i to orthogonal space to $\mathrm{span}\{q_1, q_2, \cdots, q_{i-1}\}$ — let us call the projection operator as $P_{\perp \mathrm{span}\{q_1, q_2, \cdots, q_{i-1}\}}$. This procedure does not have any problem in the mathematical point of view. In the numerical computation, however, the process of (A.62) $\sim$ (A.65) is affected much by rounding errors, so it is unstable and bring somewhat large errors.

On the other hand, the modified Gram-Schmidt orthogonalization is stable and produces relatively smaller errors compared with the original one. While the original method performs the projection in a single step by $P_{\perp \mathrm{span}\{q_1, q_2, \cdots, q_{i-1}\}}$, the concept of the modified version

is that the projection is divided by multiple steps $P_{\perp q_k}$ so that they are performed in order:

$$q_1 = \frac{a_1}{r_{1,1}}\,, \tag{A.66}$$

$$q_2^{(1)} = a_2 - (q_1^\dagger a_2) q_1 \;\Rightarrow\; q_2 = \frac{q_2^{(1)}}{r_{2,2}}\,, \tag{A.67}$$

$$\begin{aligned} q_3^{(1)} &= a_3 - (q_1^\dagger a_3) q_1 \\ &\Rightarrow\; q_3^{(2)} = q_3^{(1)} - (q_2^\dagger q_3^{(1)}) q_2 \;\Rightarrow\; q_3 = \frac{q_3^{(2)}}{r_{3,3}}\,, \end{aligned} \tag{A.68}$$

$$\begin{aligned} q_4^{(1)} &= a_4 - (q_1^\dagger a_4) q_1 \\ &\Rightarrow\; q_4^{(2)} = q_4^{(1)} - (q_2^\dagger q_4^{(1)}) q_2 \;\Rightarrow\; q_4^{(3)} = q_4^{(2)} - (q_3^\dagger q_4^{(2)}) q_3 \\ &\Rightarrow\; q_4 = \frac{q_4^{(3)}}{r_{4,4}}\,, \end{aligned} \tag{A.69}$$

$$\vdots$$

$$\begin{aligned} q_n^{(1)} &= a_n - (q_1^\dagger a_n) q_1 \;\Rightarrow\; q_n^{(2)} = q_n^{(1)} - (q_2^\dagger q_n^{(1)}) q_2 \\ &\Rightarrow\; \cdots \;\Rightarrow\; q_n^{(n-1)} = q_n^{(n-2)} - (q_{n-1}^\dagger q_n^{(n-2)}) q_{n-1} \\ &\Rightarrow\; q_n = \frac{q_n^{(n-1)}}{r_{n,n}}\,. \end{aligned} \tag{A.70}$$

Here, $r_{i,i}$'s are normalization constants given by $r_{i,i} = \|q_i^{(i-1)}\|$. Note that $q_i^{(k)} = P_{\perp q_k} q_i^{(k-1)}$. Because

$$P_{\perp \mathrm{span}\{q_1, q_2, \cdots, q_{i-1}\}} = P_{\perp q_{i-1}} \cdots P_{\perp q_2} P_{\perp q_1}\,, \tag{A.71}$$

both algorithm should give exactly the same result in the mathemat-

```
for i = 1, 2, ··· , n
{
    q_i = a_i
    for j = 1, 2, ··· , i − 1
    {
        r_{j,i} = q_j^† q_i
        q_i = q_i − r_{j,i} q_j
    }
    r_{i,i} = ‖q_i‖
    q_i = q_i / ‖q_i‖
}
```

Figure A.6: Basic modified Gram-Schmidt algorithm

ical point of view.

Fig. A.6 is a basic version of the modified Gram-Schmidt algorithm in accordance with the process (A.66) $\sim$ (A.70), Arnoldi algorithm in Fig. A.2 and Lanczos algorithm in Fig. A.3 are based on this.

In practice, the basic algorithm in Fig. A.6 is not efficient for the parallel processing, because the nested loop for j is composed of sequential processes. Fig. A.7 is a variant of the modified Gram-Schmidt algorithm, where the parallel processing is considered. In this version, each step of the nested loop for j is composed of independent calculations between each other, so that they can be performed in parallel.

```
for i = 1, 2, ··· , n
{
    q_i = a_i
}

for i = 1, 2, ··· , n
{
    r_{i,i} = ‖q_i‖
    q_i = q_i/‖q_i‖
    for j = i + 1, i + 2, ··· , n
    {
        r_{i,j} = q_i^† q_j
        q_j = q_j − r_{i,j} q_i
    }
}
```

Figure A.7: modified Gram-Schmidt algorithm considering the parallel processing

국문초록

스태거드 쿼크의 카이랄성과 테이스트 대칭성

정환철
서울대학교 대학원
물리천문학부 물리학 전공

본 학위논문에서는 향상된 스태거드 쿼크의 고유값이 가지는 일반적인 성질과 고유값 스펙트럼에서 나타나는 카이랄 대칭성과 SU(4) 테이스트 대칭성의 형태를 살펴본다. 스태거드 페르미온은 양자색역학을 연구하는 데 사용되는 격자 게이지 이론의 한 방법론이다. 아쉽게도 격자 위에서 정의된 스태거드 쿼크에서 카이랄 대칭성과 테이스트 대칭성이 정확하게 보존되지 않는다. 하지만, 본 연구의 결과는 HYP 스태거드 쿼크, Asqtad 스태거드 쿼크, HISQ 스태거드 쿼크와 같은 향상된 스태거드 쿼크들에 대해서 이러한 대칭성들이 상당히 잘 보존되며 연속계의 성질을 어느 정도 유지하고 있다는 것을 보인다. 본 학위논문에서 수행된 계산 시뮬레이션들은 Quenched 양자색역학 근사법과 HYP 스태거드 쿼크를 사용하여 수행되었다.

본 학위논문에서는 새로운 카이랄성 오퍼레이터와 시프트(이동) 오퍼레이터를 정의한다. 골터만의 기약 표현 정의와는 달리, 이 새로운 정의는 연속계의 카이랄성 오퍼레이터인 γ_5가 만족하는 것과 같은 회귀

공식을 만족하며, 스태거드 페르미온 액션에서 보존되는 $U(1)_A$ 축대칭성의 Ward identity 에 의해 두 오퍼레이터가 연결된다. 이러한 새로운 카이랄성 오퍼레이터를 사용하여 스태거드 디랙 고유모드에 대해서 카이랄성을 측정하고, 이로부터 제로 모드를 구분하고 그 결과가 인덱스 정리에 따라 위상전하 값과 일치하는 것을 보인다.

이러한 통상적인 카이랄성 측정방법을 확장하여, 카이랄 오퍼레이터와 시프트 오퍼레이터의 스태거드 디랙 고유공간에서의 행렬원소를 측정하여 하나의 고유모드에서 다른 고유모드로 전이되는 카이랄성의 정도를 연구한다. 이 측정값을 리키지(누출)라고 명명한다. 카이랄 Ward identity에 의해 카이랄 오퍼레이터와 시프트 오퍼레이터의 리키지 원소 중 8개가 서로 같다는 것을 보일 수 있고, 이 결과는 계산 오차 내에서 잘 성립된다. 추가적인 연구를 통해 제로 모드와 비제로(제로가 아닌) 모드의 리키지가 서로 반대되는 패턴을 나타내는 것을 살펴본다. 이를 이용하여 제로모드와 비제로모드를 정밀하게 구분할 수 있을 것이다. 또한, 비제로모드의 리키지에서는 SU(4) 테이스트 대칭성의 존재가 명확하게 드러나는데, 이로부터 테이스트 대칭성의 깨짐의 정도를 측정할 수 있는 2가지 지표를 측정한다. 이러한 리키지 패턴이 보편적으로 만족됨을 기계 학습 분석법을 사용하여 보인다. 더불어, 본 연구의 부산물로서 카이랄성의 재규격화를 논의한다.

주요어: 양자색역학, 격자 게이지 이론, 스태거드 페르미온,
카이랄 대칭성, 테이스트 대칭성

학번: 2012-30108